Computational Fluid Dynamics-Modelling of a Multi-Stage Transonic Axial-Flow Compressor

by

Philip Nel

Thesis presented in partial fulfilment of the requirements for the degree of Master of Engineering (Mechanical) in the Faculty of Engineering at Stellenbosch University

Supervisor: Prof. S.J. van der Spuy

Co-supervisor: Prof. T.W. von Backström

December 2019

Stellenbosch University https://scholar.sun.ac.za

Declaration

By submitting this thesis electronically, I declare that the entirety of the work contained therein is my own, original work, that I am the sole author thereof (save to the extent explicitly otherwise stated), that reproduction and publication thereof by Stellenbosch University will not infringe any third party rights and that I have not previously in its entirety or in part submitted it for obtaining any qualification.

Date: December 2019 .....

Copyright © 2019 Stellenbosch University
All rights reserved.

Stellenbosch University https://scholar.sun.ac.za

Abstract

Computational Fluid Dynamics-Modelling of a Multi-Stage Transonic Axial-Flow Compressor

P. Nel

Department of Mechanical and Mechatronic Engineering,
University of Stellenbosch,
Private Bag X1, Matieland 7602, South Africa.

Thesis: MEng (Mech)

December 2019

This research originates from commercial interest in the numerical modelling of transonic axial compressors. The Darmstadt R-1/S-1 and NASA Stage-37 transonic stages are used as validation test cases using commercial (ANSYS® CFX®) and open-source (MULTALL-open) CFD software. Various turbulence models, including a transition model, are tested. The structure parameter of the $SST - \gamma Re_\theta$ model is calibrated to reduce over-predicted shock-induced boundary layer separation and to predict the correct separation behaviour on the Darmstadt stator. At the operating point, the numerical and experimental stage pressure ratio and efficiency for NASA Stage-37 differ by 0.8% and 0.3%, respectively (1.8% and 1.5% for the Darmstadt test case). Aspects of a specific multi-stage compressor, such as the effects of fillets and surface roughness are investigated. It was found that at certain shaft speeds, fillets restrained hub corner stall. Blade surface roughness has a greater effect on overall performance than endwall roughness due to for example, the outward migration of a thickened suction side boundary layer, which mixes with the tip leakage flow. The difference between transient and steady-state results is investigated. Inaccurate treatment of flow features at the mixing plane of a steady-state model gains significance in the modelling of multi-stage compressors. The mixing plane approximation leads to reduced hub corner stall at some blade rows and reduced entropy production by the tip clearance flow. Lastly, the ability of the MULTALL-open turbomachinery design suite of programs to be used for transonic axial compressor performance prediction is investigated. Good estimates could be obtained. The accuracy with which MULTALL resolves typical flow features of transonic axial compressors such as the tip clearance flow features, is found to be promising. It is concluded that MULTALL can be used for transonic axial compressor performance prediction.

Stellenbosch University https://scholar.sun.ac.za

Uittreksel

Berekeningsvloeimeganika-Modellering van 'n Multi-Stadium Transsoniese Aksiaalvloei Kompressor

("Computational Fluid Dynamics-Modelling of a Multi-Stage Transonic Axial-Flow Compressor")

P. Nel

Departement Meganiese en Megatroniese Ingenieurswese,
Universiteit van Stellenbosch,
Privaatsak X1, Matieland 7602, Suid Afrika.

Tesis: MIng (Meg)

Desember 2019

Hierdie navorsing ontstaan uit kommersiële belangstelling in die numeriese modelering van transsoniese aksiaalvloei kompressors. Die Darmstadt R-1/S-1 en NASA Stage-37 transsoniese kompressor stadiums word gebruik as toetsgevalle vir kommersiële (ANSYS® CFX®) en oopbron (MULTALL-open) berekeningsvloeimeganika sagteware. Verskillende turbulensie modelle word getoets, insluitende 'n turbulensie-oorgangsmodel. Die struktuur parameter van die $SST - \gamma Re_\theta$ turbulensie model is gekalibreer om oorgeskatte skok-geïnduseerde grenslaag skeiding te verminder en om die korrekte wegbrekingsgedrag op die Darmstadt stator te voorspel. By die ontwerpspunt verskil die numeriese en eksperimentele drukverhouding en benuttingsgraad van die NASA Stage-37 toetsgeval met 0.8% en 0.3%, onderskeidelik (1.8% en 1.5% vir die Darmstadt toetsgeval). Aspekte van 'n spesifieke multi-stadium kompressor, soos die effekte van vulradiusse en oppervlakgrofheid word ondersoek. Daar is gevind dat by sekere as-snelhede, vulradiusse die naafhoek wegbreking verminder. Die grofheid van die lem se oppervlak het 'n groter effek op die algehele verrigting as die grofheid van die rand a.g.v. bv.; die uitwaartse migrasie van 'n verdikte grenslaag aan die laagdruk kant van die lem, wat met die lekvloei van die lempunt meng. Die verskil in resultate tussen tyd afhanklike en bestendigte modelle word ondersoek. Onakkurate hantering van die vloei kenmerke by die meng-tussenvlak van die bestendige model, word uitgelig in die modellering van multi-stadium kompressors. Die meng-tussenvlak benadering lei tot verminderde naafhoek wegbreking by party lemrye en verminderde entropie produksie by die lekvloei van die lempunt. Laastens word die vermoë van die MULTALL turbo-

Stellenbosch University https://scholar.sun.ac.za

masjienerie ontwerpsprogramme vir die gebruik van transoniese aksiaalvloei kompressor verrigtingsvoorspelling ondersoek. Goeie skattings kon verkry word. Die akkuraatheid waarmee MULTALL tipiese vloei eienskappe van transsoniese aksiaalvloei kompressors soos die lekvloei by die lempunt oplos, is belowend. Daarmee word afgelei dat MULTALL gebruik kan word vir die voorspelling van die verrigting van transsoniese aksiaalvloei kompressors.

Stellenbosch University https://scholar.sun.ac.za

Acknowledgements

The author would like to acknowledge the following contributions:

- For their support, Prof. S.J. van der Spuy and Prof. T.W. von Backström, the supervisor and co-supervisor of this work.
- NUMECA (Germany) for providing the geometry of the Darmstadt R-1/S-1 test case of Technische Universität Darmstadt.
- Dr Hannes Pretorius of DeltaV Aerospace. DeltaV Aerospace sponsors this work.
- The HPC1 computing cluster of Stellenbosch University.
- The CSIR Rosebank CHPC (Centre for High Performance Computing).

Stellenbosch University https://scholar.sun.ac.za

Contents

Stellenbosch University https://scholar.sun.ac.za

Stellenbosch University https://scholar.sun.ac.za

Stellenbosch University https://scholar.sun.ac.za

List of Figures

Stellenbosch University https://scholar.sun.ac.za

Stellenbosch University https://scholar.sun.ac.za

Stellenbosch University https://scholar.sun.ac.za

Stellenbosch University https://scholar.sun.ac.za

List of Tables

Stellenbosch University https://scholar.sun.ac.za

Nomenclature

Acronyms

CFD Computational fluid dynamics
HPC High pressure compressor
LES Large eddy simulation
LPC Low pressure compressor
NACA National Advisory Committee for Aeronautics
NASA National Aeronautics and Space Administration
SST Shear stress transport

Symbols (Latin)

A	Area	$[\,\mathrm{m}^2\,]$
h_s	Sand grain roughness height	$[\,\mathrm{m}\,]$
k	Turbulence kinetic energy	$[\,\mathrm{m}^2/\mathrm{s}^2\,]$
l_t	Turbulent length scale	$[\,\mathrm{m}\,]$
$\dot{m}$	Mass flow rate	$[\,\mathrm{kg/s}\,]$
$\overline{p_s}$	Averaged static pressure	$[\,\mathrm{kg/m.s}^2\,]$
v	Kinematic viscosity	$[\,\mathrm{m}^2/\mathrm{s}\,]$
u	Local velocity	$[\,\mathrm{m/s}\,]$
u_τ	Friction velocity	$[\,\mathrm{m/s}\,]$
r	Radius	$[\,\mathrm{m}\,]$
t	Time	$[\,\mathrm{s}\,]$
U	Mean velocity	$[\,\mathrm{m/s}\,]$
u'	Root-mean-square of turbulent velocity fluctuations	$[\,\mathrm{m/s}\,]$
y	Normal distance from wall	$[\,\mathrm{m}\,]$
y_0	Wall shift distance	$[\,\mathrm{m}\,]$

Symbols (Greek)

ϵ	Rate of dissipation of turbulence kinetic energy	$[\,\mathrm{m}^2/\mathrm{s}^3\,]$
δ^*	Displacement thickness	$[\,\mathrm{m}\,]$

Stellenbosch University https://scholar.sun.ac.za

μ_t	Turbulent viscosity	$[\,\mathrm{kg/m.s}\,]$
ρ	Density	$[\,\mathrm{kg/m^2}\,]$
τ_w	Wall shear stress	$[\,\mathrm{N/m^2}\,]$
ω	Specific rate of dissipation of turbulence kinetic energy	$[\,\mathrm{m^2/s^3}\,]$

Subscripts

A	ANSYS® Solution
Ch	Choke
D	Design
r	Rough surface
s	Smooth surface

Dimensionless numbers

a_1	Structure parameter
Re	Reynolds number
b	Nondimensionalised effective reduction in flow area
$\overline{c_p}$	Averaged pressure coefficient
C	Von Kármán constant # 1
C_{lim}	Shear stress limiting coefficient
h_s^+	Nondimensionalised sand grain roughness height
I	Fractional turbulent intensity
Ma	Mach number
u^+	Dimensionless velocity
y^+	Dimensionless normal distance from wall
y_0^+	Dimensionless wall shift distance
κ	Von Kármán constant # 2
η_{tot}	Total to total isentropic efficiency
π_{tot}	Total to total isentropic efficiency

Stellenbosch University https://scholar.sun.ac.za

Chapter 1

Introduction

The historical background of transonic axial compressors, leading to the thesis objectives, is discussed in this chapter.

1.1 Background and motivation

A brief history of turbomachine development provides historical context for this work. The motivation and possible contribution of this thesis are subsequently discussed.

1.1.1 Historical background

In 1884, Sir Charles Parsons, a British engineer, invented a multi-stage steam turbine for use in marine propulsion. During the same year, he patented a turbine in reversed configuration for use as a compressor (Dixon, 2014) (Funk & Wagnall, 2008).

By 1900, reversed turbines were used as compressors for blast furnace work. Due to a lack of aerodynamic understanding, such as adverse pressure gradient causing flow separation and blade stall, these designs were inefficient. These machines were especially inefficient when attempting to produce a design with higher delivery pressures. As a result, development on axial compressors was abandoned in favour of centrifugal compressors, which offered robustness and higher efficiency (Aungier, 2004).

Following the invention of the aeroplane and its role during the First World War, the need for aerodynamic understanding became apparent. In 1926, A. A. Griffith published his aerofoil theory of compressor and turbine design. Engineers Frank Whittle of the United Kingdom and Hans von Ohain of Germany, both independently developed the turbojet concept in the late 1930s (Flack, 2005). In August of 1939, the world's first jet propelled aircraft, the Heinkel He 178, had its maiden flight. It was powered by the HeS 3 centrifugal turbojet engine, designed by von

Stellenbosch University https://scholar.sun.ac.za

Ohain with the help of Ernst Heinkel. A photo of a replica of the HeS 3 is shown in Figure 1.1.

Although rugged and easier to manufacture than their axial counterparts, centrifugal compressors offer a lower mass flow rate for a given frontal area (by geometric nature). Furthermore, when attempting to reduce the frontal area of a centrifugal turbojet by introducing multi-staging, the decrease in efficiency is bound to be significant due to severe turning of the flow.

The advantages of axial-flow compressors for aircraft propulsion soon became apparent. The Junkers Jumo 004B, shown in Figure 1.2, was the first axial-flow turbojet placed in production. The engine was designed by Anselm Franz and based on von Ohain's patent. It was used to power the Messerschmitt Me 262, which had its first turbojet equipped flight in July of 1942.

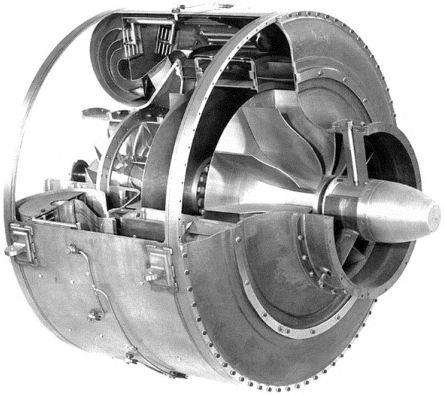

Figure 1.1: HeS 3 Centrifugal turbojet engine at the Deutsches Museum in Munich *(photographer: Hans-Jochum Becker).*

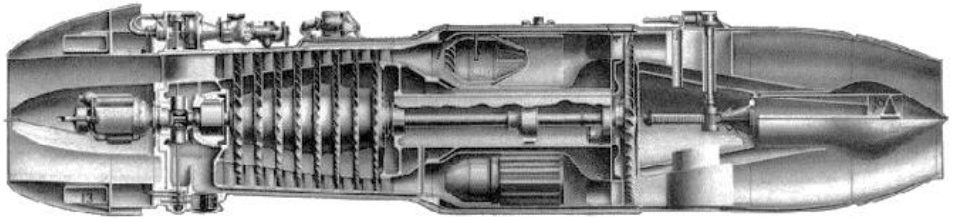

Figure 1.2: Jumo 004B axial turbojet engine illustration *(Junkers Flugzeug- und Motorenwerke, 1944).*

In the years following World War II, it soon became widely understood that axial compressors are able to achieve higher pressure ratios due to efficient multi-staging as well as less variation in efficiency with mass flow rate. With advances

Stellenbosch University https://scholar.sun.ac.za

in materials and manufacturing technology, the advantages of manufacturing centrifugal compressors became of lesser significance. The axial-flow configuration is preferred for manned, winged, jet-powered aircraft, offering higher thrust and efficiency at lower drag. The importance of efficiency is particularly pronounced in the aerospace industry, since a slight increase in efficiency results in substantial cost saving.

A better understanding of supersonic flow gave rise to the transonic compressor, commonly found in modern jet aircraft engines and stationary gas turbines (Farokhi, 2008). The particulars of this development are discussed in Chapter 2. A modern turbofan engine with transonic compressor, the EJ200, as found in the Eurofighter Typhoon, is shown in Figure 1.3. Transonic axial compressors are particularly convenient for aircraft propulsion due to high thrust to weight ratio obtained from maximizing the stage pressure ratio. In transonic compressors, high shaft speeds lead to supersonic relative flow at the blade tip, with the flow at the hub remaining subsonic. Calvert and Ginder (1999) identify three main categories of transonic compressors: the high bypass ratio single-stage fan used in civil aero-engines, the multi-stage low-pressure compressor (LPC) for military aero-engines and the frontal stages of multi-stage industrial gas turbines. A mere two transonic rotor stages are needed to produce the same pressure ratio as that of the Jumo 004B subsonic axial compressor, which produced a cycle pressure ratio of 3.14 across eight stages. However, when designing transonic axial compressors, performance prediction proves to be particularly challenging.

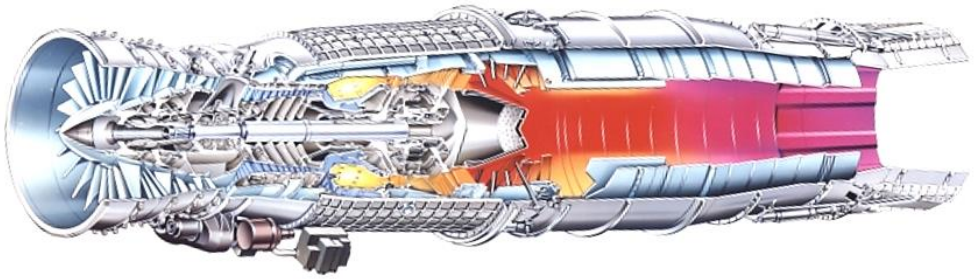

Figure 1.3: EJ200 Turbofan engine with highly loaded transonic compressors *(Courtesy of Rolls-Royce, plc).*

1.1.2 Thesis background and motivation

Due to the complexity of flow within transonic axial compressors, challenges arise when using computational fluid dynamics (CFD) to predict their performance. Flow phenomena within these compressors include significant secondary flows, shock waves and the consequent shock- and boundary layer interactions which may cause shock-induced flow separation, and flow destabilization resulting from additional aerodynamic complications (Biollo & Benini, 2011). Aforementioned concepts are discussed in Chapter 2.

Stellenbosch University https://scholar.sun.ac.za

These complexities may result in present-day limitations on the prediction of compressor performance using CFD. It is therefore proposed that an investigation be performed in order to obtain a clearer understanding of the physics, CFD related challenges, and limitations experienced when modeling a transonic compressor. There is currently an interest in developing a South African capability in the modeling of small transonic axial-flow compressors. The investigation is to be performed using CFD codes which are of interest to the local industry.

1.2 Thesis objectives

In 2017, Professor John Denton, formerly of the Whittle Lab (University of Cambridge), released his turbomachinery design system, MULTALL, as open-source software. The opportunity therefore exists to use MULTALL-open in commercial compressor design. Commercial advantages may include rapid design and adaption of compressor geometry, as well as cost saving.

In order to investigate its suitability and possible advantages, MULTALL-open, as well as a widely acknowledged commercial CFD code, ANSYS®, are to be used. A baseline transonic axial compressor stage for which experimental results exist is to be modeled in order to calibrate the CFD setup. This baseline stage is to be modeled in both ANSYS® and MULTALL. Results from these CFD codes are to be compared and analysed in order to gain an understanding of the physics involved in the flow through the compressor as well as the CFD-related limitations experienced when investigating the flow. Furthermore, specific aspects of the performance of a proprietary multi-stage transonic axial compressor which is of interest to the local industry, are investigated. The main investigation of this specific compressor is to be carried out using ANSYS® CFX®. Aspects that will be evaluated are:

1. Quantify the effect of fillets on compressor aerodynamic performance.
2. Quantify the effect of blade and wall roughness on compressor performance.
3. Quantify the difference between transient vs steady-state compressor performance results (at design and off-design).
4. Perform grid dependency studies.

The ANSYS® simulation will consider various turbulence models as well as a transition model. Conclusions are to be made regarding the suitability of using MULTALL for transonic axial compressor performance prediction.

Stellenbosch University https://scholar.sun.ac.za

Chapter 2

Literature Study

In the first section of this chapter, the incentive for the use of transonic compressors is studied by reviewing important historical developments. Following this, complications with transonic axial compressor performance prediction are discussed. Lastly, the CFD validation test cases are introduced.

2.1 Supersonic and transonic compressor background

In the 1940s, researchers settled on the idea of supersonic compressors as the next step in compressor design. It was known that, due to shock waves, higher energy losses are inevitable with supersonic compressors. The aim was to achieve pressure rise through compression shocks in the most efficient manner. This could be done, for example, by canceling extended wave patterns resulting from such a shock (Kantrowitz, 1950). There is also potential for savings in weight and size.

Weise, a German aeronautics researcher, was the first to develop a supersonic compressor (Hawthorne, 2017). In Weise's first supersonic compressor, the rotor tangential velocity was such that the energy imparted on the subsonic inlet flow increased the relative Mach number to about 1.5. The rotor featured extremely high (90 degree) turning (Hawthorne, 2017). In the stator, kinetic energy was converted to pressure energy by means of a normal shock. It is believed that the normal shock induced flow separation, leading to disappointing compressor efficiency (26%). The achieved pressure ratio was recorded to be less than 1.4.

In the late 1940s, Kantrowitz of the NACA Langley Research Center continued investigations on supersonic compressors. In contrast to Weise's design, the design of Kantrowitz featured a rotor with low turning and a shock at the rotor passage inlet. The stator was subsonic and featured tandem vanes which allowed for high turning (Broichhausen & Ziegler, 2005). This means that the rotor pressure rise in the Kantrowitz supersonic compressor is attributed mainly to the shock. Further pressure rise is achieved by high turning in the stator. This design is referred to

Stellenbosch University https://scholar.sun.ac.za

as an impulse-type rotor and allowed for a pressure ratio of 2, with a promising efficiency in the order of 65%.

In 1952, Klapproth of the NACA Lewis Flight Propulsion Laboratory presented a rotor with supersonic flow throughout the rotor passage, avoiding strong shocks in the rotor (Klapproth, 1952). His shock-in-stator-type compressor allowed for a pressure ratio of 2.6 at an efficiency of 67%. Axial-flow compressor research was terminated at NACA in 1957 (Calvert & Ginder, 1999). The pioneering work of Weise, Kantrowitz and Klapproth proved the potential of supersonic flow in compressors.

During the 1960s, supersonic compressor research was continued in the United States of America as well as in Europe. A significant development following research in supersonic cascade rows was to demonstrate that a turning blade row followed by an overlapping diamond shaped blade row to avoid suction side separation of the first blade row is a favourable arrangement for both sub- and supersonic conditions (Broichhausen & Ziegler, 2005). Contributions through various research groups such as NASA, the Von Kármán Institute, and RWTH Aachen University had led to design improvements enabling total isentropic efficiencies of 90% and 87% for impulse-type and shock-in-stator-type (supersonic flow throughout the rotor) rotors, respectively. Pressure ratios exceeded 3. However, when operating these rotors in a stage arrangement, it was found that unsteady interference occurs between the rotor and stator. This was also the case for the shock-in-stator-type rotor for which no interference is contemplated due to relative and absolute supersonic rotor outlet flow. Despite this, the interference was found to be caused by reduced flow velocities due to throttling by the stator, causing localized subsonic axial flow in the rotor wake which enables upstream interference by the stator. This issue was to be resolved using a variable stator. However, shock-induced stator vibrations followed. Further investigations led to a diagonal rotor which proved to be stable throughout the operating speed range. Such compressors were planned to be used for UAV applications, and had a pressure ratio of 4.8 at a total isentropic efficiency of 74% (Broichhausen & Ziegler, 2005).

Existing knowledge of subsonic compressors and transonic aerofoil flow, combined with the findings from supersonic compressor research had led to the development of the transonic compressor. In this paragraph, the main transonic compressor categories identified by Calvert and Ginder (1999) are briefly discussed. The single-stage transonic fan at the inlet of civil aero-engine fans is of crucial importance to these engines. It is responsible for about 75% of the total thrust. Typical design pressure ratios and tip speeds range from 1.6 to 1.8 and 400 to 460 m/s, respectively, with inlet relative Mach numbers of up to 1.5. The overall pressure ratio of a multi-stage military LPC ranges from 2.5 to 5. This is typically achieved within two to three stages, with inlet relative Mach numbers often as high as 1.7 for the first stage. The frontal stages of modern industrial gas turbines often feature transonic flow. High specific flow is less important, with emphasis on a wide operating range. Inlet relative Mach numbers for these compressors are generally below 1.2 (Calvert & Ginder, 1999).

Stellenbosch University https://scholar.sun.ac.za

According to Broichhausen and Ziegler (2005), the high stage pressure ratios in the order of 1.7-1.8 common to modern high performance transonic compressors are achieved through a combination of high rotor tip speeds, in the order of 500 m/s, as well as a high stage loading, in the order of 1.

2.2 Shock waves and shock-induced separation

A bow shock near the rotor passage entrance (rotor-bow shock) is caused by leading edge thickness as well as by the expansion waves emanating from the (fore) surface of the suction side of the neighbouring blade. In transonic axial compressors, the rotor-bow shock leads to shock-induced separation and reattachment on the blade suction side (Weber *et al.*, 2002). Separation is also found in the corner region, where the shock interacts with the endwall boundary layer as well as with that forming on the blade suction side, resulting in a highly three-dimensional vortex structure (Hah & Loellbach, 1999).

According to Prasad (2003), depending on the operating point and in the absence of supersonic axial velocities, the rotor-bow shock on later stages may propagate upstream past the stator wake, interacting directly with the upstream stator. This may lead to unfavourable stator aerodynamic performance, consequently adding to losses.

In context of CFD, the shock could propagate through the inlet of the rotor computational domain. The way in which a CFD solver handles nonlinear waves propagating through a domain boundary may pose challenges (Prasad, 2003). Furthermore, the shock is typically present for the outer 75% of blade span for transonic axial compressors, with flow near the hub either remaining at subsonic conditions or decelerating from supersonic to subsonic flow in absence of a shock (Prasad, 2003). This means that, in the radial direction, the upstream propagating shock structure varies significantly, resulting in highly 3-dimensional flow.

The rotor-bow shock may also interact with vortices and irregular flow patterns coming from the upstream stator wake. This wake-shock interaction may lead to pronounced unsteady effects and may, for example, affect the rotor incidence angle (Estevadeordal *et al.*, 2007). This may lead to unfavourable aerodynamic performance as well as rotor vibrations. Irregular flow patterns may, for example, originate from upstream shock-boundary layer interactions. It is apparent that the physical problem is of a highly time dependent nature.

2.3 Real geometry effects in CFD

In the design process of a transonic axial compressor, a simplified geometry is often considered in order to reduce the complexity of the design process. A higher fidelity model includes real geometry effects, such as tip clearance gaps, fillets, surface roughness, and deformation due to thermal and centrifugal loads. The addition

Stellenbosch University https://scholar.sun.ac.za

of fillets adds a material blockage. Tip clearance gaps render the axial velocity of the leakage flow to be negligible, adding to blockage. A vortex is generated upon leakage of the high pressure flow at the pressure side of the blade to the suction side, resulting in losses. According to a literature study by Chima (1998), it may be suggested that tip clearance effects are not well understood and that the majority of losses often attributed to tip-clearance effects may be due to other causes. According to Hofmann and Ballmann (2002), the tip clearance vortex originates at the leading tip of the blade and is fed from a flow sheet along the tip edge. It then propagates into the blade passage. This vortex interacts with the rotor-bow shock and endwall boundary layer. Upon shock-vortex-interaction, the abrupt flow deceleration affects the vorticity distribution of the vortex. This may lead to diverging flow and consequently vortex breakdown, possibly inducing compressor surge (Hofmann & Ballmann, 2002).

According to Suder (1998), blockage due to boundary layer effects may be defined as:

$$b = 1 - \frac{A - \int \delta^* dr}{A} \tag{2.1}$$

This value represents the non-dimensionalised effective reduction in flow area due to boundary layer displacement thickness. According to the findings of Khalid (1994), and Suder (1998), the aerodynamic loading increases with blockage development until a limiting aerodynamic loading (asymptote intercepting the axis of aerodynamic loading) is approached. Blockage development is influenced by shock-boundary layer interactions as well as tip clearance flow-shock-interactions (Suder, 1998). This may lead to complications in CFD performance prediction due to, for example, the inadequacy of turbulence models to aid in resolving these effects.

Surface roughness leads to boundary layer thickening, resulting in blockage and intensified secondary flows. Bammert and Woelk (1980) found that losses due to surface roughness in a 4 stage turbine were more sensitive to the suction side, more specifically the downstream half thereof. Chen *et al.* (2014) investigated the effect of roughness on NASA Stage-35 and found that the effect of roughness was more sensitive on the suction side, but less significant toward the rear. Millsaps *et al.* (2004) found that the suction side of a compressor cascade was more sensitive to roughness than the pressure side, and that blade loading became sensitive to roughness at $Re > 550000$.

With regards to the effect of fillets, Jongsik-Oh (2016) reports a drop in pressure ratio, choking mass flow rate, and efficiency in a fillet investigation on a centrifugal compressor. Shi *et al.* (2010) states that fillets restrain some corner separation on a single stage turbine, but losses increase due to enhanced secondary flow. Rajeevalochanam *et al.* (2017) reports just under 3% and 2% reduction in mass flow rate and efficiency (respectively) for a 2.4 mm fillet on an axial flow turbine stage. In a 15-stage axial compressor, Kügeler *et al.* (2008) reported that reduced endwall flow turning leads to reduced loading of downstream blade rows. In most cases, research on the effect of fillets on centrifugal or single-stage axial compressors or turbines

Stellenbosch University https://scholar.sun.ac.za

report lower performance and choking mass flow rate due to the fundemental material blockage and decreased flow deflection at the fillet. However, it is interesting to note that Kügeler *et al.* (2008) states that better overall performance was observed in their 15-stage axial compressor fillet investigation, even though Kügeler *et al.* (2008) also reports reduced loading. This may be a result of unexpected effects due to the complexity of a multi-stage axial compressor flow. Brockett and Kozak (1982) showed that small fillets (5% chord) increases the efficiency by 1.4%, suggesting that the corner flow separation was reduced due to the fillet. They suggested that due to the additional drag, fillets larger than 10% chord fail to improve efficiency. On the contrary, Stratford (1973) found that fillets increased separation and losses on a compressor cascade, while Tweedt and Okiishi (1983) found that the effect of fillets was not significant. It would seem that the effect of fillets is highly incomparable between axial flow turbomachines.

2.4 Roughness modelling

In order to gain an understanding of the factors which are involved in roughness modeling, the basic principles upon which roughness modeling is based are briefly investigated.

When the roughness thickness is less than the thickness of the laminar sub layer, the surface is considered to be hydraulically smooth (Schlichting, 1987). Schlichting (1987) defined sand grain roughness to be the roughness equivalent caused by a layer of spheres on a smooth surface, with the sand grain height being the diameter of such a sphere. In 1933, German engineer and physicist Nikuradse (1933) showed that for rough surfaces, the logarithmic law is preserved but shifted. He showed that the sand grain roughness height h_s can be related to u^+ by

$$u^+ = \frac{1}{\kappa} \ln \frac{y^+}{h_s^+} + B \tag{2.2}$$

where

$$u^+ = \frac{u}{u_\tau} \qquad u_\tau = \sqrt{\frac{\tau_w}{\rho}} \qquad y^+ = \frac{y u_\tau}{v} \qquad C = 5.5 \qquad \kappa = 0.40 \tag{2.3}$$

and where B is related to h_s^+ according to

$$\begin{array}{ll} 1 < h_s^+ < 3.5 & B = 5.5 + \frac{1}{\kappa} \ln h_s^+ \\ 3.5 < h_s^+ < 7 & B = 6.59 + 1.52 \ln h_s^+ \\ 7 < h_s^+ < 14 & B = 9.58 \\ 14 < h_s^+ < 68 & B = 11.5 - 0.7 \ln h_s^+ \\ 68 < h_s^+ & B = 8.48 \end{array} \tag{2.4}$$

To simulate this shift in CFD turbulence modeling, Aupoix and Spalart (2003) proposed a wall shift y_0 together with increased turbulent viscosity μ_t near the wall.

Stellenbosch University https://scholar.sun.ac.za

Velocity gradients between rough (r) and smooth (s) surfaces can then be written as:

$$\left.\frac{\partial u_r^+}{\partial y^+}\right|_{y^+} = \left.\frac{\partial u_s^+}{\partial y^+}\right|_{y^+ + y_0^+} \tag{2.5}$$

After integrating and rewriting equation 2.5, the dimensionless velocity shift can be written as:

$$\triangle u^+ = u_s^+(y_0^+) \tag{2.6}$$

Noting that the momentum equation in the boundary layer reduces to

$$(1 + \mu_t^+)\frac{\partial u^+}{\partial y^+} = 1, \tag{2.7}$$

then μ_t and y_0 can be related by combining equation 2.5 and 2.7.

2.5 Transition modelling

In this work, the Wilcox $k-\omega$ turbulence model will simply be referred to as the $k-\omega$ model. Menter's $k-\omega$ SST turbulence model without transition model will simply be referred to as the SST model. When the γRe_θ transition model is used alongside the SST model, it will be referred to as the $SST-\gamma Re_\theta$ model. The $SST-\gamma Re_\theta$ model with standard shear stress limiter will be referred to as the $SST-\gamma Re_\theta, a_1 = 0.31$ model. If the shear stress limiter is adjusted, the model will be referred to as, for example, the $SST-\gamma Re_\theta, a_1 = 0.345$ model.

2.5.1 Significance

Keeping in mind that the Reynolds number in transonic compressors is deemed to be very high, it could be argued for that the effect of transition modelling may be negligible. Some publications, such as the master's thesis of Chinnaswamy (2015) on a compressor stage of Chalmers University, suggest a negligible influence of transition modeling on stage performance. However, a 2011 ANSYS® presentation on transition modeling argues that the $SST-\gamma Re_\theta$ model predicts the total pressure ratio of NASA Rotor-37 much better than the SST and $k-\epsilon$ models. The presentation also shows that incorrect flow topology on the RGW compressor cascade of RWTH Aachen is obtained with the assumption of fully turbulent flow, with the $SST-\gamma Re_\theta$ model performing much better than the SST turbulence model without γRe_θ transition model. The RGW compressor cascade images from the presentation are reproduced in Figure 2.1. In *(b)*, an experimental oil streak visualisation shows a transitional zone characterized by laminar separation and turbulent reattachment. This separation bubble affects the corner stall. In *(a)*, the corner stall is clearly over-predicted when using the SST turbulence model without transition model. In *(c)*, the extent of predicted corner stall is in much closer agreement to the experimental result when using a transition model.

Stellenbosch University https://scholar.sun.ac.za

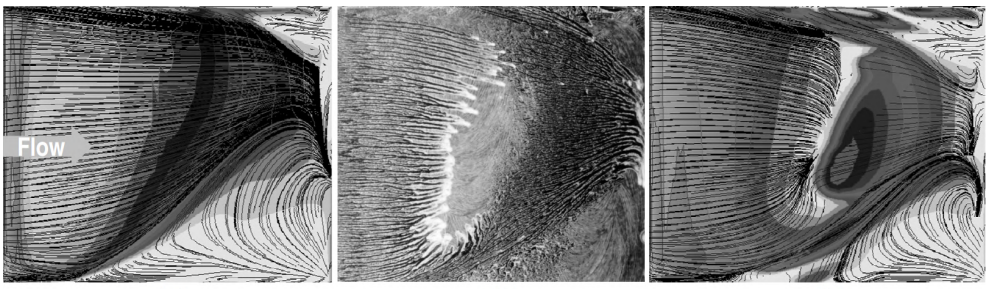

Figure 2.1: RGW compressor cascade: (a) SST, (b) experimental, (c) $SST - \gamma Re_\theta$ (ANSYS®, 2011)

An experimental study by Haideng *et al.* (2015) on the NACA-65 K48 high subsonic compressor cascade shows a transition zone present on the cascade (Figure 2.2). It is narrow and abrupt, caused by laminar separation due to increasing normal strain on the blade suction side in the flow direction.

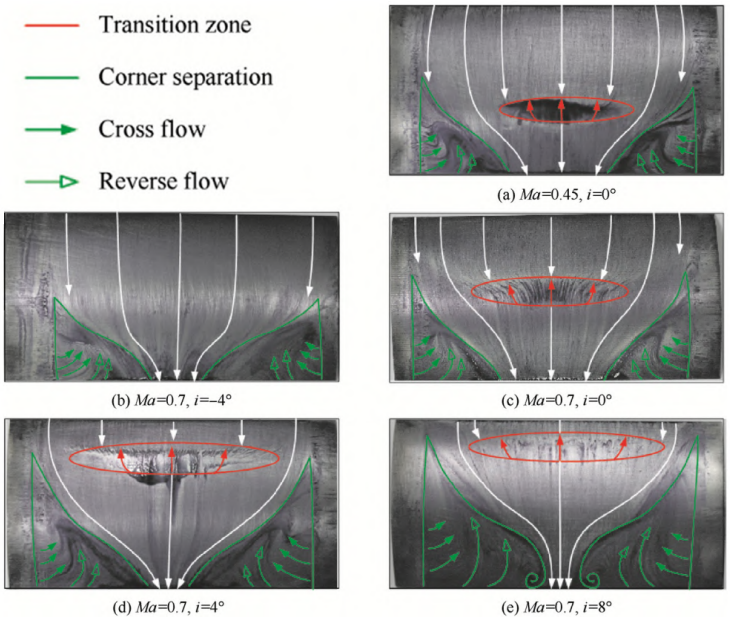

Figure 2.2: Experimental oil streak lines by Haideng *et al.* (2015) on the NACA-65 K48 high subsonic compressor cascade at varying angles of attack.

After transitioning to turbulent flow, the flow re-attaches. Obviously, such a transition zone cannot be predicted when assuming that the flow is turbulent from the leading edge. Furthermore, it is less likely that the flow will separate if the boundary layer is turbulent. This high subsonic compressor cascade is comparable to the stator of a transonic compressor stage. This study also shows that the transition zone shifts in the stream-wise direction, depending on the angle of attack. Depending on the operating point of a transonic compressor, the same will happen

Stellenbosch University https://scholar.sun.ac.za

to the transition zone of the stator as the critical Reynolds number changes. This is important because the transitional zone may affect the extent of corner stall.

A high resolution example of an abrupt transition zone, which can be seen in an oil streak visualization experiment of the suction side of a single cascade blade by Willert and Klinner (2014) is shown in Figure 2.3. The transition zone on this cascade is analogous to what is found on the stator of the Darmstadt compressor (Figure 2.4). Therefore, it is clear that the presence of possibly significant regions of laminar flow and transitional effects which might affect important features such as corner stall are not uncommon in transonic compressors.

Furthermore, it is known that transition modeling is beneficial in aerofoil CFD such as the McDonnell Douglas 30P-30N 3-Element flap test case, where pressure-side boundary layer transition occurs as late as 0.526 of chord fraction on the main flap (Malan *et al.*, 2009). It is apparent that transition modeling may be significant in transonic axial compressor CFD modelling.

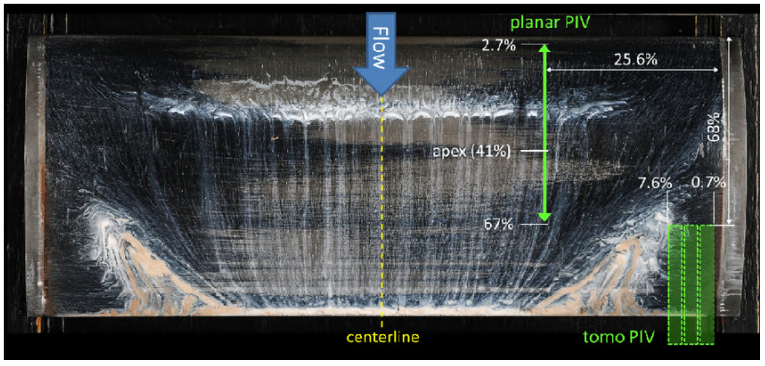

Figure 2.3: "Oil streak visualization of the suction side a single cascade blade overlaid with positions of PIV measurement areas". Reproduced from Willert Klinner (2014).

2.5.2 Application

The $\gamma - Re_\theta$ transition model was presented by Menter *et al.* (2004). Transition onset is completely automatic and is based on the strain-rate Reynolds number rather than the momentum thickness, avoiding the use of non-local variables. In this correlation-based transition model, two additional transport equations are solved. It is therefore the most elaborate transition model in ANSYS® CFX®. Proper application of other available transition models requires more knowledge of what is expected from the boundary layer flow.

According to Menter *et al.* (2006), if the γRe_θ model is to be used, the mesh must have a y^+ value of ~ 1 in order to capture the location of laminar and transitional boundary layers correctly. It is not always practical to have mesh y^+ values of ~ 1, especially from a commercial point of view. Although the transition model

Stellenbosch University https://scholar.sun.ac.za

can still be used at higher y^+ values, it should be noted that the transition onset location moves upstream with increasing y^+ (Menter *et al.*, 2006).

2.6 CFD Validation

In this section, the test CFD validation test cases are introduced. Technical data are given in the following chapter. For CFD validation of a transonic compressor stage, the Darmstadt R-1/S-1 and NASA Stage-37 test cases are selected.

The Darmstadt test case has been operated by the Institute of Gas Turbines and Aerospace Propulsion at the Technische Universität Darmstadt since 1994 (Bergner, 2006). The Darmstadt test case represents a typical high pressure compressor (HPC) of a civil turbofan engine. The baseline Darmstadt test case features excessive stator flow separation. An oil streak visualisation of the stator flow separation can be seen in Figure 2.4. According to Bakhtiari *et al.* (2015), who had utilised an optimization process to eliminate flow separation on the Darmstadt stator, the onset of separation and reattachment on the stator is difficult to predict with RANS isotropic turbulence models. Reising and Schiffer (2009) had predicted large hub corner stall for the entire operating range. In some research papers, the measured experimental pressure ratio of the Darmstadt reaches a maximum just under 1.52 (Müller *et al.*, 2007) (Reising & Schiffer, 2009). Other researchers report a maximum pressure ratio from 1.53 to 1.54 (Baktiari *et al.*, 2015) (Bergner, 2006). From the PhD dissertation of Bergner (2006), the limit of stability of the Darmstadt compressor is around 15 kg/s at 20000 rpm. Excessive stator flow separation occurs in the Darmstadt stator for the entire operating range (Bergner *et al.*, 2003) (Bergner, 2006) (Reising & Schiffer, 2009).

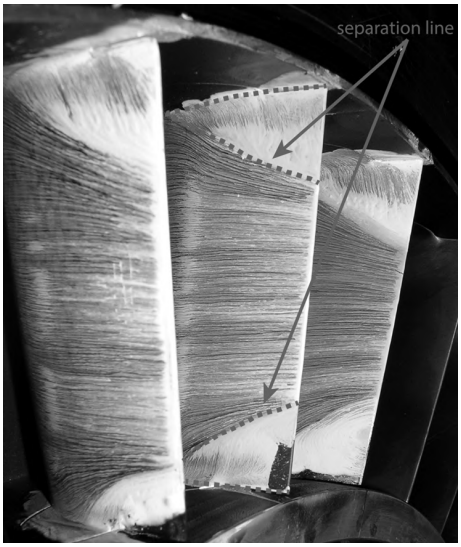

Figure 2.4: Darmstadt stator flow separation. (Bakhtiari *et al.*, 2015)

Stellenbosch University https://scholar.sun.ac.za

For further validation of a transonic stage, NASA Stage-37 is selected. The NASA Stage-37 transonic compressor stage was designed and tested originally by Reid and Moore (1978) of the Lewis Research Center. The compressor stage represents a low aspect ratio inlet stage of an eight-stage aero-engine HPC. In 1994, the rotor was tested in isolation by Suder and Celestina (1995) as well as Suder *et al.* (1995). These results were used for the well-known blind test case sponsored by ASME and IGTI. The unpublished blind test case results showed that the performance of the rotor was challenging to predict. According to Hah (2009), predicted pressure ratios varied by nearly 10% and predicted efficiencies varied by 6 points. It was found that algebraic turbulence models performed worse than turbulent transport models. Hah *et al.* (1996) suggested that the large variation in results is due to corner stall on the rotor suction surface. According to Chima *et al.* (2003), the central-differencing scheme smears out the details of total pressure, and that this effect is exaggerated when analysing a single compressor blade row such as NASA Rotor-37 due to a low total pressure ratio. Shabbir *et al.* (1997) provided evidence that the discrepancies may be due to an error in the experiment related to hub leakage flow. In a study of Rotor-37 using LES, Hah (2009) found a better agreement with experimental results and suggested that this is due to the ability of LES to correctly resolve time dependencies related to flow interactions from features such as the passage shock and tip vortex.

2.7 Concluding remarks

The literature study concludes that the effect of blade fillets may be highly incomparable between axial flow turbomachines, and that adding surface roughness to a compressor mainly results in enhanced boundary layer blockage. Furthermore, it is concluded that the presence of possibly significant regions of laminar flow is not uncommon in a transonic compressor stage and that transition modelling may therefore be important for transonic axial compressor performance prediction. Lastly, it is concluded that the performance of the transonic compressor stages selected for CFD validation may be difficult to predict with RANS turbulence models, and that shock interactions complicates transonic compressor CFD.

Stellenbosch University https://scholar.sun.ac.za

Chapter 3

Validation Test Cases in ANSYS®

3.1 Numerical modelling setup

A typical computational domain is shown in Figure 3.1. Simulations are performed using ANSYS® CFX® 19.1. For steady-state simulations, a single passage is simulated with a mixing plane rotor-stator interface. Unless stated otherwise, surfaces are assumed to be smooth. Tip clearance gaps are considered for all simulations. Unless stated otherwise, simulations consider a single compressor passage and are solved in pseudo-transient with mixing plane rotor-stator interfaces.

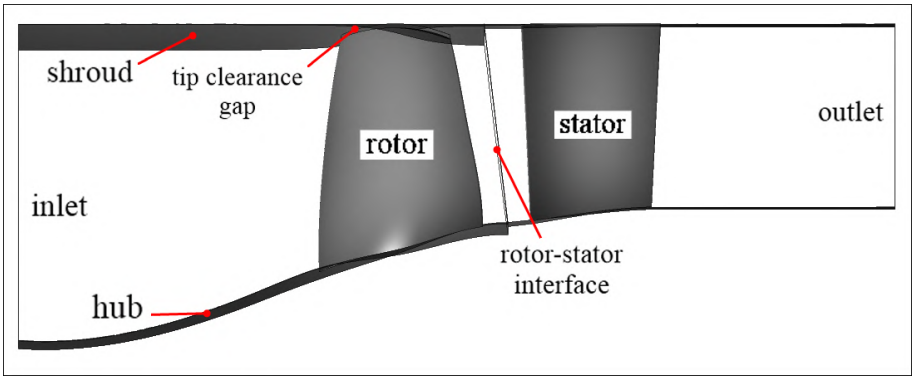

Figure 3.1: Typical computational domain of a compressor stage.

The boundary conditions for NASA Stage-37 are given in Table 3.1. These boundary condition values are consistent with measurements by Reid and Moore (1980). The static outlet pressure is varied in order to obtain a performance curve. In order to obtain an estimate of the experimental inlet boundary profile, the model features a stationary inlet domain with rotating hub and a total length of 0.175 m, similar to the experimental setup. This inlet domain features a relatively coarse, biased mesh. The mesh for NASA Stage-37 can be seen in Appendix A.1.

Modelling control parameters for NASA Stage-37 are shown in Table 3.2. Corresponding information for the Darmstadt test case can be found in Appendix A.2.

Stellenbosch University https://scholar.sun.ac.za

The bounded second-order upwind biased ("high resolution" option) scheme is selected for the advection and turbulence numerics. This is recommended when using the $SST - \gamma Re_\theta$ model (ANSYS®, 2019). When using a transition model with the SST turbulence model, the Kato-Launder turbulent production modification is recommended and automatically enabled (ANSYS®, 2019).

Table 3.1: NASA Stage-37 boundary conditions in ANSYS® CFX®

Location	**Boundary condition**	**Value**
Inlet	Total pressure (subsonic regime)	101.325 kPa
	Total temperature	288.15 K
	Fractional turbulent intensity	0.03
	Flow direction	Normal to boundary condition
Outlet	Static pressure (subsonic regime) with circumferential pressure-averaging and profile blend factor of 0.05 (recommended in ANSYS® manual (2019))	Varied from 1 atm to 1.7 atm depending on turbulence model
Rotating-mesh rotor domain shroud	Wall velocity	Counter rotating at 17188.7 rpm
Inlet domain hub	Wall velocity	Rotating at 17188.7 rpm
Stator domain hub	Wall velocity	Rotating at 17188.7 rpm

Table 3.2: Modelling control parameters in ANSYS® CFX® for NASA Stage-37

Modelling control parameter	**Value**
Floating point accuracy	16 digits
Advection scheme	Bounded second-order upwind biased
Turbulence numerics	Bounded second-order upwind biased
Timescale factor	0.5 (0.1 for starting solution)
Specific heat at constant pressure	1004 J/kg.K (Reid & Moore, 1980)
Ideal gas transport properties	Sutherland's formula

Stellenbosch University https://scholar.sun.ac.za

As seen in Table 3.1, the fractional turbulence intensity is specified. The turbulent intensity at the inlet of NASA Stage-37 and Darmstadt R-1/S-1 is 3% and 4%, respectively (Boretti, 2010) (Haug & Niehaus, 2018). For the multi-stage compressor, the turbulent intensity is assumed to be the recommended and default value of 5% in ANSYS® CFX® (ANSYS®, 2019).

By using the fractional turbulence intensity, the turbulence length scale is automatically computed as follows: The distribution of turbulence kinetic energy and rate of dissipation of turbulence kinetic energy at the inlet is scaled according to the turbulence intensity, I:

$$I = \frac{u'}{U} \tag{3.1}$$

where u' is the root-mean-square of turbulent velocity fluctuations and U is the mean velocity. Since diffusion can be assumed to be negligible, the scaled values of k and ϵ are simply multiplied by the mass flow rate in order to obtain the inlet flow values for k and ϵ (ANSYS®, 2019). The turbulent length scale l_t, which is calculated as the cube root of the domain volume, is related to k and ϵ as follows:

$$\epsilon_{inlet} = \frac{k^{\frac{3}{2}}}{l_t} \tag{3.2}$$

3.2 Technical data

The design parameters of Darmstadt R-1/S-1 and NASA Stage-37 can be seen in Table 3.3. When comparing the NASA and Darmstadt test cases, the Darmstadt test case features a lower inlet relative Mach number, lower rotor blade loading, as well as a higher blade pitch and rotor aspect ratio. The rotor bow-shock interacting with the neighbouring rotor suction side boundary layer stronger in the NASA test case than the Darmstadt test case. For the Darmstadt test case, the hub of the stator domain is stationary. For the NASA test case, the rotor and stator hub rotate, with the stator featuring a hub clearance gap.

Stellenbosch University https://scholar.sun.ac.za

Table 3.3: Design parameters for Darmstadt R-1/S-1 and NASA Stage-37

	Darmstadt R-1/S-1	NASA Stage-37
Mass flow rate (corrected)	16 kg/s	20.19 kg/s
Total pressure ratio	1.5	2.050
Tip speed (corrected)	398 m/s	454.2 m/s
Relative rotor tip inlet Mach number	1.35	1.48
Relative rotor hub inlet Mach number	0.70	1.13
Shaft speed	20000 rpm	17188.7 rpm
Hub to tip radius ratio	0.47	0.70
Tip diameter	0.38 m	0.5 m
Rotor tip clearance gap	1.6 mm	0.356 mm
Stator hub clearance gap	none	0.72 mm
Number of blades	16	36
Number of stator blades	29	46
Rotor blade aspect ratio	1.5	1.26

3.3 Mesh information

The "Single Round Round Symmetric" O-type grid in ANSYS® CFX® is a symmetric topology for single-bladed geometry with round leading and trailing edges for which refinement around the leading and trailing edges is not required. This topology is used for all simulations and is shown in Figure 3.2. An example of a typical mesh obtained with this topology is given in Figure 3.3. In the case of blade fillets, a shallow corner is added to the blade at the hub, as seen in Figure 3.4.

For both test cases, the grid spacing is relatively fine up and downstream of the compressor stage in order to resolve the rotor-bow shock and the wake of stator stall separation in high resolution.

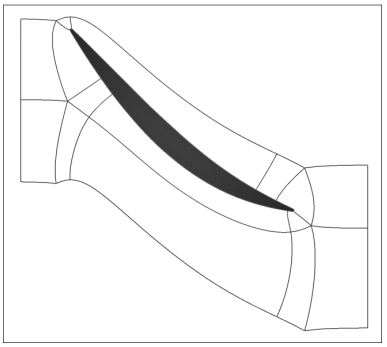

Figure 3.2: Selected mesh topology for ANSYS® CFX® simulations.

Stellenbosch University https://scholar.sun.ac.za

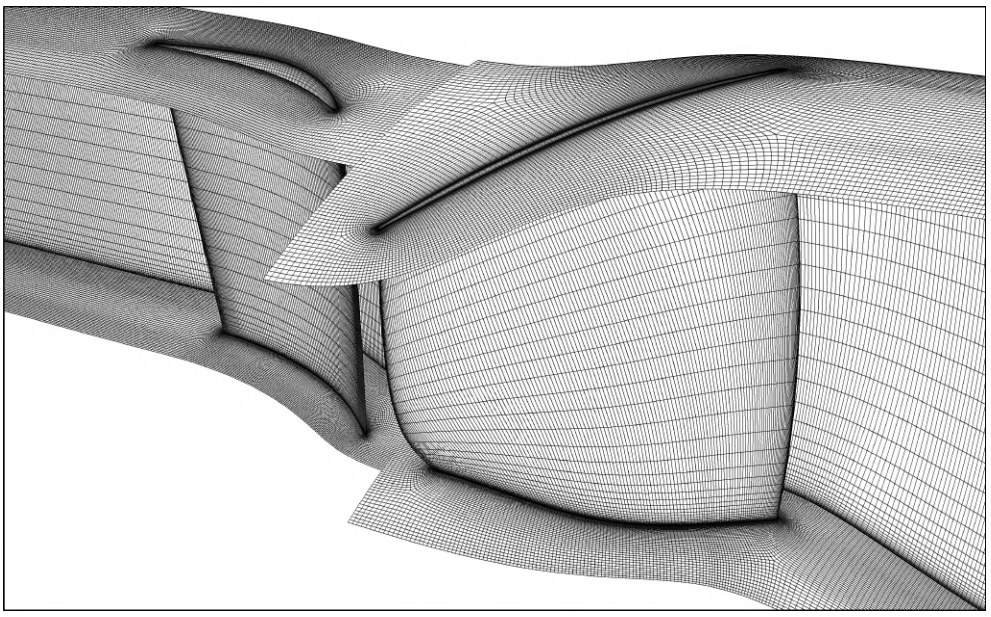

Figure 3.3: An ANSYS® CFX® mesh obtained with the selected mesh topology (Darmstadt R-1/S-1).

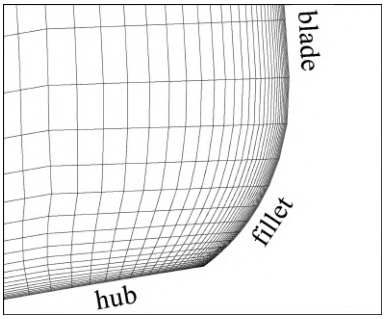

Figure 3.4: Orthogonal detail for geometry with fillets.

The grid convergence information for the Darmstadt test case can be seen in Tables 3.4 to 3.6. The same information for NASA Stage-37 can be found in Appendix A.1. In Table 3.4, the number nodes, first cell height, and solution file size for the different grids can be seen. Note that there is a significant difference between the finest and second-finest grid sizes. Although the finest grid is not practical for this work due to the file size (Table 3.4) and solving time (Table 3.5), it's solution is compared to the second-finest (selected) grid to show that there is no significant difference in results if significantly increasing the grid size. This can be seen in the mesh convergence information of Table 3.6. It is concluded that the solutions become adequately mesh independent for this work around 3.5 million nodes for the rotor domain and 1.3 million nodes for the stator domain. General information

Stellenbosch University https://scholar.sun.ac.za

for the chosen grid sizes for Darmstadt R-1/S-1 and NASA Stage-37 can be found in Table 3.7.

Table 3.4: General grid information (Darmstadt)

#	Rotor nodes	Stator nodes	Rotor first cell height [um]	Stator first cell height [um]	file size [GB]
1	1.2M	740k	20	20	1.66
2	1.55M	740k	20	20	1.94
3	2M	850k	20	20	2.42
4	3.1M	1M	20	20	3.49
5	3.1M	1M	10	10	3.54
6	3.4M	1.25M	5	5	3.93
7	21M	10.3M	0.15	0.35	25.9

Table 3.5: Residual convergence and solving speed (Darmstadt)

#	W-mom	V-mom	U-mom	P-Mass	iterations /s/thread
1	2.11E-04	9.74E-05	3.14E-04	1.32E-05	3.10E-03
2	1.95E-04	9.05E-05	2.93E-05	1.21E-05	2.75E-03
3	1.83E-04	8.70E-05	2.83E-05	1.22E-05	2.75E-03
4	1.54E-04	7.45E-05	2.57E-05	1.12E-05	1.47E-03
5	1.95E-04	9.95E-05	4.25E-05	1.27E-05	1.47E-03
6	1.98E-04	9.77E-05	4.28E-05	1.19E-05	1.38E-03
7	1.36E-04	7.34E-05	1.50E-04	2.82E-05	2.26E-04

Table 3.6: Grid y^+ and convergence at choke (Darmstadt)

#	Mass flow [kg/s]	Isentropic efficiency	Pressure ratio	Rotor max y^+	Stator max y^+
1	16.445	0.70479	1.2859	29.6	21.7
2	16.462	0.7059	1.2865	29.6	21.6
3	16.46	0.7061	1.2865	30.0	22.3
4	16.465	0.7063	1.2864	30.0	22.3
5	16.475	0.70654	1.287	18.2	13.1
6	16.476	0.7065	1.287	11.2	7.8
7	16.486	0.7016	1.2822	1.19	0.856

Stellenbosch University https://scholar.sun.ac.za

Table 3.7: General grid information for chosen grid sizes.

	Darmstadt R-1/S-1	NASA Stage-37
Rotor domain elements	3.4 M	3.66 M
Stator domain elements	1.25 M	1.37 M
Maximum rotor y^+	11.2	11.9
Maximum stator y^+	7.8	9.8

3.4 Effect of transition modelling

From Figure 3.5 it can be seen that, as expected, the transition onset moves downstream as the grid y^+ decreases. The flow images are of the stator, with the compressor stage operating at choking mass flow rate. The magenta ISO surface is one of intermittency equal to 0.035, and intends to show the presence of laminar flow. The boundary layer transition zone moves downstream until it reaches a passage shock. The shock interaction induces laminar separation. This shock-induced transition is not to be confused with the transition region that is also found at lower mass flow rates in the same area due to large normal strain in the absence of a passage shock. Although the shock at the stator is of approximately the same strength for both the SST and $SST-\gamma Re_\theta$ solutions, the shock does not affect the turbulent boundary layer of the SST model as much as the laminar boundary layer of the $SST-\gamma Re_\theta$ model. In fact, the pre-shock Mach number reaches 1.3645 for the SST solution, whereas it reaches 1.355 for the $SST-\gamma Re_\theta$ solution. The higher pre-shock Mach number is most likely due to the thicker turbulent boundary layer produced by the SST model. This also means that the SST model predicts a lower choking mass flow rate than the $SST-\gamma Re_\theta$ model (16.47 kg/s as opposed to 16.40 kg/s). The fact that transitional effects are physically present, and noting that turbulence models with transition modelling predict a higher choking mass flow rate suggests that the choking mass flow rate predicted by the $SST-\gamma Re_\theta$ may be more accurate than that of other turbulence models due to over-predicted boundary layer blockage for the assumption of fully turbulent flow.

Observing the rotor turbulence kinetic energy in Figure 3.6, it can be seen that, at choke and at half blade span, transition on the rotor occurs at mid-chord on the suction side of the blade and near the trailing edge on the pressure side of the blade for the $SST-\gamma Re_\theta$ model. The thicker turbulent boundary layer of the SST model also results in, for example, a 22% higher turbulent kinetic energy induced into the stator free stream by the mixing plane at this height. This also affects the stator boundary layer flow. Due to the extra mesh dependency of the $SST-\gamma Re_\theta$ turbulence model, all mesh dependency studies in this thesis are performed using this model.

The understanding gained thus far regarding the effects of transition modeling on compressor models is applied and expanded on during CFD validation and dur-

Stellenbosch University https://scholar.sun.ac.za

ing the transient and steady-state results-comparison.

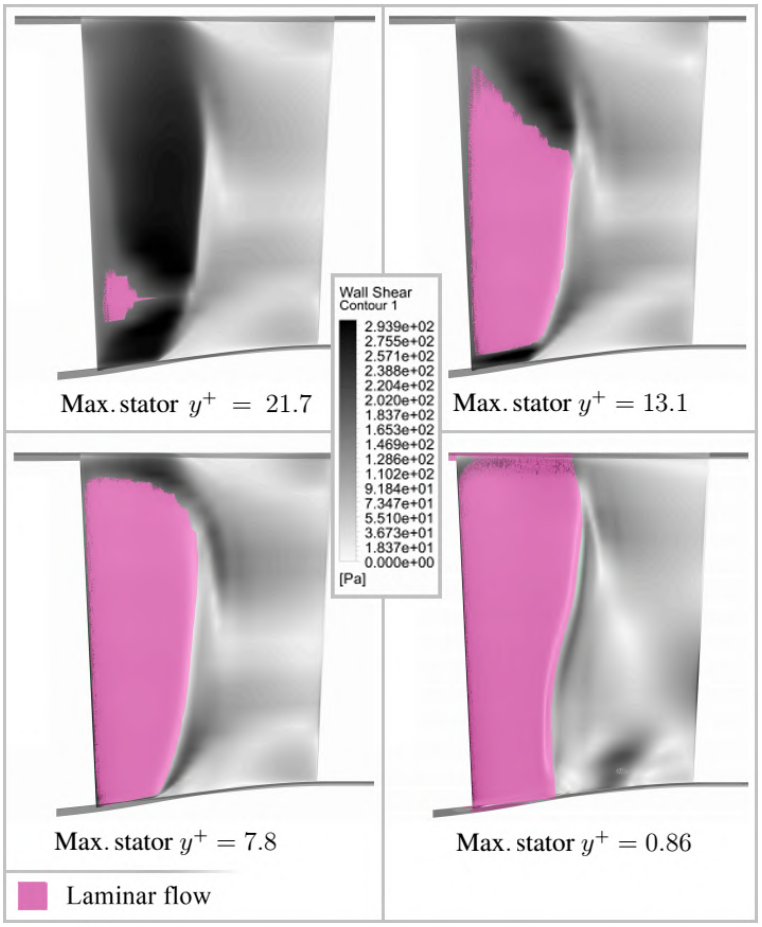

Figure 3.5: Downstream movement of stator boundary layer transition with decreasing y^+ in Darmstadt R-1/S-1 test case.

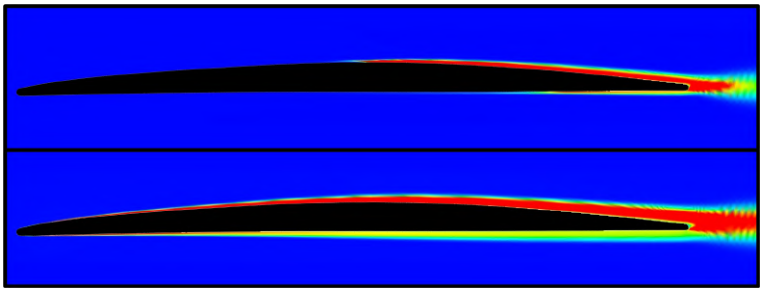

Figure 3.6: Rotor turbulent boundary layer comparison of $SST - \gamma Re_\theta$ result (top) and SST result (bottom) at half span.

Stellenbosch University https://scholar.sun.ac.za

3.5 Motivation for using the $SST - \gamma Re_\theta$ model

Following the mesh dependency study, the models were solved on the selected girds. Various turbulence models were used. The results for NASA Stage-37 are compared to experimental results by Reid and Moore (1980) of NASA's Lewis Research Center. The Darmstadt R-1/S-1 results are compared to experimental results by Müller *et al.* (2007) and Bahktiari *et al.* (2015) of TU Darmstadt.

3.5.1 Darmstadt R-1/S-1 test case

The Darmstadt performance curves of isentropic efficiency and overall pressure ratio are shown in Figure 3.7. Although it would seem that the $k-\omega$ turbulence model produces satisfactory results when observing these operating curves, the same cannot be said for the extent of expected stator flow separation on the stator. The operating point at which the oil streak lines of Figure 2.4 were allowed to settle in the stator during the experiment is unclear. The $k-\omega$ turbulence model fails to predict excessive flow separation on the stator near the operating point (Figure 3.8.b), whereas the $SST - \gamma Re_\theta$ model succeeds (Figure 3.8.a), but predicts irregular overall performance results downward from 15.3 kg/s. The $k-\epsilon$ turbulence model produces results similar to the $k-\omega$ turbulence model, but with slightly reduced separation. The SST turbulence model (no transition model) produces disappointing results with regards to the change in efficiency with mass flow rate.

The shear stress limiting coefficient has been increased such that the numerical results from the $SST - \gamma Re_\theta$ model is in closer agreement to the experimental performance curve and stator flow field separation behaviour. The $SST - \gamma Re_\theta, a_1 = 0.31$ model predicts chaotic and highly unsteady stator flow separation downward from 15.3 kg/s, with the hub corner stall region reaching 47% blade span at a near stall mass flow rate of 15.3 kg/s, compared to 35% blade span for the modified model. This is why the $SST - \gamma Re_\theta, a_1 = 0.31$ model produces an unusual performance curve, as shown in Figure 3.7, which does not agree with the experimental behaviour. A stator flow field comparison of the default and modified models at different mass flow rates (14.8, 15.2, 16 kg/s) is shown in Appendix A.3. It is concluded that the $SST - \gamma Re_\theta$ turbulence model with modified shear stress limiter $(a_1 = 0.345)$ is superior to the unmodified shear stress limiter $(a_1 = 0.31)$ with regards to predicting the experimental performance curve and the appropriate nature of flow separation on the stator. The reason for choosing $(a_1 = 0.345)$ is influenced not only by the Darmstadt results, but also the NASA Stage-37 results. Therefore, the shear stress limiting coefficient is discussed further in Section 3.6.

Although the $k-\omega$ turbulence model predicts flow separation near stall (Figure 3.8.d), the structure of this separation does not agree well with experimental results. Comparing the orientation of shear lines for the two turbulence models at the shroud corner separation (Figures 3.8.c and 3.8.d), it should be noted that the orientation of shear lines is inverted near the shroud for the $k-\omega$ turbulence model. A larger region of negative axial velocity is observed near the shroud. From the experiment

Stellenbosch University https://scholar.sun.ac.za

it should be noted that the orientation of shear lines near the shroud agrees with that of the $SST - \gamma Re_\theta, a_1 = 0.345$ model. From the downward facing shear lines of the experiment and the $SST - \gamma Re_\theta, a_1 = 0.345$ solution, it may be deduced that the experimental region of negative axial velocity for the shroud corner stall is in closer agreement with that of the $SST - \gamma Re_\theta, a_1 = 0.345$ model. Furthermore, the $k - \omega$ turbulence model fails in predicting corner stall of adequate extent at the hub for the entire operating range (Figures 3.8.b and 3.8.d).

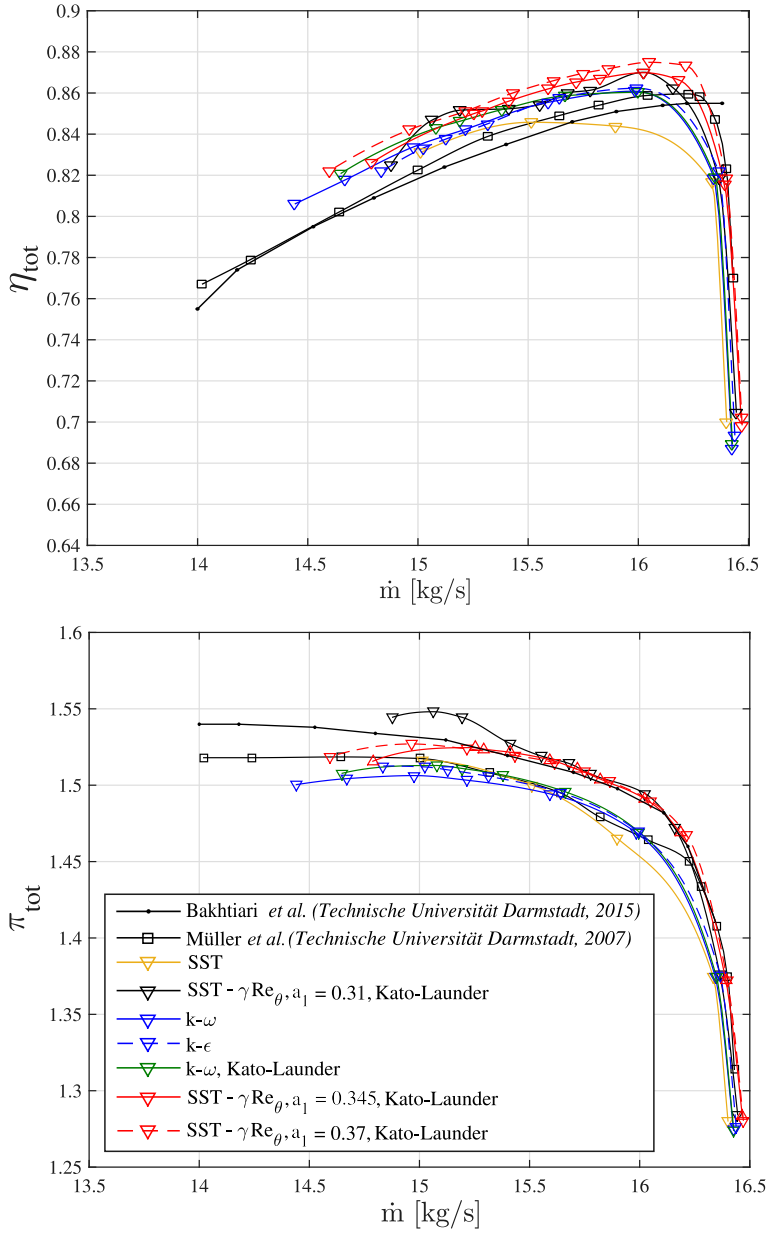

Figure 3.7: Darmstadt R-1/S-1 performance curves: isentropic efficiency (top), stage pressure ratio (bottom).

Stellenbosch University https://scholar.sun.ac.za

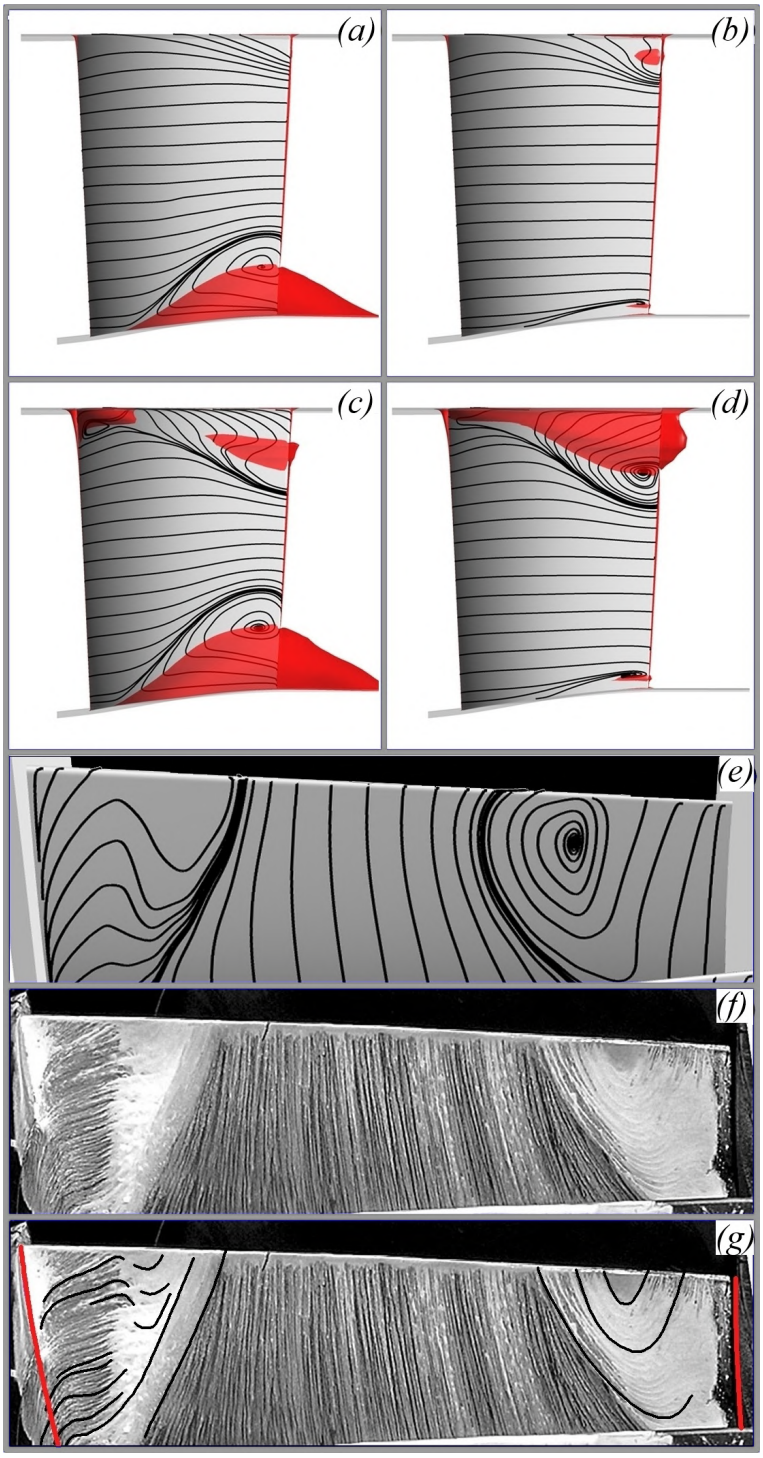

Figure 3.8: (a): $SST - \gamma Re_\theta, a_1 = 0.345$ and (b): $k - \omega$ near peak efficiency (16 kg/s). (c): $SST - \gamma Re_\theta, a_1 = 0.345$ and (d): $k - \omega$ near stall (14.8 kg/s). Red indicates regions of negative axial velocity. Numerical (e) and experimental (f) stator shear lines. The interpretation of experimental stator shear lines (g).

Stellenbosch University https://scholar.sun.ac.za

3.5.2 NASA Stage-37 test case

The NASA Stage-37 performance curves can be found in Figure 3.9. For NASA Stage-37, the $k-\epsilon$ and $k-\omega$ turbulence models yield results which seem superior to those of the SST turbulence model, with or without a transition model. Additional performance curves for NASA Stage-37 can be found in Appendix A.4.

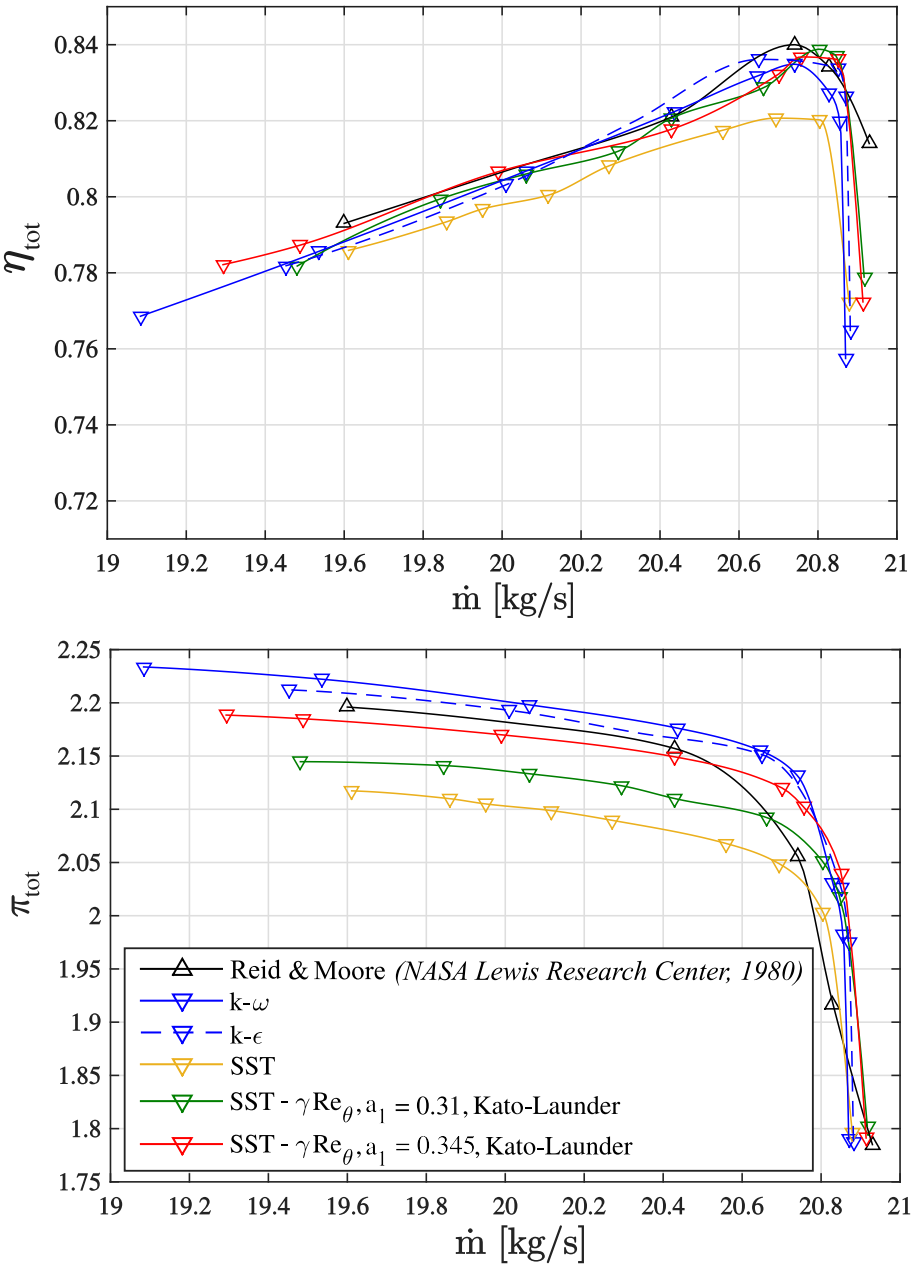

Figure 3.9: NASA Stage-37 performance curves: stage isentropic efficiency (top), stage pressure ratio (bottom).

Stellenbosch University https://scholar.sun.ac.za

Upon inspection of the flow field, it can be seen that a separation region caused by shock induced boundary layer separation on the suction side of the rotor blade is far larger for the SST turbulence model than for the $k-\epsilon$ and $k-\omega$ turbulence models (Figure 3.10). Upon enabling the transition model, the size of this over-predicted separation region by the SST turbulence model decreases (Figure 3.10 (c)), allowing the pressure ratio to increase.

The rotor bow-shock interacting with the suction side boundary layer is weaker for the Darmstadt test case due to its higher pitch (fewer blades) and lower inlet tip relative Mach number. The aspect ratio of the Darmstadt stage is such that the rotor-bow shock intensity, which is also a function of distance from the emanation, decreases more severely along a spanwise hub to tip fraction in the direction of the hub. Additionally, adverse pressure gradient on the rotor blade suction side boundary layer is less severe for the Darmstadt test case due to lower blade loading. This can be observed in the rotor blade loading charts of Figure 3.11.

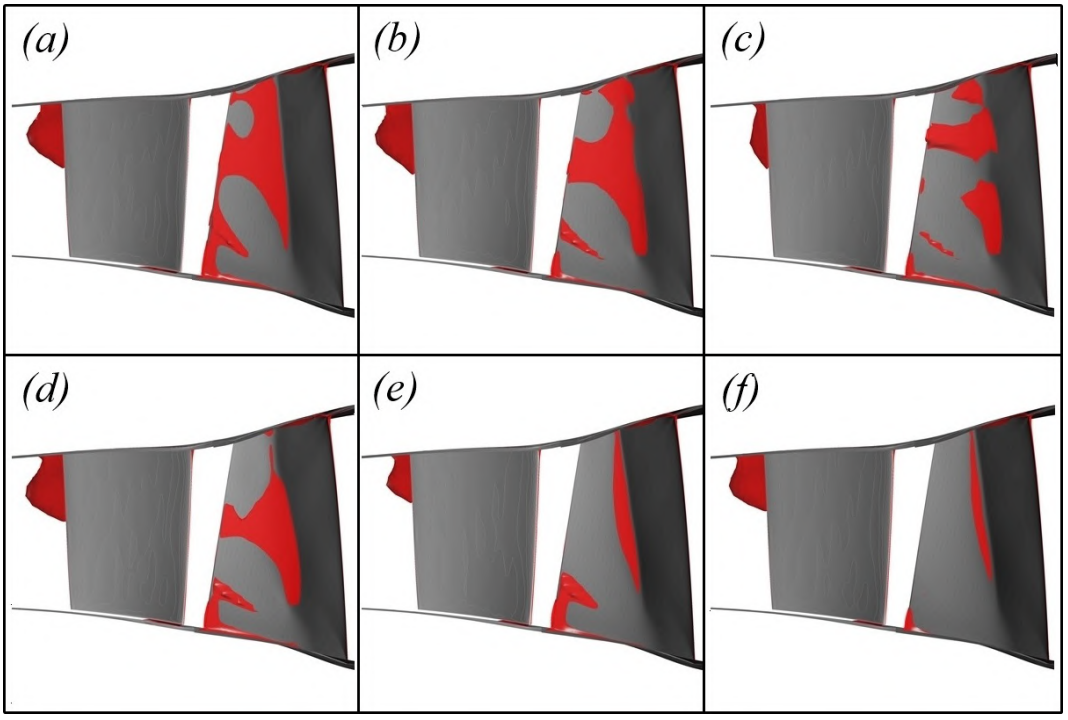

Figure 3.10: Shock induced boundary layer separation at 20 kg/s on NASA Stage-37 rotor blade suction side. (a): SST, (b): $SST-\gamma Re_\theta, a_1 = 0.31$ + Reattachment Production. (c): $SST-\gamma Re_\theta, a_1 = 0.31$. (d): $SST-\gamma Re_\theta, a_1 = 0.345$. (e): $k-\omega$. (f): $k-\epsilon$.

Stellenbosch University https://scholar.sun.ac.za

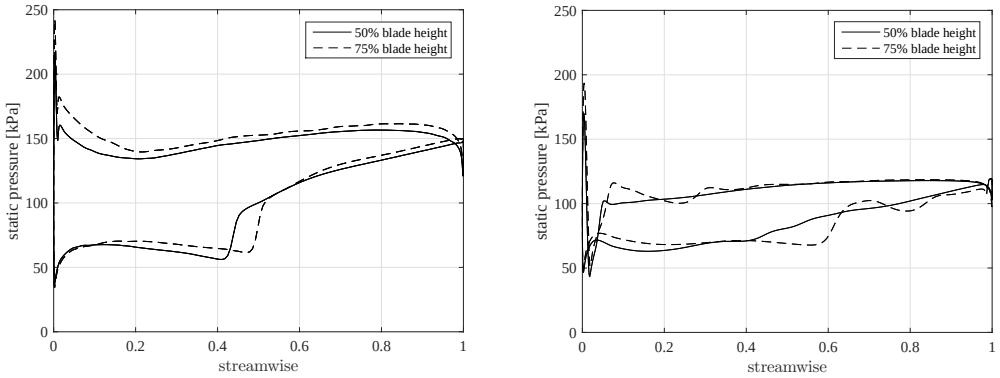

(a) NASA Stage-37 (b) Darmstadt R-1/S-1

Figure 3.11: Blade loading comparison at 50% and 75% blade height near operating points ($k-\omega$ turbulence model).

Due to this weaker shock and adverse pressure gradient, the shock induced separation is not sustained for the Darmstadt case, regardless of the turbulence model. For the Darmstadt case, the $k-\omega$ turbulence model predicts no shock induced boundary layer separation. Minor shock induced boundary layer separation is predicted by the $SST-\gamma Re_\theta, a_1 = 0.31$ model, and reattachment occurs immediately after the separation (Figure 3.12).

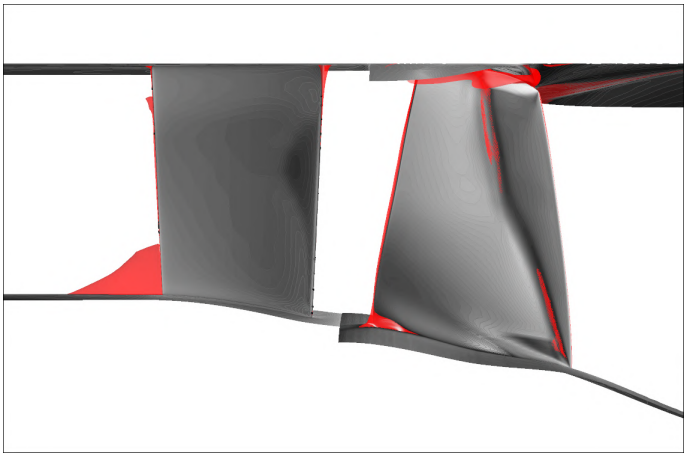

Figure 3.12: Darmstadt compressor near stall, showing minor shock induced boundary layer separation for the $SST-\gamma Re_\theta$ model with $a_1 = 0.345$.

Due to the significantly under-predicted pressure ratio by the SST and $SST-\gamma Re_\theta, a_1 = 0.31$ models in the NASA test case, it becomes apparent that this is due to over-predicted shock induced boundary layer separation on the blade suction side of NASA Stage-37. However, as seen in the Darmstadt test case, the γRe_θ transition model is required for the adequate flow behaviour in some regions of moderate

Stellenbosch University https://scholar.sun.ac.za

normal strain in the subsonic regime, such as the stator. Transition modelling is also important for predicting the choking mass flow rate. The choking mass flow rate is influenced by boundary layer blockage and separation behaviour, both of which are affected by transitional effects.

3.6 Adapting the shear stress limiter

The amount of shear stress in the boundary layer may be increased in order to reduce flow separation. Noting that the SST turbulence model contains a shear stress limiter, it might be possible solve this problem by reducing it's effect. The limiter cannot simply be disabled, since it is required for modelling the stator flow field. The amount of turbulent shear stress in the boundary layer can be controlled by varying the structure parameter, a_1. According to Tharwat *et al.* (2016), the SST turbulence model performs well for mild adverse pressure gradients in subsonic flows and is designed to successfully predict separation where the majority of two-equation models fail to do so. Tan *et al.* (2011) states that, in some cases, the SST turbulence model fails to accurately predict flow fields with strong shock/boundary layer interaction (large normal strain). In the work by Tan *et al.* (2016), where the shear stress limiter strength is adapted to suit Mach 2.8 and Mach 5 experimental shock wave turbulent boundary layer interaction (SWTBLI) test cases, they conclude that a constant value of stress limiter is not sufficient. Tan *et al.* (2011) hypothesises that the shear stress limiter could be made a function of the flow variables and that more validation test cases are required.

Tharwat *et al.* (2016) mentions a recent SWTBLI workshop for a Mach 5 compression corner problem for which a value of a_1 equal to 0.356 has been found appropriate. In the work of Tharwat *et al.* (2016) the standard SST turbulence model over-predicts shock induced boundary layer separation in a dual throat nozzle problem. A value of a_1 equal to 0.34 was found to be appropriate in order to match experimental results. In the present work, a value for the structure parameter which yields satisfactory results for both NASA Stage-37 and Darmstadt R-1/S-1 is to be found. The effect of this value on the overall performance of the client-specified multi-stage compressor is investigated in Section 4.3 of the next chapter.

The structure parameter (a_1) can be related to the shear stress limiting coefficient, C_{lim}, by

$$a_1 = \frac{1}{C_{lim}}\sqrt{\beta^*} \tag{3.3}$$

where the model coefficient $\beta^* = 0.09$. If $C_{lim} \to 0$, Menter's SST turbulence model becomes the Menter BSL model, which is a predecessor of Menter's SST turbulence model. The SST turbulence model corresponds to $C_{lim} = 1$. An elaborate discussion on the structure parameter can be found in Tharwat *et al.* (2016).

If the structure parameter is increased, the separated volume decreases (Figure 3.10 (d)). As expected, this results in a higher pressure ratio. Note that a separation bubble of significant volume over the upper part of the blade, where higher blade

Stellenbosch University https://scholar.sun.ac.za

loading occurs, is eliminated. After comparing performance curves of the two different test cases evaluated with values of a_1 ranging from 3.3 to 3.7, it was decided that a value of a_1 equal to 0.345 is adequate for both Darmstadt R-1/S-1 and NASA Stage-37.

3.7 Concluding remarks

With the adapted shear stress limiter, adequate separation behaviour with regards to flow structure is predicted on the Darmstadt stator, whilst suppressing seemingly premature chaotic corner stall which starts at 15.3 kg/s for the unmodified model. Furthermore, the performance curves for both test cases are in close agreement with experimental results.

For the Darmstadt test case and with the adapted shear stress limiter, the experimental (Müller *et al.*, 2007) and numerical performance curves for stage pressure ratio and stage isentropic efficiency differ by approximately 1.8% and 1.5% at the operating point, respectively. In comparison to the experimental results by Bakhtiari *et al.* (2015), the stage pressure ratio and efficiency differ by approximately 0.1% and 2.0% at the operating point. For the NASA test case, the experimental (Reid & Moore, 1980) and numerical stage pressure ratio and stage isentropic efficiency differ by approximately 0.8% and 0.3%, respectively. It may be suggested that the value of a_1 can be increased even more, since the experimental pressure ratio has not yet been reached, and since the experimental Darmstadt stator shows less separation than the numerical solution. However, if it is increased by too much (for example $a_1 = 0.37$), the isentropic efficiency of the Darmstadt compressor increases, shifting the numerical solution away from experimental results. It should be kept in mind that surface roughness is not considered in the current test case study. Depending on the sensitivity of shock induced boundary layer separation to surface roughness, further investigation might show that the numerical Darmstadt performance curves move closer to experimental data while the numerical operating curves for the NASA case stay relatively constant due to the difference in numerically predicted shock induced separation between the two test cases. It is also concluded that the appropriate value of the structure parameter in compressor CFD is case-specific.

Furthermore, it is concluded that the choking mass flow rate of a compressor is better predicted when a transition model is used. Results suggest that turbulence models without transition modelling over-predict blockage because of the omitted laminar boundary layer flow present in the experiment.

Stellenbosch University https://scholar.sun.ac.za

Chapter 4

Main Numerical Investigation

In Section 4.1, the Darmstadt R-1/S-1 test case is considered for a comparison between transient and steady-state results for a single stage. The insight gained is useful for doing a comparison between steady-state and transient overall performance results for the proprietary multi-stage compressor. The mesh dependency study for this proprietary multi-stage compressor geometry is shown in Section 4.2, and the compressor map is given in Section 4.3. To maintain confidentiality, all multi-stage compressor results are non-dimensionalised with respect to a given design point. In Section 4.5, the effect of blade and endwall roughness on the proprietary multi-stage compressor is investigated. Lastly, the effect of blade fillets on the proprietary multi-stage compressor is investigated in Section 4.6. In the current work, the effects of fillets and surface roughness are studied in isolation.

4.1 Test case transient and steady-state comparison

Fundamental differences between transient and steady-state results are investigated in order to understand the significance of transient analysis at a steady operating point (not near numerical stall).

The $SST - \gamma Re_\theta$ model is used on a grid with a maximum stator y^+ of 7.8. As discussed in Section 2.5.2 and 3.4, although this is not ideal for the $SST - \gamma Re_\theta$ model, the model can still be used on this grid and the transition zone on this grid is close to the final location, which was shown by the $y^+_{max} \sim 1$ solution. It is not the purpose of this section to investigate particulars about the exact location of the transition zone. For such an investigation, a maximum y^+ value of ~ 1 is required. Keeping in mind that the transient and steady-state comparison is also performed for the multi-stage compressor, a grid with a maximum y^+ value of ~ 1 is not practical for the current work.

In order to start with the fundamental differences, a single passage transient solution at a single time step is compared to a steady-state mixing plane model. The models are solved at the choking mass flow rate in order to obtain a complex stator flow field.

Stellenbosch University https://scholar.sun.ac.za

Since there are no time dependencies upstream of the rotor, no significant difference in the rotor flow fields aside from upstream-travelling interactions from the stator is expected. Therefore, the investigation focuses on the stator flow field (Figure 4.1).

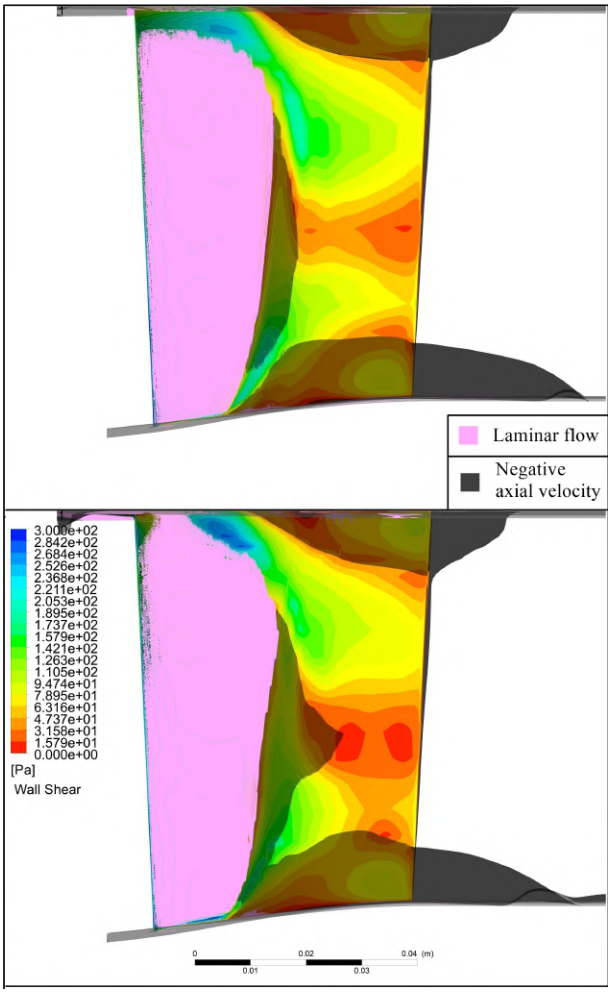

Figure 4.1: Stator pressure side boundary layer flow field of the mixing plane model (top) and transient model (bottom). Featuring wall shear stress contours, a transparent ISO surface of negative axial velocity, and a magenta ISO surface of low turbulence intermittency (0.035) to indicate the presence of nearby laminar flow.

A notable difference in the results is that the stator laminar boundary layer for the transient solution extends toward the shroud, whereas it does not for the mixing plane model. This time dependency stems from the tip vortex structure, which is destroyed by the mixing plane (Figure 4.2). For the transient model, time dependent pressure and shear variations occur at the stator shroud. At the hub, the first two notable differences in the results are the presence of a turbulent boundary layer leading to a region of local high wall shear stress, and the joining of the laminar

Stellenbosch University https://scholar.sun.ac.za

separation bubble with the end wall separation for the transient solution (Figure 4.3).

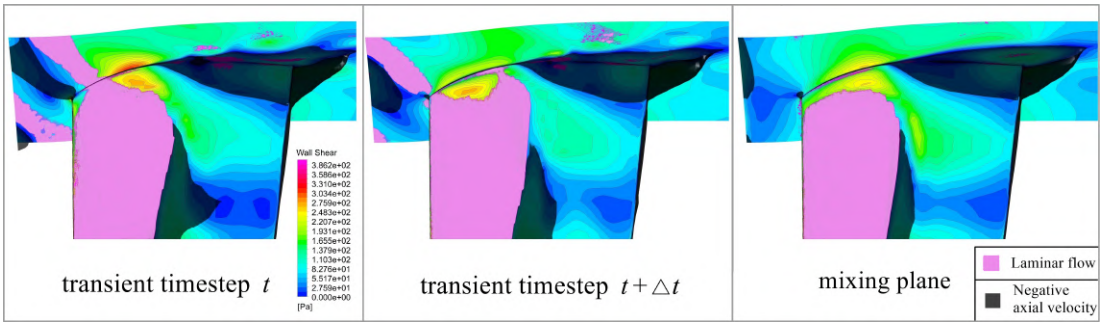

Figure 4.2: The magenta ISO surface is of turbulence intermittency equal to 0.035 to indicate the presence of nearby laminar flow. The transparent ISO surface shows negative axial velocity.

The discrepancy between the mixing plane and transient models near the hub (Figure 4.3) is caused by a difference in the way in which the endwall boundary layer is treated at the rotor-stator interface. For the transient solution, the turbulent boundary layer from the rotor domain is transferred directly to the stator domain, and the turbulent kinetic energy of this boundary layer is concentrated sufficiently at the endwall to achieve local removal of the laminar boundary layer. This is shown in Figure 4.4. As the turbulent boundary layer approaches the stator laminar boundary layer, the turbulent kinetic energy is absorbed. If this dissipation is sufficient, the laminar boundary layer of the stator is locally removed, as is the case for the transient solution (Figure 4.4 (c)).

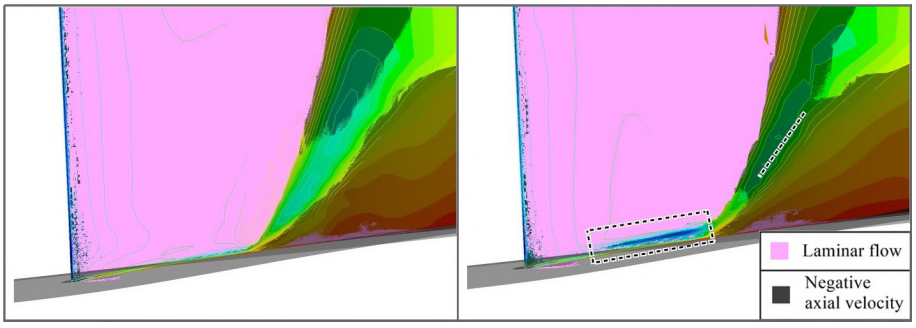

Figure 4.3: The stator pressure side boundary layer flow field of the mixing plane model (top) and transient model (bottom) showing two notable differences (dotted line).

For the mixing plane model, the turbulent kinetic energy from the rotor flow field endwall boundary layer is dispersed, leading to a region of interaction that spans a greater radial distance than for the transient solution. This higher free

Stellenbosch University https://scholar.sun.ac.za

stream turbulent kinetic energy is the reason why the laminar separation bubble does not join with the endwall separation for the mixing plane solution , whereas it does for the transient solution. It is caused by thinning of the laminar boundary layer for the mixing plane model for which the endwall turbulent kinetic energy is radially dispersed. The dispersion of turbulent kinetic energy over this region prevents separation close to the endwall, that would lead to the joining of the laminar separation bubble and endwall separation. For this part of the laminar boundary layer, transition can now occur without separation.

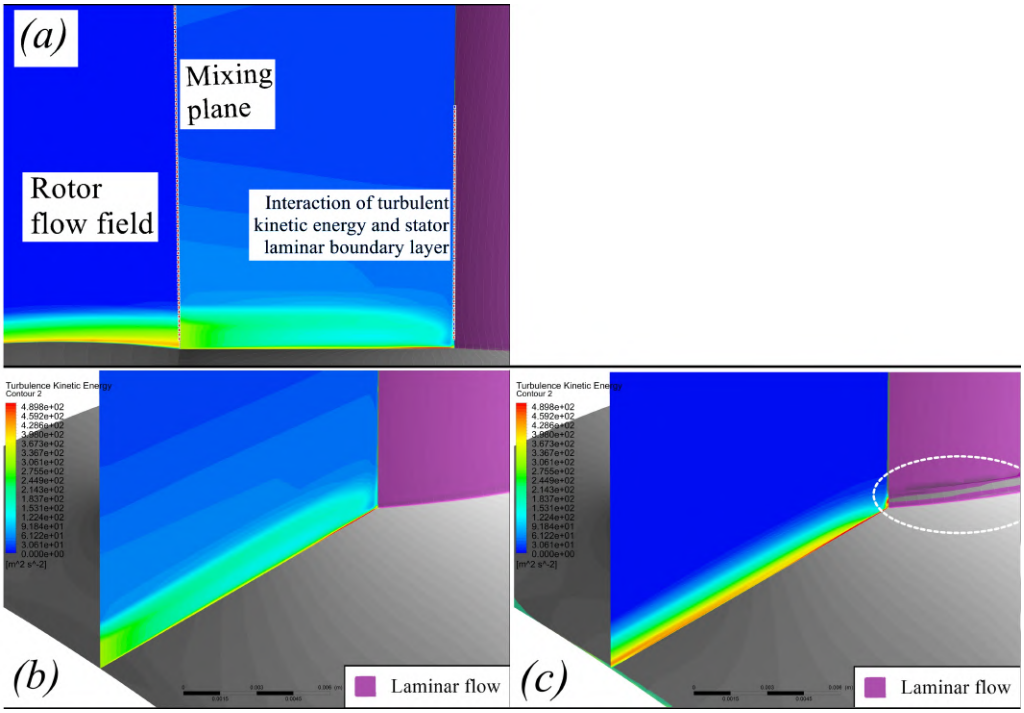

Figure 4.4: (a): Mixing plane model showing radial dispersion of endwall turbulent boundary layer turbulent kinetic energy. (b): Unconcentrated endwall turbulent boundary layer of mixing plane model fails to locally remove stator laminar boundary layer. (c): Concentrated endwall turbulent boundary layer of transient solution locally removes stator laminar boundary layer near endwall.

The boundary layer thickness in the applicable region is compared for the two models in Figure 4.5. For visual context, the location of the plane (12 cm from the axis) used for Figure 4.5 can be seen in Appendix B.1.

A further difference in the results is that the mixing plane model velocity boundary layer starts at the leading edge of the hub, leading to high shear stress at the hub stator leading edge. This leads to higher pressure losses at the hub, causing a smaller stagnation point at the stator leading edge since the fluid has already been slowed down. This is can be seen in Figure 4.6.

Stellenbosch University https://scholar.sun.ac.za

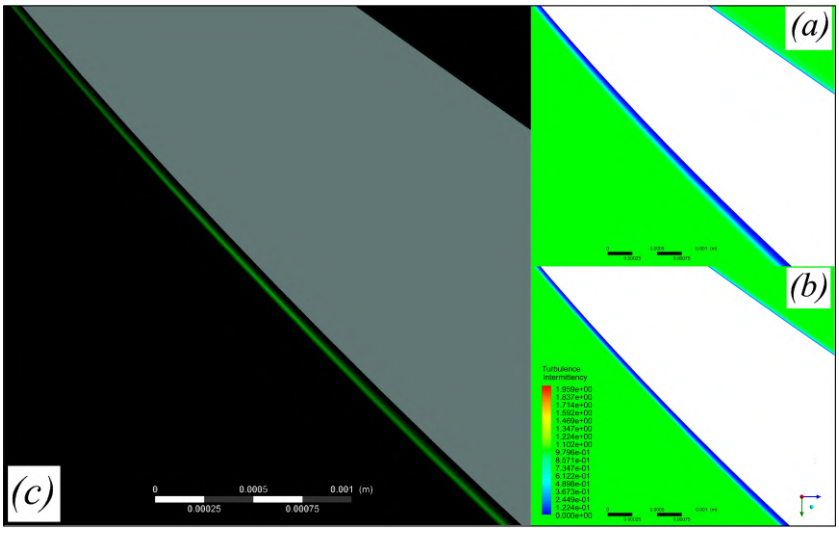

Figure 4.5: Comparison of laminar boundary layer thickness. (a): Transient model. (b): Mixing plane model. (c): Difference between (a) and (b).

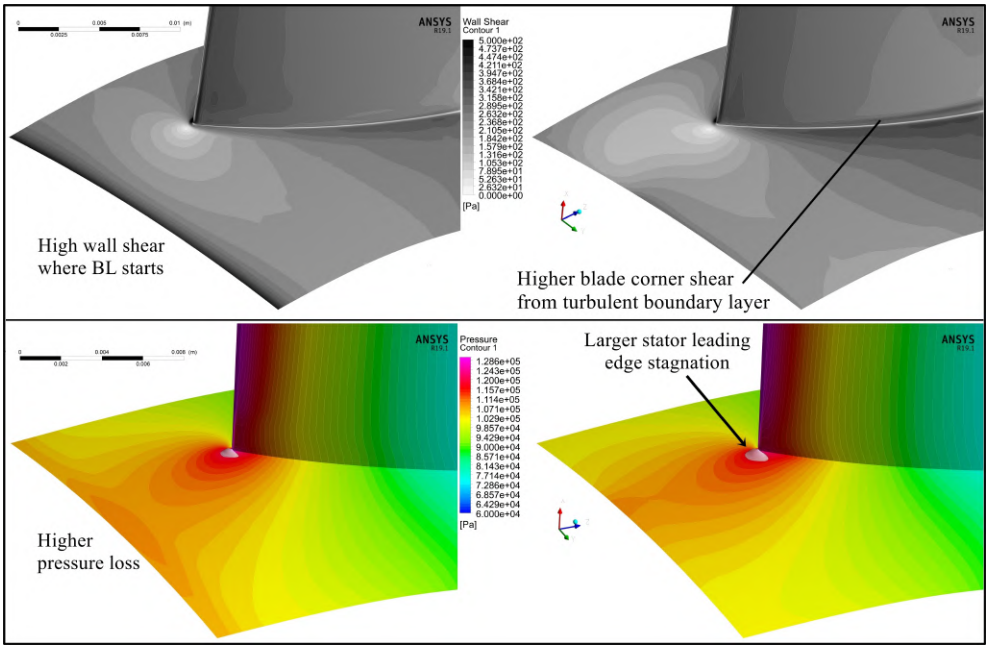

Figure 4.6: This figure illustrates the difference in wall shear (top half) and pressure (bottom half) distribution between the mixing plane (left) and transient (right) models.

In Figure 4.7, it can be seen that the rotor flow at the hub slows down prior to flowing over the non-rotating stator hub. This low momentum fluid (red ISO surface of 10 m/s in Figure 4.7) joins with the rotor wake, and extends into the stator domain, creating stretched wall shear contours. This particular difference in

Stellenbosch University https://scholar.sun.ac.za

the results is dependent on the rotor rotation-position relative to the stator at a fixed time step.

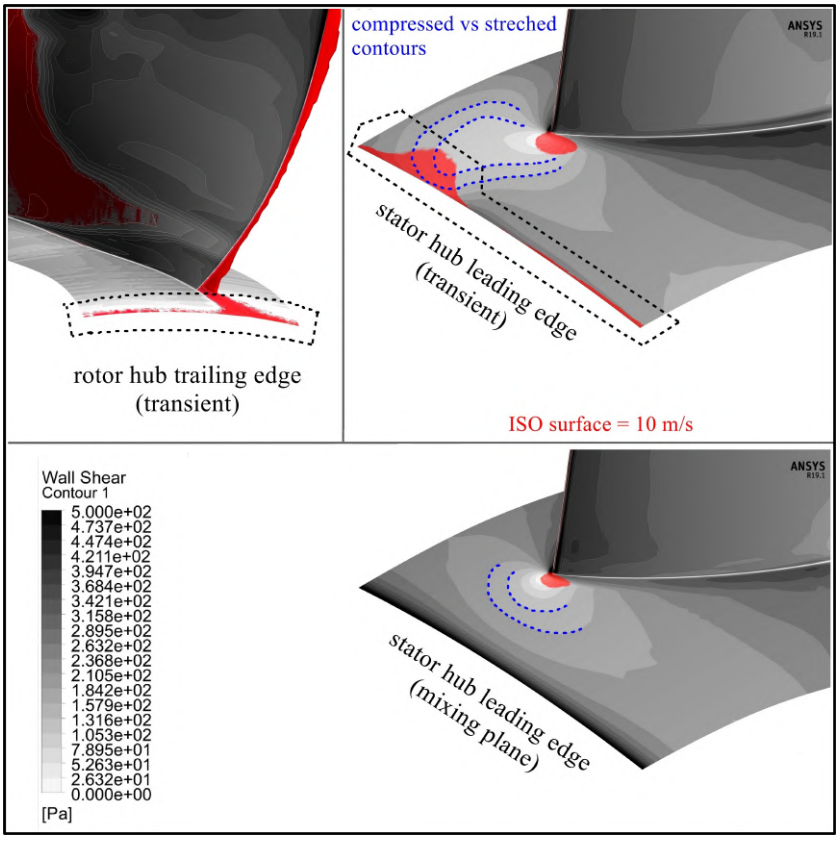

Figure 4.7: Transient (top) and mixing plane (bottom).

It is apparent that the additional time dependencies inherent to the transient solution would have a significant effect on the transient results, when only considering a single passage. This can be seen in Figure 4.8, which shows the time dependent total to total isentropic efficiency for a single and a multi-passage transient model. The multi-passage model has two rotor passages and three stator passages. The model is set up such that the rotor moves by one passage every 20 time steps (at design speed, the resulting time step size is 9.375e-06 s). The variation in isentropic efficiency is more for a single-passage, with the signal period being 20 time steps, or one passage pass. Since a stage is normally designed to prevent resonance, the relative position of each rotor passage to that of a stator passage is unique when solving at fixed time steps. This is why considering more passages is essential for transient analysis, but makes no difference for steady-state mixing plane analysis. Due to the difference in relative rotor-stator positions, an irregular signal with a lower amplitude is obtained. It is therefore likely that the amplitude will decrease further if more passages are considered.

Stellenbosch University https://scholar.sun.ac.za

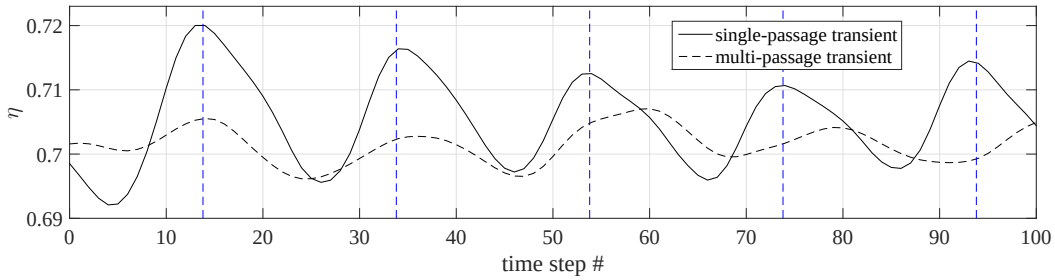

Figure 4.8: Isentropic efficiency output comparison for a single-passage and multi-passage model. A period of 20 time steps (one passage passing) is indicated with blue dotted lines.

The steady-state efficiency output (not shown) varies irregularly between 69.6% and 71.5%. Therefore it may be suggested that a more reliable answer can be obtained with a transient model if the transient solution output varies within a lower amplitude and keeping in mind the nature of the differences between transient and steady-state results. There is no significant difference in transient and steady-state efficiency or pressure ratio at this operating point.

As determined at the hub, averaging at the mixing plane can have an effect on, for example, the pressure distribution. Naturally, this would also affect subsonic regions of the rotor flow. This discrepancy between mixing plane and transient results is demonstrated in Figure 4.9.

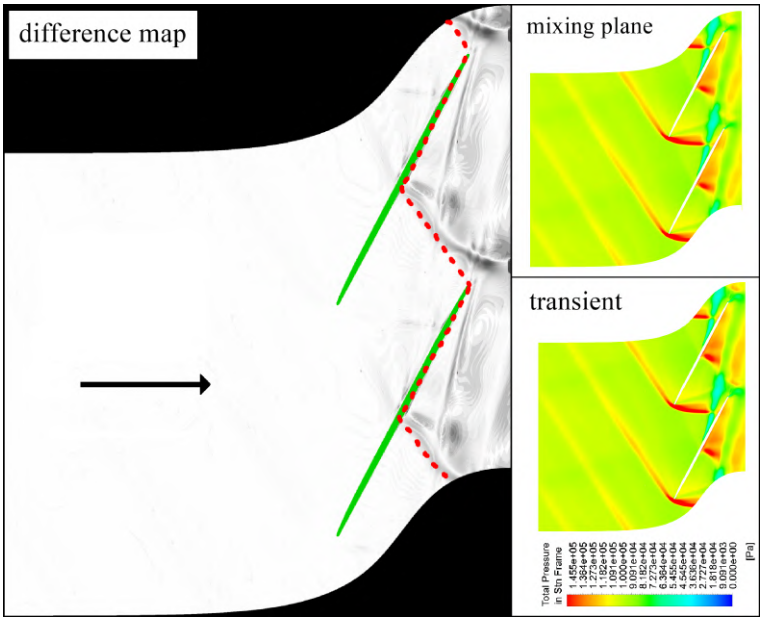

Figure 4.9: Difference map between transient and steady-state (mixing plane) total pressure in stationary frame at 97% span. High subsonic flow exists downstream of the dotted line.

Stellenbosch University https://scholar.sun.ac.za

Lastly, since the output of each passage is unique due to a unique relative rotor-stator position, and since pressure waves can travel upstream toward the rotor passage shock from the stator, variations occur between rotor passages. Figure 4.10 shows the shift in pressure contour position between two neighbouring transient passages. As expected, the most significant variations occur after the passage shock.

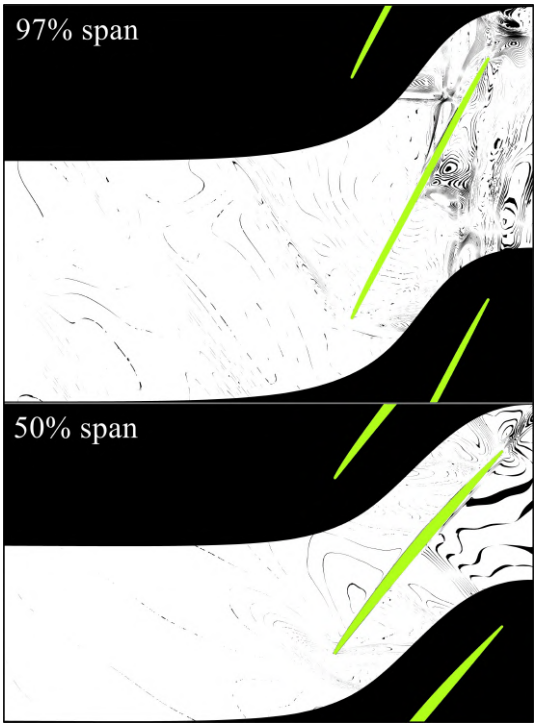

Figure 4.10: The shift in pressure contour position from one passage to the next at 97% and 50% blade span.

4.2 Multi-stage compressor mesh

A mesh dependency study is performed on the proprietary multi-stage compressor geometry. The mesh dependency study was performed at the choking mass flow rate and at 100% of the design speed, using the $SST - \gamma Re_\theta$ turbulence model. The study was also performed for a case with extreme relative Mach numbers throughout the compressor (115% of design speed) and a case with predominantly subsonic flow in the first 3 stages (70% of design speed), with the same conclusions. The considered mesh sizes can be seen in Table 4.1. The change in mass flow rate, total pressure ratio, and total to total isentropic efficiency relative to the result produced by the first mesh can also be seen in Table 4.1. It should be noted that the results file size in Table 4.1 is for a single passage simulation. This is a post processing and storage space consideration, and is especially important for intermediate multi-passage transient results. The ratio at which the first cell height decreases through

Stellenbosch University https://scholar.sun.ac.za

the respective stages compensates for the increase in y^+. Due to the problem size, a mesh with a maximum y^+ of ~ 1 is not practical. It should also be kept in mind that the solution is to be compared with a transient solution, which will consider multiple passages. Even though the maximum y^+ on rotor-1 is 2.3 for the last mesh, the average y^+ is 0.3. The average y^+on stator-1 for this mesh is 0.2. The y^+ values for each rotor and stator can be seen in Table 4.2. The grid first cell height and the attained convergence levels for continuity and mass conservation with a pseudo transient time step factor of 0.5 can be seen in Appendix B.2. It is concluded that the solution becomes adequately mesh independent at a total of 8.33 million elements.

Table 4.1: General grid information and convergence

#	Nodes /rotor	Nodes /stator	Total nodes	Total elements	Size [GB]	$\dot{m}$	π_{tot}	η_{tot}
1	220-270 k	180 k	1.70 M	1.56 M	1.55	1.0000	1.0000	1.0000
2	360-430 k	220 k	2.43 M	2.26 M	2.21	1.0020	0.9681	0.9578
3	370-460 k	220 k	2.55 M	2.37 M	2.31	0.9977	1.0023	1.0244
4	490-620 k	220 k	3.15 M	2.95 M	2.83	0.9952	0.9580	0.9862
5	700-870 k	280 k	4.23 M	4.00 M	3.80	0.9948	0.9868	1.0160
6	0.95-1.17 M	330 k	5.60 M	5.34 M	5.00	0.9960	0.9654	0.9814
7	0.95-1.17 M	440 k	6.05 M	5.77 M	5.38	0.9963	0.9796	0.9954
8	1.47 M	630 k	8.68 M	8.33 M	7.68	0.9968	0.9556	0.9592
9	1.75 M	630 k	9.94 M	9.58 M	8.76	0.9963	0.9524	0.9594
10	2.3 M	830 k	13.15 M	12.73 M	11.56	0.9962	0.9589	0.9594

Table 4.2: Grid y^+ for per rotor / stator

#	max y^+ rotor-1	max y^+ rotor-2	max y^+ rotor-3	max y^+ rotor-4	max y^+ stator-1	max y^+ stator-2	max y^+ stator-3	max y^+ stator-4
1	103	112	120	120	96	132	135	128
2	111	114	123	123	98	141	140	133
3	61	63	64	77	55	76	71	69
4	34	34	35	38	30	6	37	36
5	18	19	19	21	16	20	19	19
6	19	20	19	21	17	21	19	19
7	19	20	19	21	17	21	19	19
8	11	12	11	12	9	11	10	10
9	4.2	4.1	4.3	4.4	2.5	2.7	2.5	2.3
10	2.3	2.4	2.5	2.6	1.1	1.1	1.1	1

Stellenbosch University https://scholar.sun.ac.za

4.3 Baseline multi-stage compressor map

The baseline (no surface roughness, no fillets) compressor speedlines in Figure 4.11 were simulated such that the CFD model stalled to the nearest 1 kPa of the varied static pressure outlet. This means there is variability in terms of closeness to numerical stall inception of each speedline. This also means that it may be possible to obtain solutions at lower mass flow rates for each speedline by searching for the point of stall inception using smaller increments of static outlet pressure. When numerical stall is reached, the mass flow rate becomes unstable in the time domain and decreases toward 0, with the solution diverging before this can happen. The $k-\omega$ turbulence model, which is also required for the roughness comparison, is used for the baseline compressor map simulation, keeping in mind the number of solutions and the fact that it is a single-passage mixing plane simulation. The $k-\omega$ turbulence model performed well with regards to overall performance in the test cases.

4.3.1 Discussion of results

In the test cases it was seen that the $k-\omega$ model produces a solution with a lower choking mass flow rate than the $SST-\gamma Re_\theta$ model, even though more flow separation is observed with the $SST-\gamma Re_\theta$ model due to the shear stress limiter. In the test cases, the laminar boundary layer flow present on the rotor and stator for the $SST-\gamma Re_\theta$ compensated for the increased flow separation, reducing the blockage. In a multi-stage compressor the flow is highly turbulent downstream of the first stage, leading to negligible areas of laminar boundary layer flow in downstream stages. This is why the choking mass flow rate is more rather than less when comparing a $k-\omega$ and a $SST-\gamma Re_\theta$ solution for the multi-stage compressor at design speed. This is not the case for 93% speed, at which less flow separation is observed. When comparing the $SST-\gamma Re_\theta$ and SST solutions, the transition model reduces corner stall. This was also seen during CFD validation. The transition model allows for significant laminar boundary flow in the first stage. At design speed, the choking mass flow rate of the $SST-\gamma Re_\theta$ solution is 0.2% less than that of the $k-\omega$ solution. If the shear stress limiting coefficient of the $SST-\gamma Re_\theta$ model is increased from 0.31 to 0.345, areas of separation decrease such that the choking mass flow rate is only 0.05% less than that of the $k-\omega$ solution. The SST (no transition model) solution choking mass flow rate is 0.6% less than that of the $k-\omega$ solution. During CFD validation it was concluded that the SST model most likely over-predicts flow separation and therefore blockage. At 93% shaft speed, the choking mass flow rate of the $SST-\gamma Re_\theta$ solution is still 0.2% less than that of the $k-\omega$ solution, but as in the validation test cases, the choking mass flow rate of the $SST-\gamma Re_\theta$ model with $a_1 = 0.345$ is now more than that of the $k-\omega$ solution (+0.33%). This is because the blockage is less dependent on flow separation when reducing the shaft speed from 100% speed where flow separation is rather significant. This is analogous to what is observed during the roughness investigation.

Stellenbosch University https://scholar.sun.ac.za

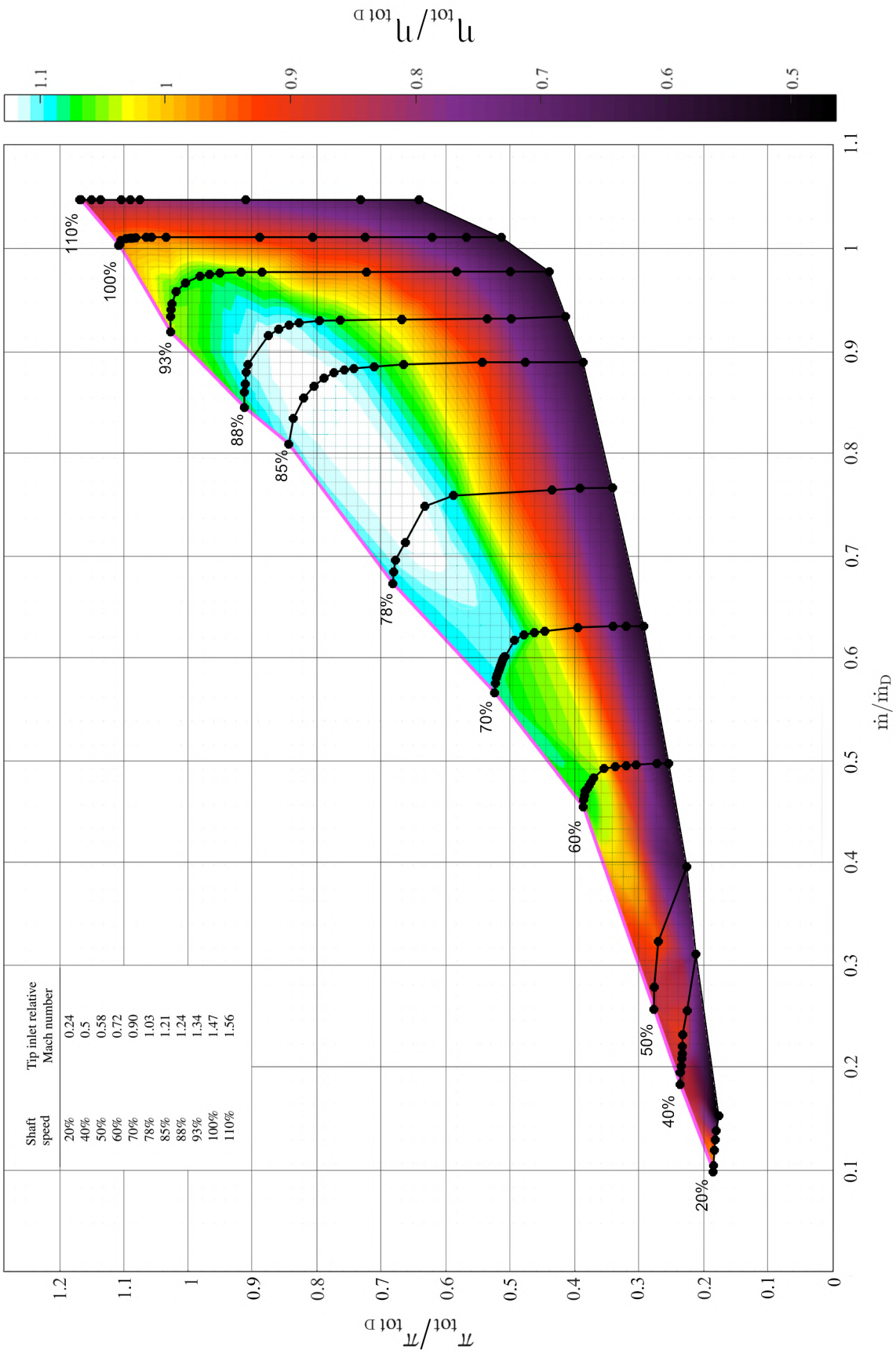

Figure 4.11: Multi-Stage compressor speedlines ($k-\omega$ turbulence model).

Stellenbosch University https://scholar.sun.ac.za

A comparison of the $k-\omega$ and $SST-\gamma Re_\theta, a_1 = 0.345$) results at 93% speed can be seen in Figure 4.12. The mass flow rate of the performance curves of Figure 4.12 are non-dimensionalised with respect to the choking mass flow rate of the $SST-\gamma Re_\theta, a_1 = 0.345$ solution.

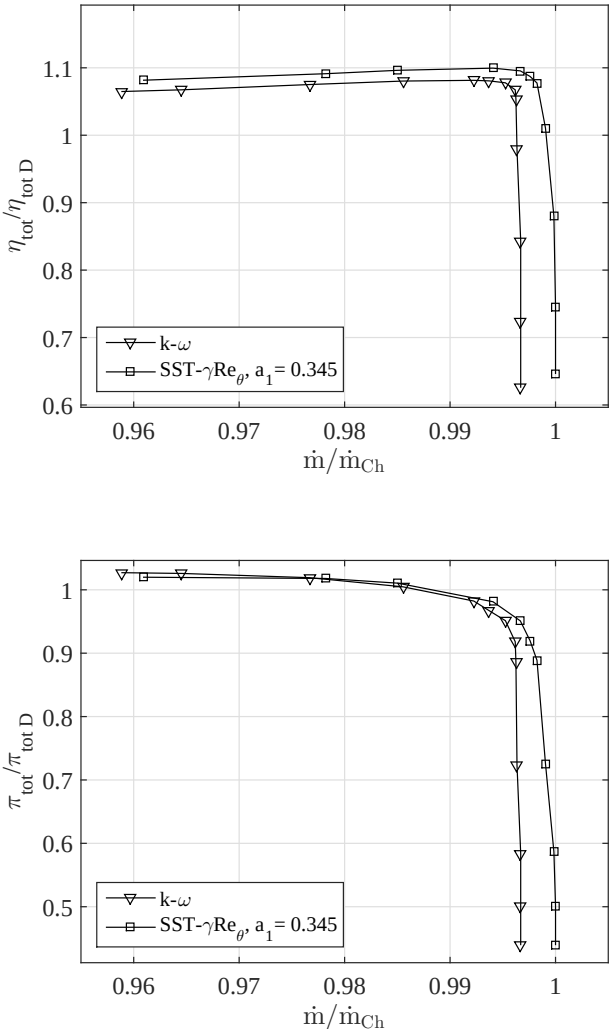

Figure 4.12: Comparison of $k-\omega$ and modified $SST-\gamma Re_\theta$ solution performance curves at 93% speed (not simulated to numerical stall) showing isentropic efficiency (top) and stage pressure ratio (bottom).

With regards to pressure ratio, the $k-\omega$ and $SST-\gamma Re_\theta, a_1 = 0.345$ solutions show similar results, with the SST and $SST-\gamma Re_\theta, a_1 = 0.31$ models showing reduced blade loading, but similar or slightly higher (+0.35% for the $SST-\gamma Re_\theta, a_1 = 0.31$ model) total to total isentropic efficiency. This is analogous to what was observed for the test cases. At 93% speed, maximum pressure ratio of the $SST-\gamma Re_\theta, a_1 = 0.345$ solution is only 0.8% less than that of the $k-\omega$ solution. In contrast to this, the predicted pressure ratio by the $SST-\gamma Re_\theta, a_1 = 0.31$

Stellenbosch University https://scholar.sun.ac.za

model is 6.2% less than that of the $k-\omega$ solution. Similar to what was observed during the NASA test case, for which strong shock-interactions also occur, this significant difference is due to a reduction in suction-side shock-induced boundary layer separation when increasing the shear stress limiter. Following the conclusions of the test cases, the $k-\omega$ solution and the $SST-\gamma Re_\theta, a_1 = 0.345$ solution should best match physical results.

4.4 Multi-stage transient and steady-state comparison

Continuing from the test case transient and steady-state comparison of Section 4.1, a comparison is performed on the proprietary multi-stage compressor at the design point and at an off design operating point with the $SST-\gamma Re_\theta$ model on the selected grid. It is not practical to consider a grid with a y^+ value of ~ 1 for this simulation because the solving time would not be justifiable when keeping in mind that it is not the purpose of this investigation to solve for a high-fidelity solution (no fillets, no surface roughness). In this transient multi-passage simulation, 3 rotor passages and 5 to 6 stator passages are considered. An example of the difference in complexity between transient and steady-state results due to rotor-stator interaction by means of a contour plot of isentropic efficiency can be seen in Figure 4.13. The complete figure is given in Appendix B.3.

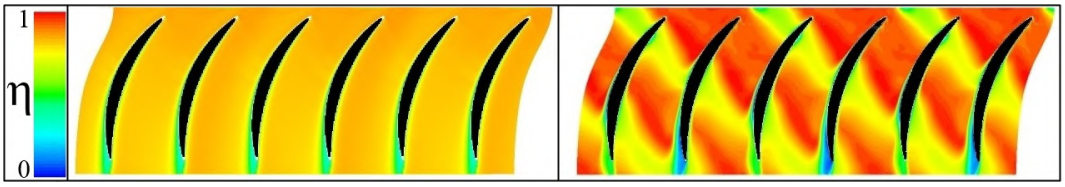

Figure 4.13: Isentropic compression efficiency contour plot for the first stator at 50% span showing the difference in complexity between the transient (right) and steady-state solutions

In Section 4.1, it was seen that although the transient and steady-state performance results do not vary within the same limits, the difference is not significant for the Darmstadt test case. However, in a single-stage simulation there is only one mixing plane. The difference may be more significant in multi-stage compressors, which have two mixing planes per stage and keeping in mind that the error is bound to be cumulative. Losses from secondary flow across rotor-stator interfaces are not properly accounted for when using a mixing plane. Pullan (2004) found that 10% less losses were produced by a steady-state model when compared to a transient model of a turbine stage. Figure 4.14 shows an example of increased areas of high entropy at the stator of the third stage due to the rotor tip leakage flow. At both operating points, the peak static entropy is more than 15% higher for the transient

Stellenbosch University https://scholar.sun.ac.za

case. This is most likely due to the difference in the transfer of the tip leakage flow across the interface.

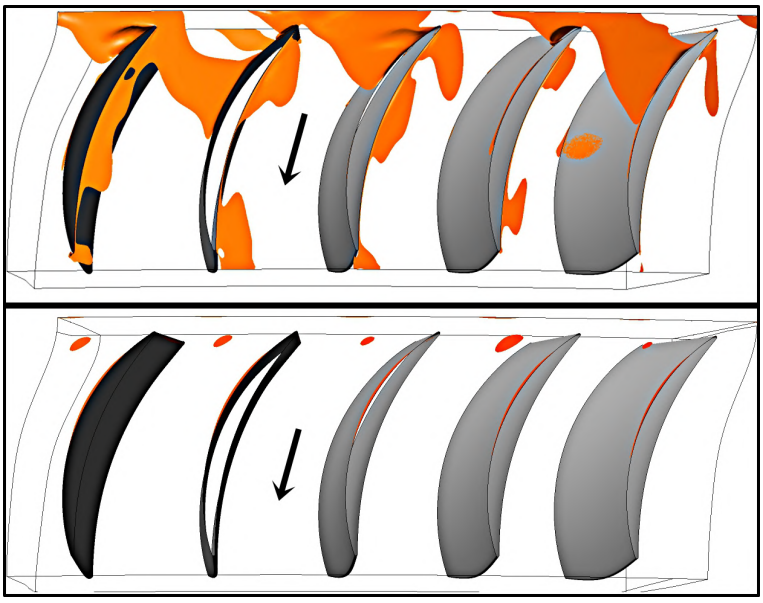

Figure 4.14: Areas of high entropy at the shroud of the third stator for the transient (top) and steady-state (bottom) solutions near choke.

At the design point, the isentropic efficiency drops by 1% for the proprietary multi-stage compressor. The pressure ratio drops by 0.9%. At a point near choke, the isentropic efficiency drops by 3.7%, and the pressure ratio drops by 2.3%. A meridional analysis with circular averaging can be used to show that the entropy production at the hub is more for the transient model. Increased entropy at the hub can be seen for the steady-state case in rotors 1 and 3 due to increased corner stall. Differences in flow separation are observed due to, for example, the way in which turbulent kinetic energy is transferred across the interface, which affects the boundary layer flow as observed during the Darmstadt comparison of transient and steady-state results (Section 4.1). The transient simulation shows thicker boundary layer flow due to the proper transfer thereof at the interface. The choking mass flow rate is 1.2% less for the transient model.

4.5 Effect of blade and endwall roughness

The roughness investigation was carried out at 93% and 100% speed on the baseline (no fillet) geometry, using the $k-\omega$ turbulence model. Roughness modelling with the $SST-\gamma Re_\theta$ model would require performing test cases for roughness validation. In the current work, the roughness height is defined by the sand grain roughness. Sand grain roughness (h_s) values of 1, 4 and 8 μm were tested on the blades and on the casing, resulting in 9 combinations, as per the graph legends.

Stellenbosch University https://scholar.sun.ac.za

Sand grain roughness between 1 and 8 μm in a compressor can account for surface roughness due to manufacturing and fouling (Chinnaswamy, 2015).

First, the results at 93% speed are discussed, since the 100% speed results lack mass flow stall margin, and one would therefore not be able to investigate much more than the effect on choking mass flow rate. For sand grain roughness of 4μm, the performance curves were evaluated towards numerical stall until the numerical model stalled to the nearest 500 Pa of varied static pressure outlet. This is also the case for the smooth surface (B0W0) model. Figure 4.15 shows the total pressure ratio as affected by blade and wall roughness of $h_s = 4\mu$m. B4 refers to blade roughness of $h_s = 4\mu$m and W0 to wall roughness of $h_s = 0\mu$m (smooth surface), and so forth. Results at 100% speed can be found in Appendix B.4.

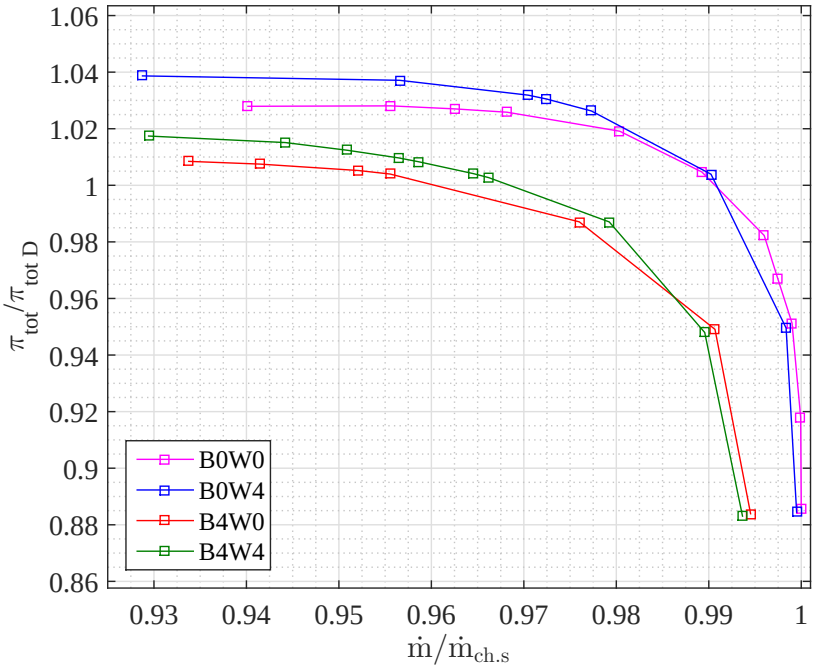

Figure 4.15: Roughness study pressure ratio @ 93% design speed for a sand grain roughness $h_s = 4\mu$m

As expected, the choking mass flow rate decreases as the total roughened surface area through the compressor increases due to increased blockage. However, note the crossover near 99% of the smooth surface choking mass flow rate (B0W0 vs B0W4 and B4W0 vs B4W4) when the blade roughness is kept constant and the wall roughness increased. A higher pressure ratio is observed when wall roughness is added, regardless of whether the blades are roughened. It may be explained using passage plots on a plane perpendicular to the flow. Figure 4.16 shows the turbulent kinetic energy at the hub and a portion of the blade.

Stellenbosch University https://scholar.sun.ac.za

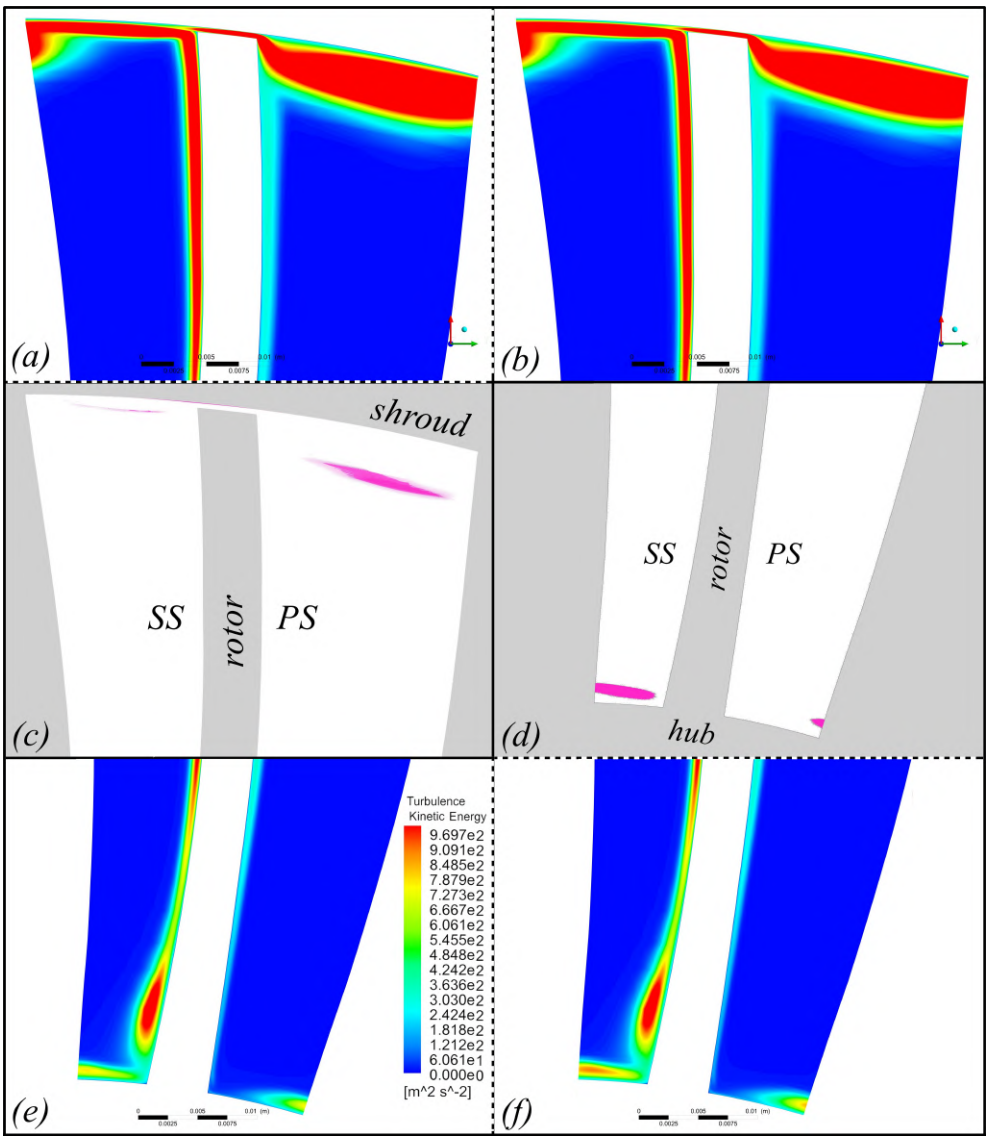

Figure 4.16: Turbulence kinetic energy contour maps and affected area (magenta difference threshold) map on a plane in the rotor passage perpendicular to the inflow direction. *(a):* B0W4 at shroud. *(b):* B0W0 at shroud. *(c):* Shroud area of significant difference. *(d):* Hub area of significant difference. *(e):* B0W0 at hub. *(f):* B0W4 at hub.

From Figure 4.16 (d) to (f), it can be seen that the turbulent boundary layer at the hub is larger for the B0W4 case, while the rotor turbulent boundary layer is unchanged. From (a) to (c) it should be noted that the area of high turbulent kinetic energy on this image is larger for the B0W0 case, in contrast to what is seen at the hub. This is because of a smaller tip leakage flow for the B0W4 case, caused by blockage of the tip vortex gap by means of a thicker casing boundary layer. Due to the angle at which the tip vortex intersects the plane, the tip vortex should

Stellenbosch University https://scholar.sun.ac.za

be interpreted as depicted in Figure 4.17. It does not form part of the turbulence kinetic energy migrating towards the shroud from the suction side surface (green dotted line). As expected, the rotor boundary layer size is unaffected. If the hub and shroud boundary layer size confines the flow path, and with less tip gap losses and at the same rotational speed (not the same shaft power), the pressure ratio increases as per Figure 4.15.

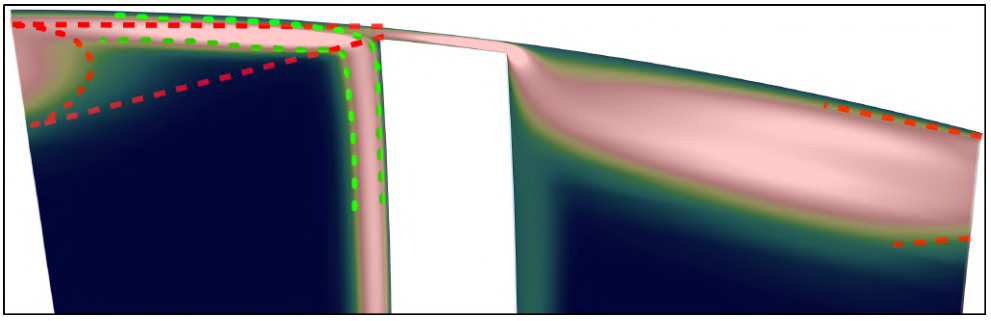

Figure 4.17: Interpretation of tip vortex (red dotted line) and suction side turbulent boundary layer (green dotted line).

Using contour plots of velocity magnitude in the stationary reference frame, it was confirmed that the casing boundary layer in the tip gap is indeed thicker for the rough wall case. This is not surprising (and therefore not shown) since roughness modelling is based on Nikuradse's shifting of the logarithmic law of the wall.

Considering Figure 4.15 near choke, it can be seen that the addition of blade roughness has a significant effect on the choking mass flow rate when compared to the addition of endwall roughness. This is expected because the blade constitutes the majority of the passage outline when observing a blade passage from the direction perpendicular to the flow and would naturally cause more blockage (Figure 4.18). However, blockage at the shroud is also affected by the blade suction side turbulent boundary layer migrating towards the casing and mixing with the tip clearance flow (Figure 4.17 and 4.18). The reduced tip clearance vortex size in the case of a roughened shroud compensates for some of the blockage caused in that case. It should also be noted that, in the case of a roughened blade, the tip clearance blockage is also increased due to roughness on top of the blade. However, the tip clearance vortex joins directly with the thickened migrating suction side boundary layer. This worsens the situation because the low-momentum flow accompanying the tip clearance vortex is now more rather than less. This explains the significant difference between the effect of endwall and blade roughening on the choking mass flow rate.

Stellenbosch University https://scholar.sun.ac.za

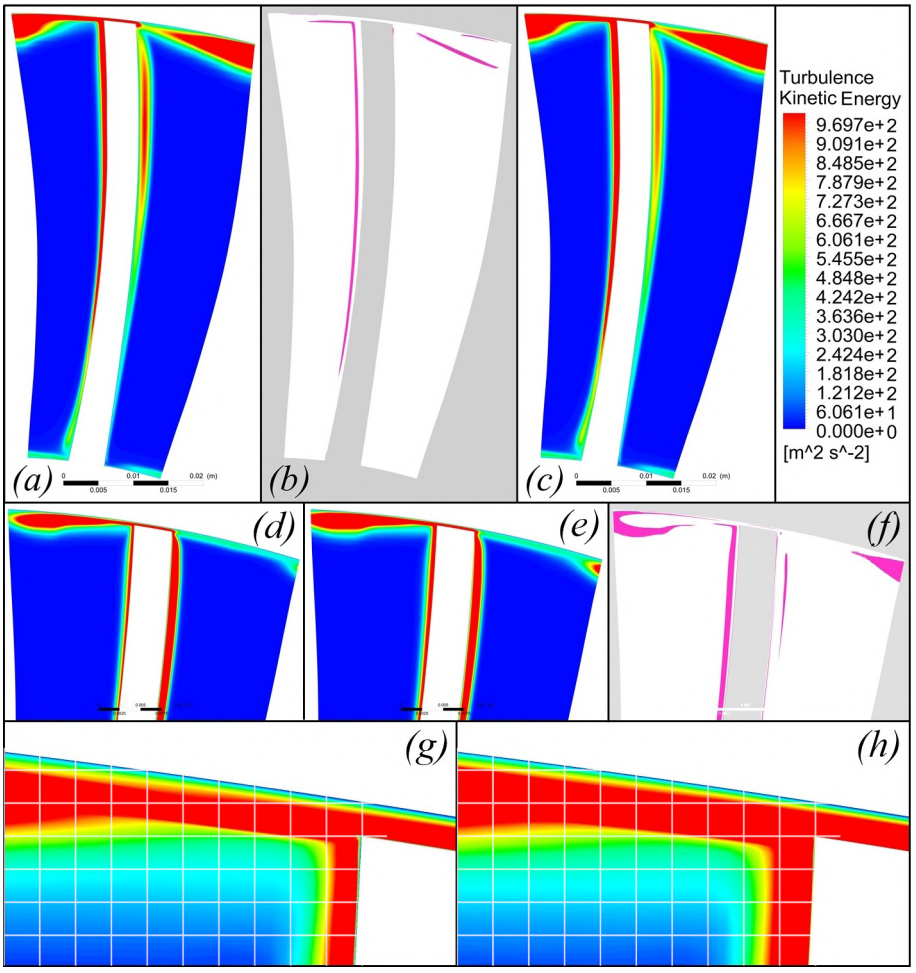

Figure 4.18: Comparison at choking mass flow rate. *(a):* B0W0 on a plane just downstream of the suction side passage shock emanation. *(b):* Threshold difference map between *(a)* and *(c)*. *(c):* B4W0 equivalent of *(a)*. *(d):* B0W0 upstream of suction side passage shock emanation. *(e):* B4W0 equivalent of *(d)*. *(f):* Threshold difference map between *(e)* and *(d)*. *(g):* detail at *(d)*. *(h):* detail at *(e)*.

At 100% speed, the effect of roughness on the choking mass flow rate is less than at 93% speed. The decrease in peak efficiency for the extreme case (B8W8) is less than 1% at design speed, and just under 1.5% at 93% design speed. The pressure ratio decreases by over 3% for the extreme case at 93% speed. It can be concluded that the compressor is much more sensitive to blade roughness than end-wall roughness, and it is most likely most sensitive to blade suction side roughness due to the observed significantly thickened suction side boundary layer. Figure 4.19 shows the pressure ratio and efficiency for all cases at 93% speed.

Stellenbosch University https://scholar.sun.ac.za

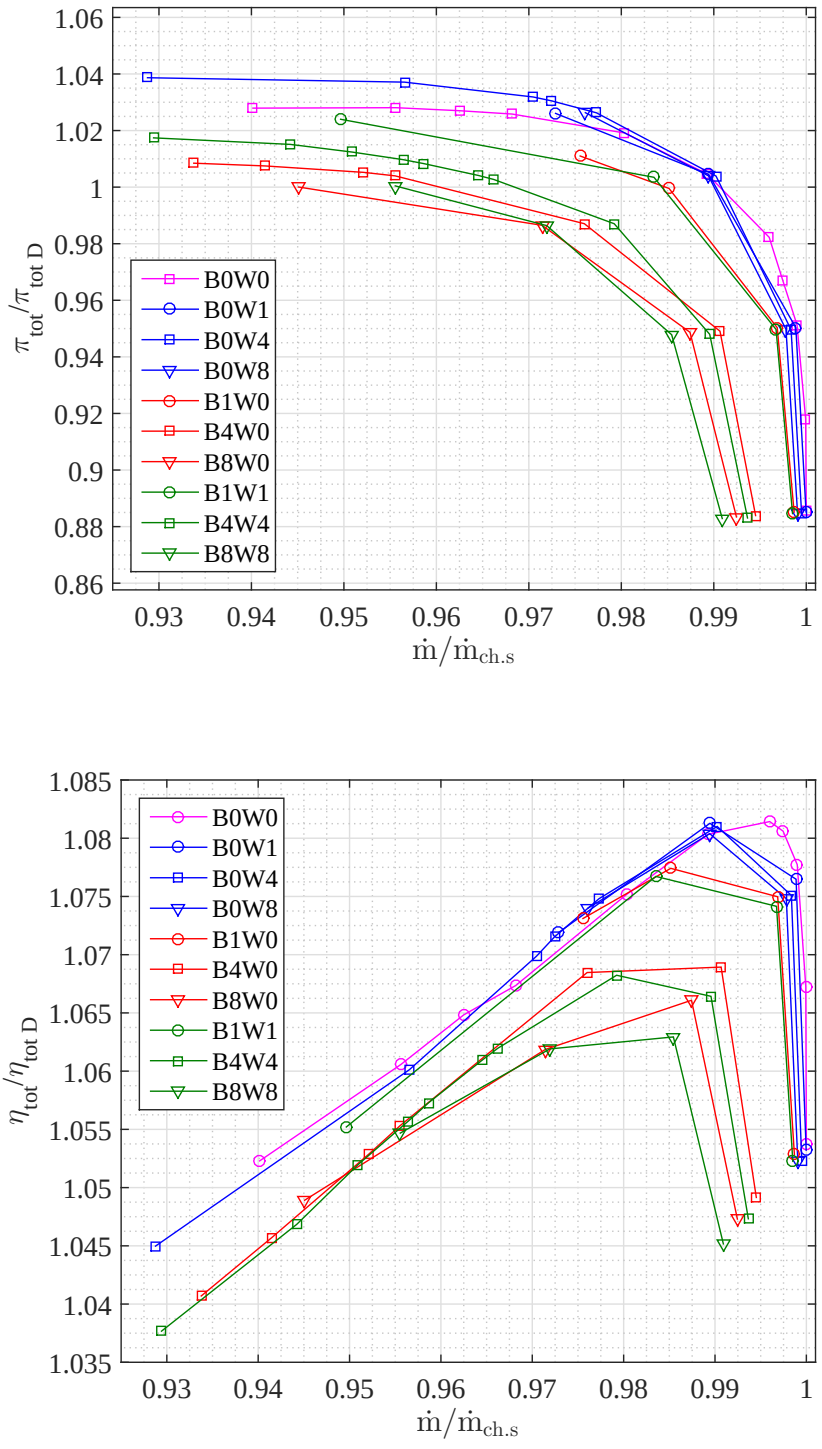

Figure 4.19: Roughness study: total pressure ratio (top) and total to total isentropic efficiency (bottom) at 93% design speed.

Stellenbosch University https://scholar.sun.ac.za

4.6 Effect of blade fillets

Using a mesh of the same size as the baseline investigation, an investigation on the effect of blade fillets is carried out using the $k-\omega$ turbulence model. Figure 4.20 shows the results. The mass flow rates are non-dimensionalised according to the baseline choking mass flow rate for each shaft speed.

Surprisingly, the mass flow rate increases if fillets are applied at 100% and 93% speed at choke. The original mesh convergence was re-evaluated and confirmed by running one operating point with a courser and finer mesh. It was also confirmed that the same conclusions are applicable with the $SST-\gamma Re_\theta$ by running one point on each speedline and comparing the result to the baseline $SST-\gamma Re_\theta$ results. The reason for increased choking mass flow rate is that the blockage through the compressor is highly dependent on hub corner stall around the design point. The added material blockage (by means of fillets) is more than compensated for by a significant reduction in flow separation. Figure 4.21 shows an example of this. Another example can be found in Appendix B.5. At 70% speed however, flow separation in the baseline compressor flow field is much less (Figure 4.22) and the fillets only add to the blockage, reducing the choking mass flow rate. At 70% shaft speed, the pressure ratio and insentropic efficiency clearly decrease when fillets are added. This is most likely due to reduced flow turning at the hub and enhanced secondary flow losses as stated by Shi *et al.* (2010). Shi *et al.* points out that the added fillet thickness at the point of maximum blade thickness pushes the flow near the hub radially outwards. This secondary flow mixes with the free stream, which increases losses. In the case of non-axisymmetric edges of blade rows due to even over-sized fillets, the pressure ratio and mass flow rate would most likely fluctuate due to time-dependent material blockage. The compressor could also experience an increase in time-dependent secondary flow losses and vibration.

At 93% shaft speed and away from choke, the compressor blockage becomes less dependent on corner stall since the corner stall decreases away from choke, and the mass flow rate subsequently decreases with the addition of fillets. The pressure ratio is less affected at 93% speed. This is due to corner stall compensation, since both corner stall and fillets reduce the flow turning and therefore blade loading (corner stall is replaced by material blockage by means of fillets). This explains why the drop in pressure ratio is more significant at 70% speed, where there is little corner stall to begin with.

Interestingly, the isentropic efficiency is increased rather than reduced in the case of fillets for 93% speed. However, the required shaft power at the same pressure ratio is 1.6% more for the filleted model. This is because the effect of stagnation, which is a loss in terms of fluid flow, is replaced by material blockage. Once again, this is not the case for 70% speed where there is little flow separation to begin with.

Stellenbosch University https://scholar.sun.ac.za

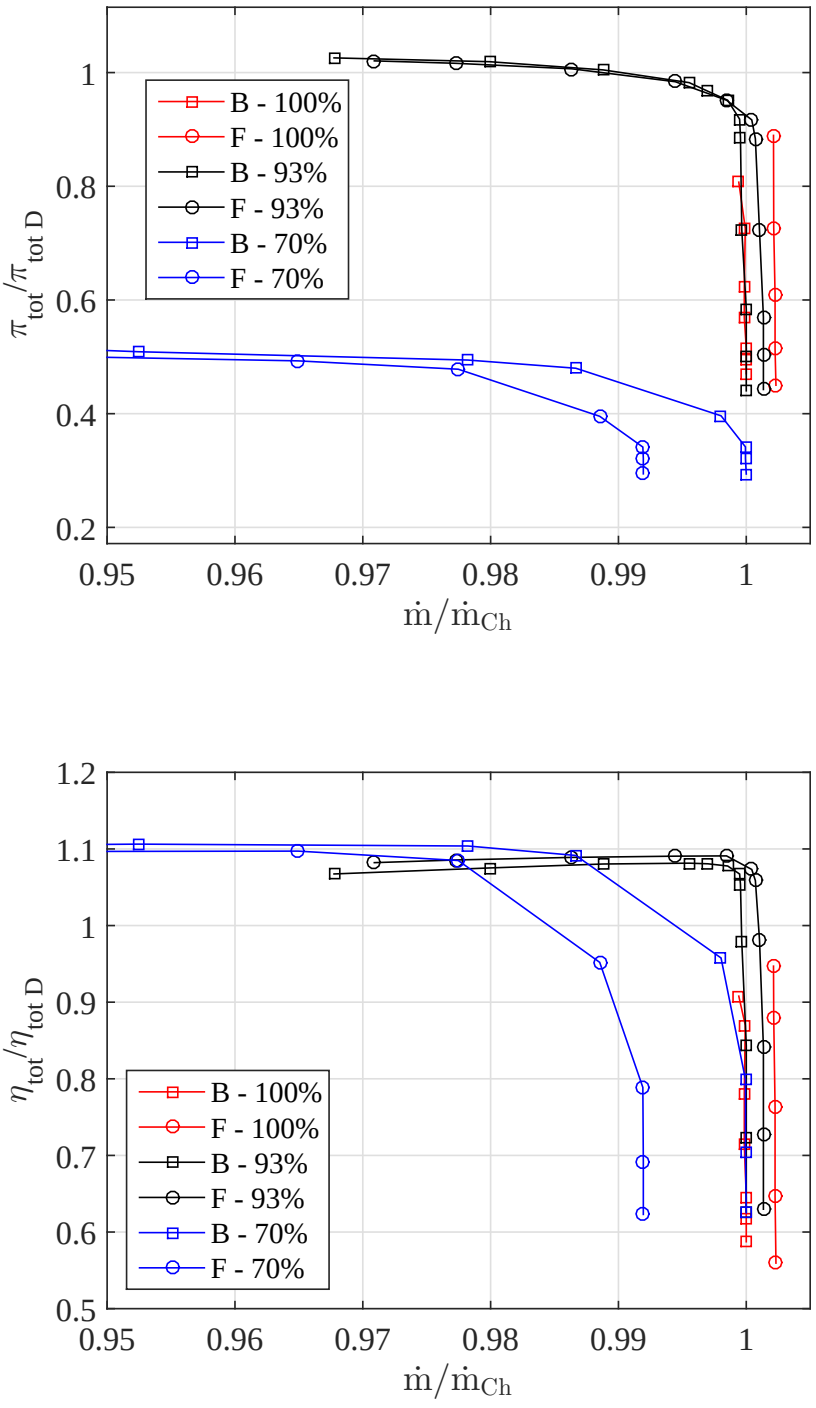

Figure 4.20: Effect of fillets on total pressure ratio (top) and total to total isentropic efficiency (bottom) at case-specific non-dimensionalised mass flow rate. B = Baseline geometry, F = Filleted geometry.

Stellenbosch University https://scholar.sun.ac.za

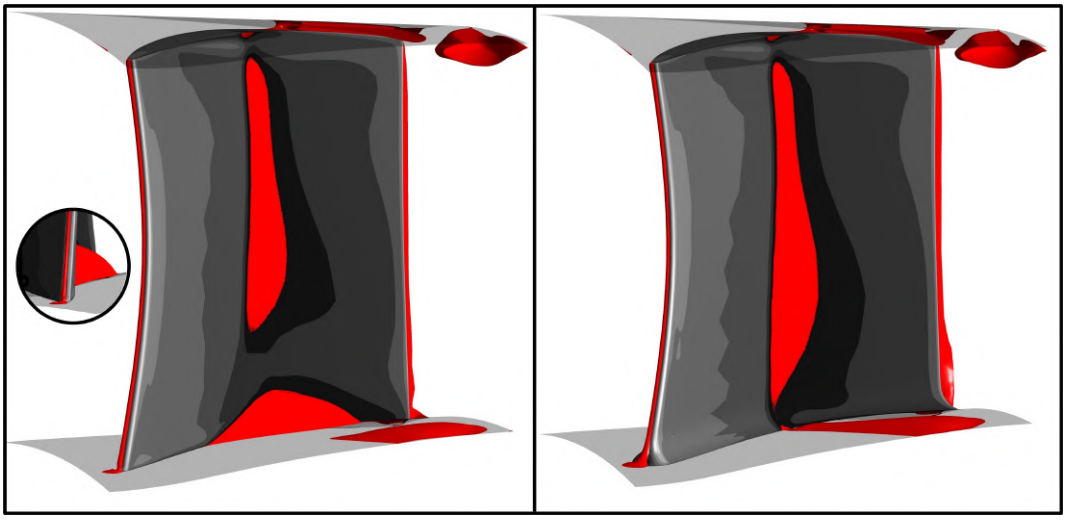

Figure 4.21: Rotor 4 at 100% design speed for the raw (left) and filleted (right) cases at choke. The red ISO surface (u @ 0 m/s) indicates negative axial velocity

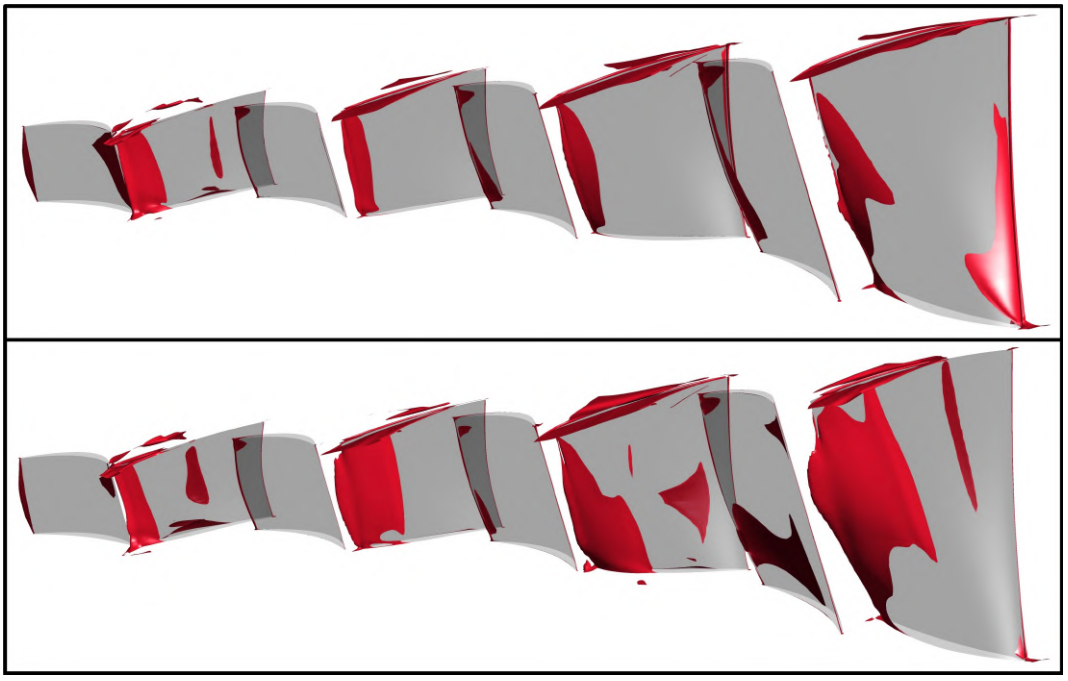

Figure 4.22: Negative axial velocity at 70% design speed (top) for comparison with 100% design speed (bottom) at choke.

Stellenbosch University https://scholar.sun.ac.za

Chapter 5

MULTALL

MULTALL-open is a rapid turbomachinery design suite of programs. Three programs can be found within MULTALL-open. MEANGEN can be used in a rapid initial design process. MEANGEN generates an input file for STAGEN. The STAGEN input file provides the essential compressor geometry and mesh definition, as well as boundary conditions and initial solution guesses. An input file to MULTALL can be generated in a matter of minutes. A 3D simulation can then be performed in MULTALL. According to Denton (2017), a typical MULTALL simulation converges in the order of 15 minutes per stage (computing speed is not mentioned). In the current work MULTALL-open is used for turbomachinery analysis rather than for its intended purpose, which is turbomachinery design.

5.1 MULTALL as an analysis tool

For the purpose of analysing an existing compressor, STAGEN can be used as a starting point. Once the STAGEN input file is completed, the blade profiles may be plotted. If the user is satisfied with the profile plots, STAGEN generates an input for MULTALL. In STAGEN, all blade rows must be defined in an equal number of span-wise sections (this may be an inconvenience). The STAGEN input file may be used to add lean and sweep to the blades, as well as axial positioning of the blades without manually modifying the coordinates. This is convenient for a rapid comparison of different designs within these design parameters. The geometry can also be scaled in specific ways within STAGEN. However, it will be seen that, in some cases, STAGEN warps the geometry and that it is better to perform these alterations with an external program, written for example, in MATLAB®. STAGEN does not provide a means for a complete definition of the geometry, such as defining axial variation in tip clearance gap or defining blade fillets. However, these aspects of the geometry can be defined by modifying the MULTALL input file coordinates. Fillet geometry can only be introduced by adding more profile sections at the fillet as a means of defining it. Since STAGEN is a design program, it decides about certain aspects of the geometry or computational domain by itself. This may lead

Stellenbosch University https://scholar.sun.ac.za

to inaccuracies when using STAGEN to input existing geometry.

5.2 MULTALL geometry defintion

The way in which existing geometry was recreated in MULTALL format for the test cases and for the multi-stage compressor is discussed. In the current work, the MULTALL geometry is defined using the input file to STAGEN, as well as modification of the subsequently generated MULTALL input file. When defining the geometry, the user may consult "Instructions for Program STAGEN" by Denton (2017). The available methods in STAGEN that are most convenient when considering the geometry format were attempted. During the test case geometry input, the process was found to be tedious due to unexpected warping of the geometry by STAGEN. However, during the multi-stage geometry input, a promising solution to this problem was found.

5.2.1 Test case geometry

Using MATLAB®, coordinates were reproduced or interpolated as needed before being written into the appropriate format in order to compile the STAGEN input file. Such an input file formatted for a coordinate-based input method and defining the geometry for one stage, typically consists of roughly 2000 rows with multiple entries per row.

The blade geometry was oriented according to the convention commonly used in MULTALL using the appropriate rotation settings in the STAGEN input file. The results from the initial simulation, which used a coordinate-based blade definition, greatly differed from what was expected. Upon inspection of the results and of the programs, it was found that STAGEN displays the correct blade profiles for perusal by the user, but distorted the output geometry when it produced the MULTALL input file.

According to Denton (2017), the standard means of defining blade geometry in MULTALL is by a blade angle distribution as a function of blade chord, with a mathematically defined thickness distribution. In this method, the user inputs certain constants, which STAGEN uses to calculate the thickness distribution. Due to the peculiar results when using the coordinate method, this blade-angle and thickness-distribution-method was attempted next. MATLAB® was used to calculate these parameters from the blade coordinates. STAGEN could be used to plot thickness distribution graphs of the original blade coordinates. The thickness distribution of the new blade data was then iteratively matched to that of the original blading by means of the mathematical thickness distribution. The parameters for defining a thickness distribution in STAGEN do not provide complete freedom, however, the difference between the new and original blading is, in most cases, small. To illustrate what is meant by this, a comparison between the original and mathematically-defined thickness distribution is shown in Appendix C.1.

Stellenbosch University https://scholar.sun.ac.za

A compromise must be made between the accuracy of the leading or trailing edge thickness and the accuracy of the geometry around the point of maximum thickness. Emphasis was placed on the accuracy of the thickness distribution around the point of maximum thickness. In either case, the shock structure will be affected. Aside from the obvious difference in choking mass flow if the maximum thickness is not accurate, it is assumed that the shock structure may be more significantly affected with regards to shock position if the geometry around the point of maximum thickness, where the thickness distribution does not change as abruptly as a function of chord position, is not as accurate as possible.

Unless a program that interpolates and converts coordinates directly into a desired mesh in the format required by MULTALL is written, it is likely that the geometry produced by STAGEN will always contain discrepancies.

In some cases, the pitch-wise dimension of the blade profiles is extended by STAGEN, which also results in incorrect blade angles. There is no direct constraint-control over this dimension. Before generating a MULTALL input file, STAGEN fits the approved blade profiles between leading and trailing edge coordinates which can be defined in the radial and axial coordinates. It is apparent that the pitch-wise dimension can be calculated through the blade angle and these coordinates, yet the geometry is often warped such that these geometric relations no longer hold true. The geometry cannot be viewed in MULTALL nor STAGEN.

Even if the geometry is not warped, the geometry for a compressor may be defined with blade profiles which are not aligned with streamlines and at the hub and shroud surface, as is required by STAGEN. It is often the case that a profile is defined as extending from inside the hub or outside the shroud. In such cases, writing the STAGEN input file requires prior interpolation of blade coordinates, perhaps along a section that is irregularly shaped at the hub or shroud. Creating a STAGEN input file that exactly satisfies the geometry format requirements is, in most cases for existing geometry based on coordinate measurement, not practical because it is too time-consuming. It therefore becomes clear that, regardless of the discrepancies and regardless of the reason for often warped geometry, and keeping in mind the inability to view the geometry within the MULTALL open-source suite of programs, a program should be written with which the geometry can be viewed in the MULTALL format and validated against the original format.

A MATLAB® program which finds and plots the appropriate coordinate data within the MULTALL input file was written. It can also be used to plot the original profile data. With the discrepancies in mind, the program was written such that blade profiles can be (non-uniformly) scaled and translated to alleviate discrepancies in blade angles. Due to possible discrepancies in thickness and blade turning as a result of off-set blade profile sections (such as a profile section defined from within the hub), the profile thickness can be changed. The camber of a profile can be changed by multiplying a fraction of a non-dimensionalised thickness distribution with the blade coordinates. This may have an unwanted thinning-effect on the leading and trailing edge thickness, therefore a decaying function is used to add thickness to the leading and/or trailing edge if needed. A typical example of the

Stellenbosch University https://scholar.sun.ac.za

graphical output by the program can be seen in Figure 5.1. Using a top view, the MULTALL blade profiles are adjusted to fit the measured geometry.

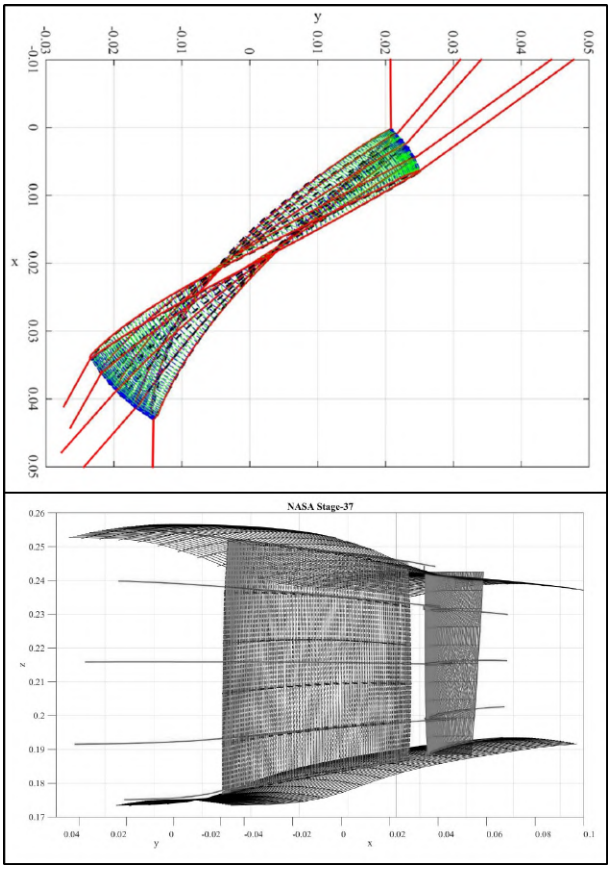

Figure 5.1: The MATLAB® program output of the comparison of stacked blade layers (top) and an overview of the compressor stage (bottom).

5.3 Multi-stage compressor geometry

Although it is clear that MULTALL, in its current version, is far from ideal for existing geometry, importing the geometry of the multi-stage compressor was much less effort per compressor stage than the CFD test cases. This is because of a different geometry definition option in STAGEN and because of the way in which particulars of the multi-stage compressor, which was created by ANSYS® CFX®'s native turbomachinery tools, could be exported. STAGEN offers an option to define blade layers by means of angles and tangential thickness distribution as a function of blade chord. This option is attractive because the axial thickness distribution and the leading, trailing, and mid-chord blade angles could be exported from ANSYS® CFX®. It was only needed to convert the axial thickness distribution to tangential thickness distribution. In order to do this, vectors of blade angles corresponding to the irregularly-spaced axial thickness distribution-vectors were interpolated. The

Stellenbosch University https://scholar.sun.ac.za

tangential thickness distribution as a function of blade chord could then determined. In this format, it is far less time-consuming than iteratively matching the mathematical thickness distribution, as done for the test case geometry definition. Furthermore, a significant advantage is that STAGEN did not warp the geometry such that blade angles or blade thickness was changed. Although the dimensions of the profiles were accurate, STAGEN straightened the forward-lean of the rotor blades and moved some profiles such that the spacing between profiles at the mixing-plane becomes larger. Therefore, using this method of geometry definition, only the position of blade profile layers relative to each other is changed. This was corrected by using the MATLAB® program. Although a larger spacing at the mixing plane can assist with convergence, the manner in which the position of the stacked profiles was changed relative to each other was not accurate. Therefore the profiles were moved to their original position.

5.4 MULTALL Modelling setup

MULTALL uses H-grid topology. A typical example of a typical MULTALL grid can be seen in Figures 5.2 and 5.3.

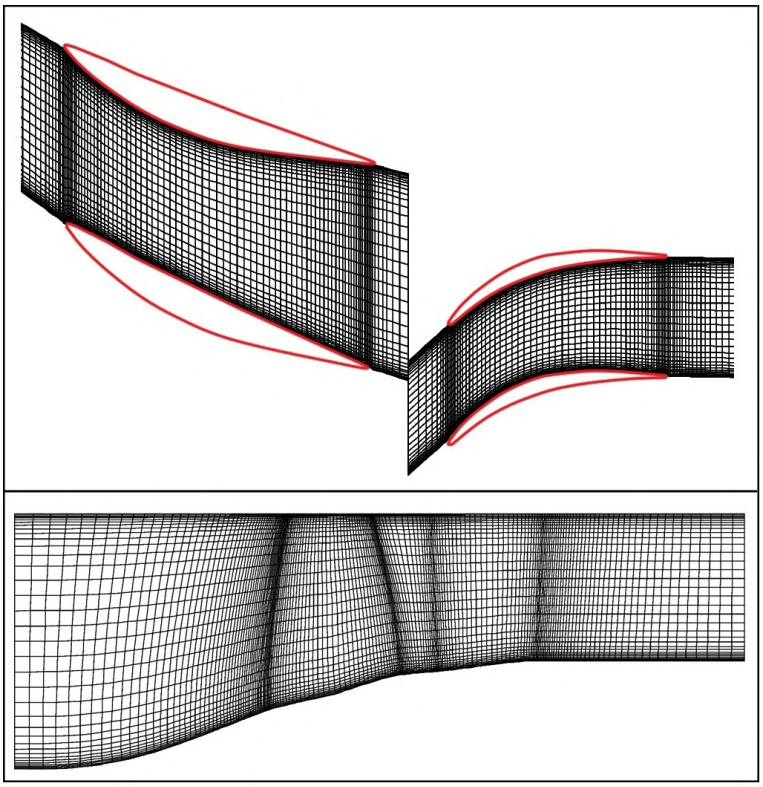

Figure 5.2: Typical MULTALL grid shown through a stream-surface (top) and meridional-surface (bottom).

Stellenbosch University https://scholar.sun.ac.za

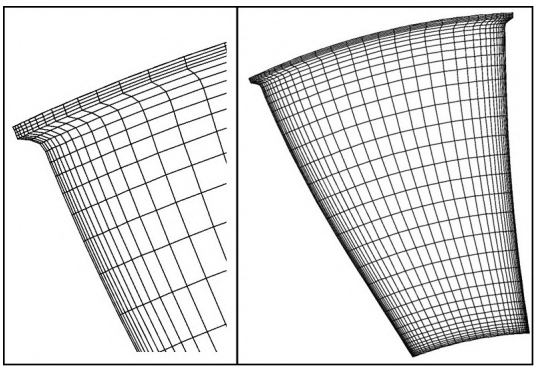

Figure 5.3: Typical MULTALL grid shown through a quasi-orthogonal-surface at a blade. Detail at the tip gap is shown (left).

The particulars of the grids under consideration for MULTALL are shown in Table 5.1. For the fine grid, the limits on pitch- and spanwise grid dimensions imposed by MULTALL version 18.3 are exceeded by recompiling MULTALL with increased limits (edited in *commall-open-18.3*). This was done in order to determine whether MULTALL can be used when grid resolution exceeds the limits set by Denton. In this work, typical grid dimensions between blade rows are 20 to 30 cells. The grid dimensions at the inlet and outlet may vary from 20 to 100 cells. For all grids, the ratio between the first cell height and the largest cell in the pitch and spanwise directions is 1:20. It is often essential to coarsen the grid at the inlet, otherwise the continuity equation converges poorly and the mass flow rate cannot be determined accurately.

Table 5.1: Considered grid dimensions for MULTALL

	coarse	medium	fine	extra fine
pitch-wise	37	37	64	83
span-wise	37	37	64	83
rotor (axial)	40	70	70	100
stator (axial)	30	50	50	70
tip gap (radial)	4	4	7	10
total elements (Darmstadt)	205350	273800	786432	1322688
total elements (Stage-37)	219040	287490	860160	1446690

A typical value of 0.0050 for a "convergence limit" suggested by Denton is defined as the average percentage change in velocity per time step divided by the RMS velocity of all grid points (E_{avg}). In some cases, even with this "convergence limit" reached, the continuity equation has not converged enough to be able to determine the mass flow rate through the compressor accurately, with the mass flow rate average at axial grid locations differing significantly through the compressor. Convergence of a solution is a matter of opinion, and depends on the use of the

Stellenbosch University https://scholar.sun.ac.za

model. For the multi-stage simulation, for which coarse span- and pitch-wise grid dimensions is used, it is difficult to obtain convergence of E_{avg} lower than 0.01. The solution was therefore taken as converged around $E_{avg} = 0.015$, given that the continuity equation is converged such that the mass flow rate average at axial grid points does not differ by more than 2% through the compressor. The boundary conditions selected for MULTALL simulations can be seen in Table 5.2. Solver parameters which were found to be notably important in order to achieve convergence are discussed in Appendix C.2.

Table 5.2: Boundary conditions used for MULTALL simulations.

Location	**Boundary condition**	**Comments**
Inlet	IN_PRESS = 0	The inlet pressure is calculated from the continuity equation. This is preferred for axial flow machines (Denton, 2017).
	IN_VTAN = 1	Unique incidence condition on tangential velocity. Since the relative inlet flow is supersonic, the unique incidence is appled by setting IN_VTAN = 1. It is assumed that the inlet is far enough from the rotor such that the tangential velocity may be approximated as 0 m/s.
	IN_VR = 0	The radial velocity is obtained by extrapolation from the interior flow field.
Outlet	IPOUT = 0	The static pressure at the hub is fixed and radial equilibrium is used for spanwise pressure variation.

In MULTALL, four different viscous models may be selected:

- Inviscid
- Thin shear layer mixing length
- Full Navier-Stokes mixing length
- Spalart-Allmaras

Denton (2017) suggests the use of the "new mixing length model" (Full Navier-Stokes mixing length). However, the formulation of the mixing length model is controversial in turbomachinery CFD. It was found that in most cases, the new mixing length model predicts a higher pressure ratio over some parts of the operating curve

Stellenbosch University https://scholar.sun.ac.za

or over the entire operating curve. It was also found that the new mixing length model generally predicts higher efficiency. Furthermore, it is apparent that there is no advantage in choosing the new mixing length model over Spalart-Allmaras with regards to convergence of the solution. The one-equation Spalart-Allmaras turbulence model's proven ability to model complex aerodynamic flows at lower computational cost than algebraic models had lead to wide acceptance and popularity in turbomachinery CFD (Reising, 2009). The Spalart-Allmaras turbulence model was selected for the multi-stage MULTALL simulation. A comparison between the two turbulence models for the "medium" grid is shown in Figures 5.4 and 5.5.

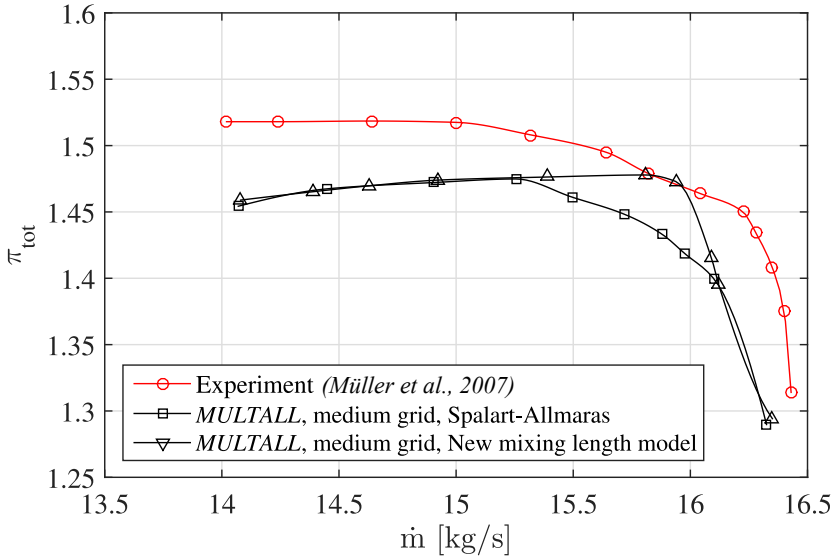

Figure 5.4: MULTALL total pressure ratio comparison of Spalart-Allmaras and "New mixing length model" with experimental results for the Darmstadt test case.

Stellenbosch University https://scholar.sun.ac.za

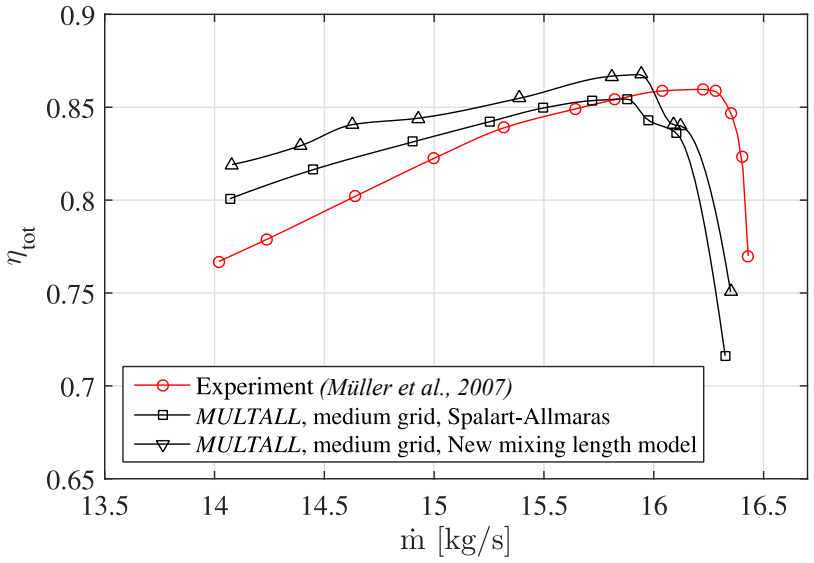

Figure 5.5: MULTALL total to total isentropic efficiency comparison of Spalart-Allmaras and "New mixing length model" with experimental results for the Darmstadt test case.

The test case results are shown in Figures 5.6 to 5.9. The Spalart-Allmaras turbulence model was used. For the Darmstadt test case in Figures 5.6 to 5.7, it can be seen that the pressure ratio and efficiency increase as the mesh is refined. It should be noted that MULTALL does not support the grid dimensions of the extra fine mesh. The limits have to be changed and the program recompiled. The extra fine mesh results are merely included as additional to the current work. The over-predicted pressure ratio by the extra fine mesh is analogous to the result obtained by the $SST - \gamma Re_\theta$ turbulence model without modified shear stress limiter during the ANSYS® CFD validation. For the NASA Stage-37 test case, the extra fine mesh once again produces a result analogous to the result obtained by the $SST - \gamma Re_\theta$ turbulence model during the ANSYS® validation, with the numerical pressure ratio falling short of experimental results in this case. Although it is most likely the result of error cancellation by the coarser meshes, the efficiency obtained by the extra fine mesh differs most from the experimental results.

Although the results produced by the extra fine grid differ significantly from the coarser grids, it is not the aim of the current work to achieve mesh independence in MULTALL. The dimensions of the coarser grids fall within the limits set by Denton. In his provided compressor examples, Denton uses similar grid dimensions as used for the "medium" mesh. MULTALL does not support parallel processing. It is therefore not practical to use grid dimensions as large as those of the "extra fine" grid. It was concluded that the choking mass flow rate and pressure ratio are best predicted by the extra fine grid. It was also concluded that the difference between the "medium" and "fine" mesh results was not significant. For the intended use of

Stellenbosch University https://scholar.sun.ac.za

MULTALL, which is to obtain a solution within a short period of time, the medium mesh produces sufficient results. At the operating point, the numerical ("medium" mesh) and experimental (Müller *et al.*, 2007) pressure ratio and efficiency for the Darmstadt test case differ by 2.9% and 1.7%, respectively. At the operating point, the numerical ("medium" mesh) and experimental (Bakhtiari *et al.*, 2015) pressure ratio and efficiency for the Darmstadt test case differ by 4.3% and 0.9%, respectively. At the operating point, the numerical ("medium mesh") and experimental pressure ratio and efficiency differ by 7.4% and 3%, respectively. Once convergence can be obtained, an entire performance curve for a single stage compressor can be solved within an hour with the "medium" mesh.

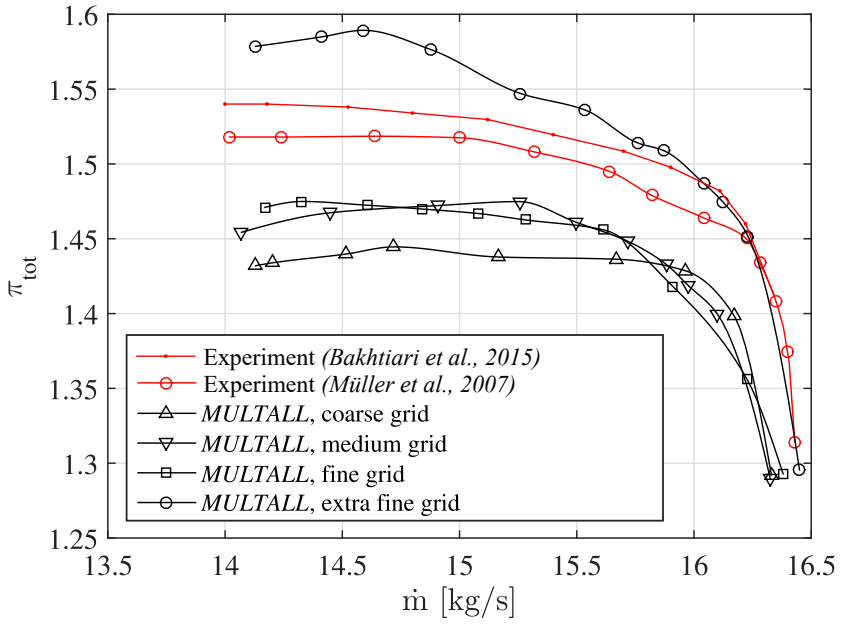

Figure 5.6: MULTALL total pressure ratio comparison with experimental results for the Darmstadt test case.

Stellenbosch University https://scholar.sun.ac.za

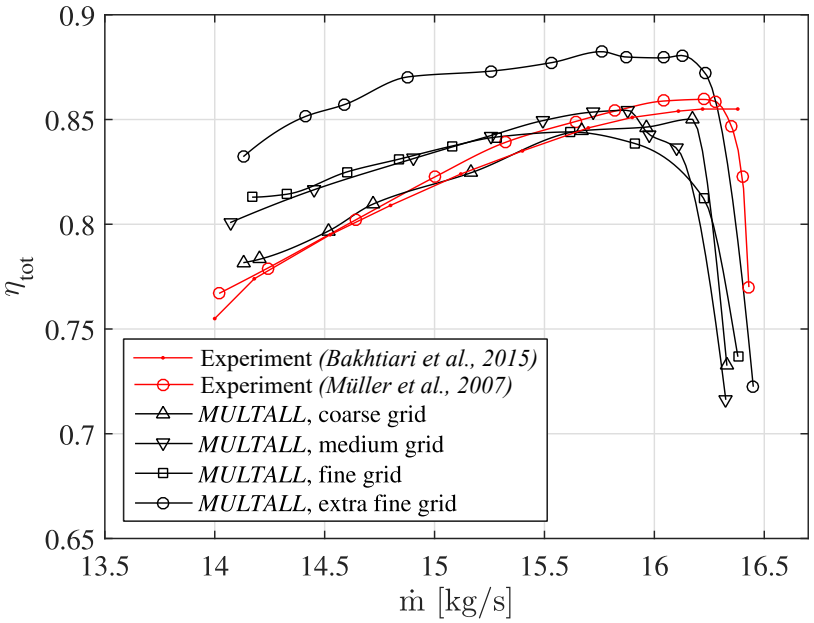

Figure 5.7: MULTALL total to total isentropic efficiency comparison with experimental results for the Darmstadt test case.

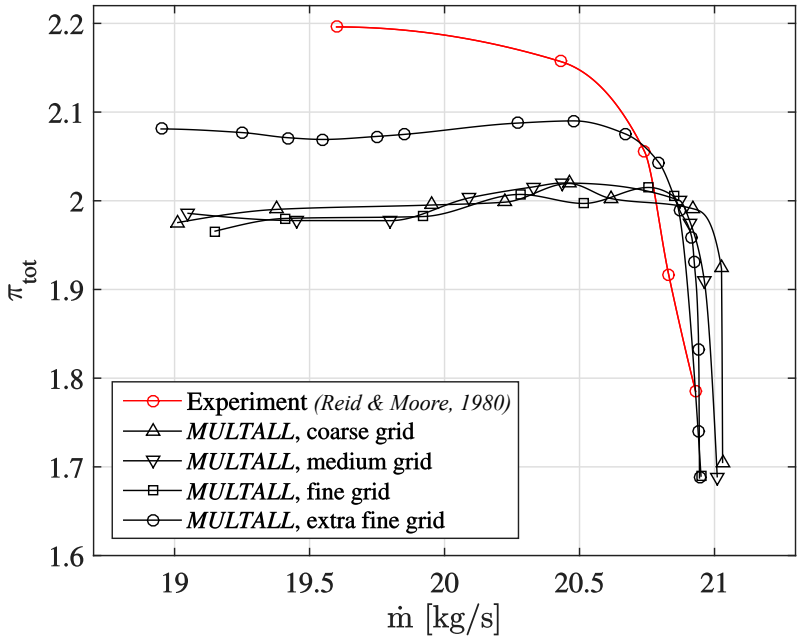

Figure 5.8: MULTALL total pressure ratio comparison with experimental results for the NASA test case.

Stellenbosch University https://scholar.sun.ac.za

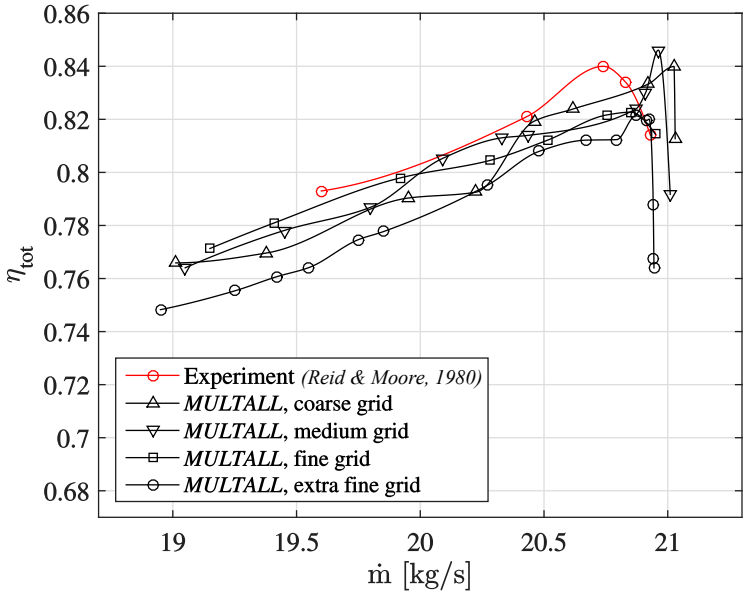

Figure 5.9: MULTALL total to total isentropic efficiency comparison with experimental results for the NASA test case.

5.5 Shroud pressure distribution

In order to investigate the level of detail with which a fine-grid MULTALL simulation can resolve typical features of a transonic axial compressor flow field, such as the passage shock and interaction of the rotor-bow shock with the tip vortex, a comparison of the pressure distribution at the shroud is performed for the Darmstadt test case. Since the shock interacts with the tip clearance flow at the shroud, this may be useful with regards to MULTALL's ability to resolve typical complexities of transonic axial compressor flow fields. The grid of this model uses the axial grid dimensions of the "extra fine" grid, and the pitch- and spanwise dimensions of the "fine" grid in Table 5.1.

The experimental and numerical (MULTALL) pressure distribution at the shroud is shown in Figures 5.10 and 5.11. When observing the pressure distribution at peak efficiency, the reason for a stronger passage shock and downstream positioned tip leakage vortex for the numerical solution is because the experimental result at "peak efficiency" was measured closer to 16.0 kg/s. For the numerical model, peak efficiency occurs at 16.2 kg/s. For the Darmstadt test case, experimental results such as those of Müller et al (2007) used in Figure 5.7, show that peak efficiency occurs between 16 and 16.2 kg/s. The exact mass flow rates at which the experimental static pressure distribution was measured is not clear. Keeping this in mind and observing the features of the flow field which evolve from choke to stall, the level of detail resolved by the MULTALL simulation and the similarity between the MULTALL and experimental static pressure distribution is promising. Furthermore, the numerical

Stellenbosch University https://scholar.sun.ac.za

flow field at 15.2 kg/s is remarkably similar to the intermediate experimental result towards stall.

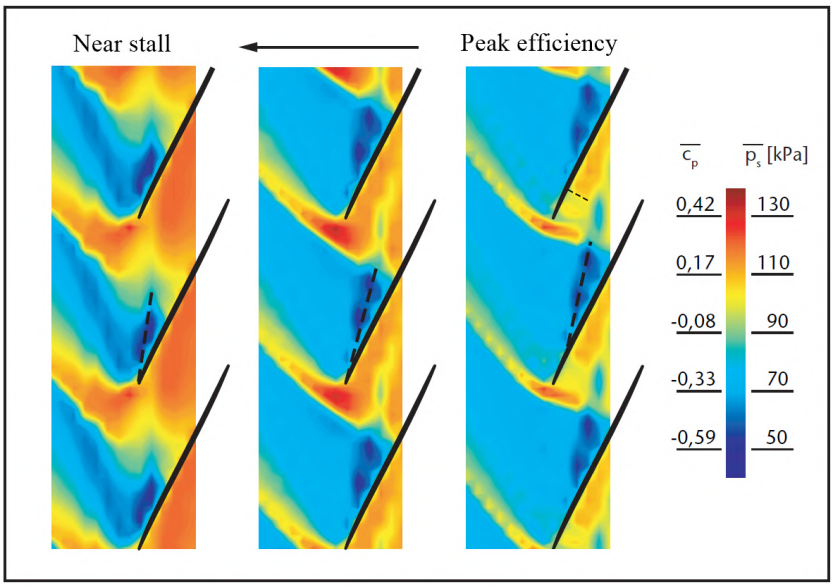

Figure 5.10: Experimental static pressure at the shroud of the Darmstadt rotor. Adapted from Bergner (2006).

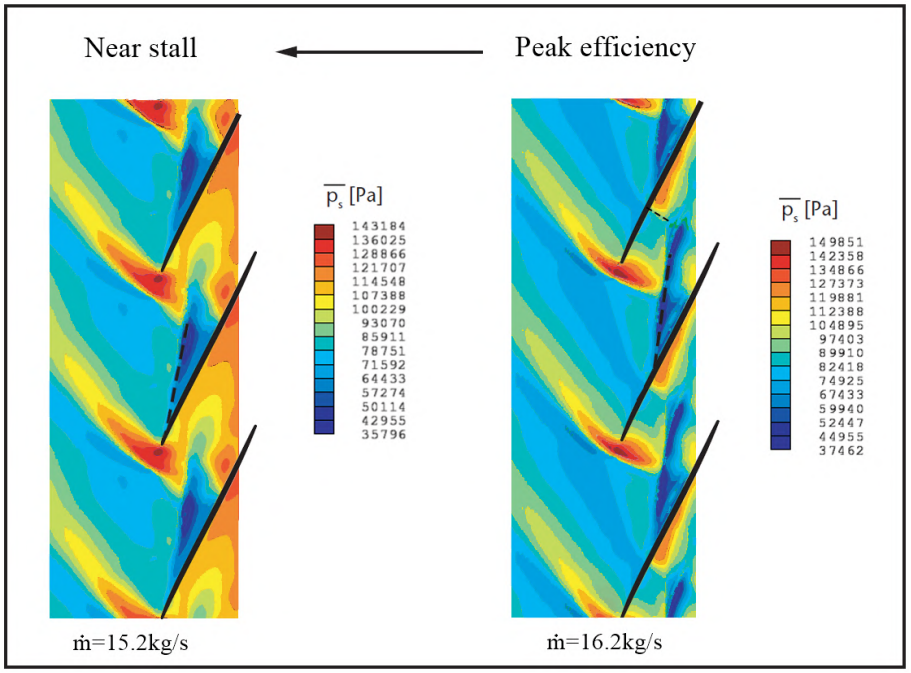

Figure 5.11: Numerical (MULTALL) static pressure at the shroud of the Darmstadt rotor at 16.2 kg/s (peak efficiency) and at 15.2 kg/s.

Stellenbosch University https://scholar.sun.ac.za

To support this, the corresponding ANSYS® results for the Darmstadt test case at 16.2, 16.0 and 15.2 kg/s are shown in Figure 5.12. The stronger passage shock and downstream positioned tip leakage flow of the ANSYS® solution at 16.2 kg/s is in close agreement to the MULTALL solution at this mass flow rate. The ANSYS® result at 16.0 kg/s supports the fact that the experimental "peak efficiency" was measured closer to 16.0 kg/s. Lastly, the intermediate experimental static pressure distribution is in agreement with the MULTALL and ANSYS® static pressure distribution at 15.2 kg/s.

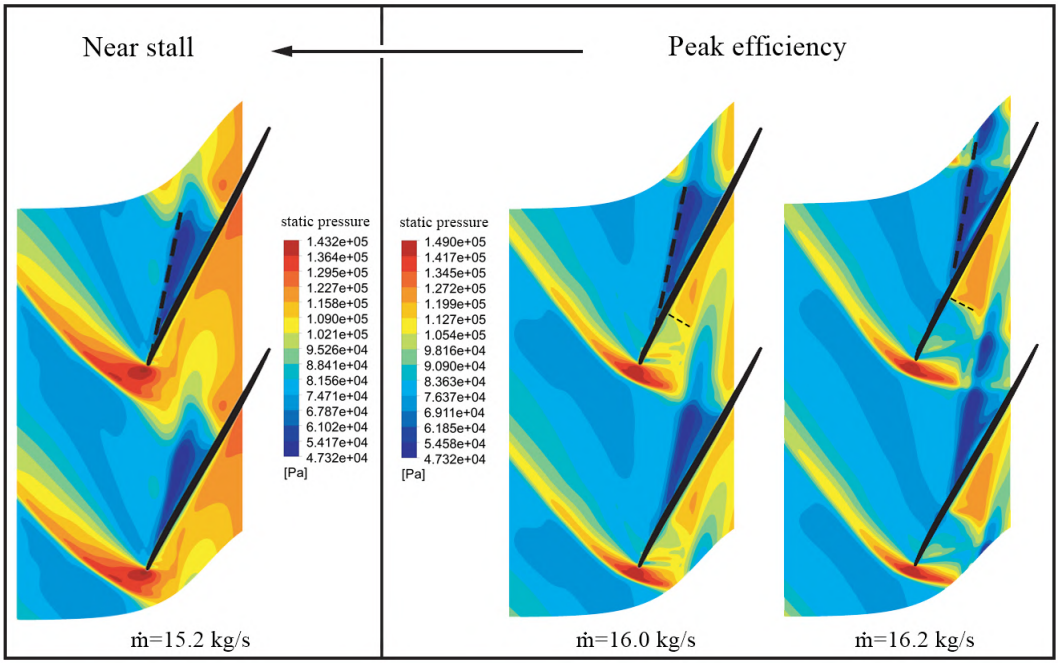

Figure 5.12: Numerical (ANSYS) static pressure at the shroud of the Darmstadt rotor at peak efficiency and near stall.

5.6 MULTALL multi-stage compressor

The "medium" grid dimensions were chosen for the multi-stage compressor, resulting in a grid with a total of 1 million cells. The Spalart-Allmaras turbulence model was used. It was challenging to create a mesh for which the solution converges for the multi-stage compressor. This was due to complex geometry such as forward lean of the rotor blades and close spacing at the hub. Furthermore, the continuity equation often diverged because of severe pressure gradient in the diffuser. In order to solve this, care had to be taken to start solving the model at a sufficiently high outlet pressure.

It was initially attempted to create a multi-stage model with the extra fine mesh. Attempts at obtaining convergence without modifying the geometry were unsuccessful. The main problem was divergence at the mixing plane. MULTALL pro-

Stellenbosch University https://scholar.sun.ac.za

vides various methods for possibly reducing instability at the mixing plane. None of the methods sufficiently reduced instability at the mixing plane for the extra fine mesh. It was also found that the relaxation factors on the multi-block grid layers had to be reduced significantly for the extra fine mesh. Furthermore, due to single-thread processing on such a fine mesh it took extremely long for the simulation to run before it could be concluded that the simulation would diverge (in some cases approximately 6 hours). It was concluded that the "extra fine" grid dimensions are not practical for a multi-stage compressor in MULTALL. Once pitch- and spanwise grid dimensions were reduced to dimensions used by Denton in his examples of multi-stage compressors, convergence in the order of $E_{avg} = 0.01$ could be attained with an unmodified geometry. In general, Denton suggests $E_{avg} = 0.005$. Convergence well below this level can be attained for a single stage compressor, but it is difficult in the case of a multi-stage compressor with diffuser. Over some regions of the operating curve, flow separation occurs in the diffuser. For an example of the grid used for the multi-stage compressor, selected regions of the grid is shown in Appendix C.3.

The MULTALL and ANSYS® $(k - \omega)$ results for the multi-stage compressor at 93% speed and 100% speed are compared in Figures 5.10 and 5.11. The mass flow rates are non-dimensionalised with respect to the choking mass flow rate of the results obtained by ANSYS® for the respective shaft speeds. The difference between MULTALL and ANSYS® results is summarized in Table 5.3.

Table 5.3: MULTALL and ANSYS® results comparison.

speed	$\triangle\pi_{max}$	$\triangle\eta_{max}$	$\triangle\dot{m}_{choke}$
100%	9.5%	7.7%	2.2%
93%	13.6%	9.9%	2.7%

Stellenbosch University https://scholar.sun.ac.za

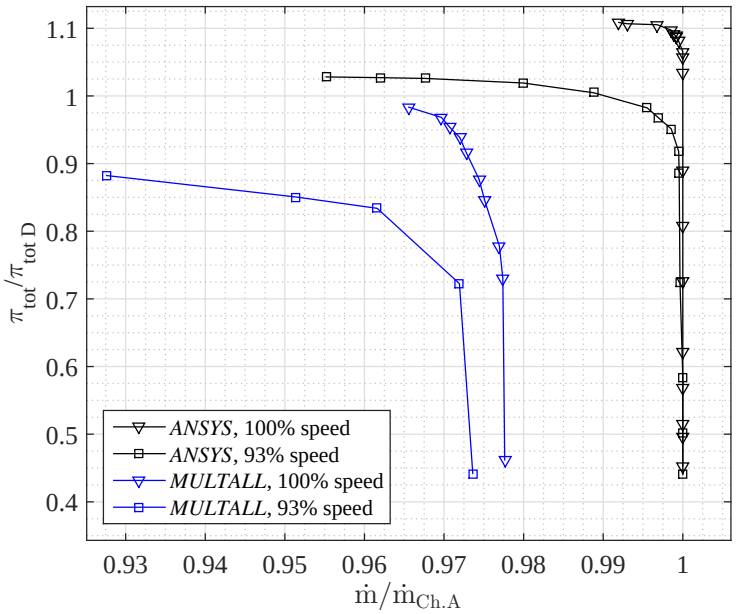

Figure 5.13: MULTALL total pressure ratio comparison with ANSYS® results for the multi-stage compressor.

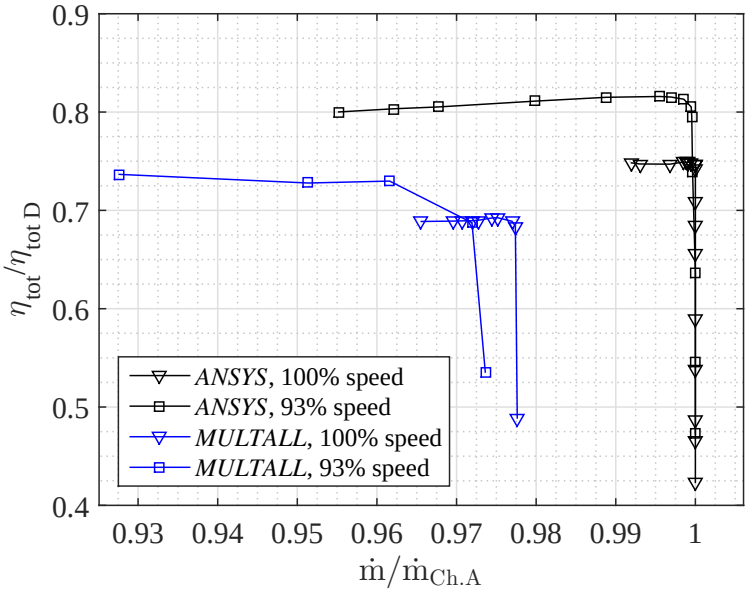

Figure 5.14: MULTALL total to total isentropic efficiency comparison with ANSYS® results for the multi-stage compressor.

Stellenbosch University https://scholar.sun.ac.za

5.7 MULTALL in a commercial environment

The suitability of using MULTALL for transonic compressor performance prediction is discussed. In commercial CFD, the ability to predict the difference in the performance of various designs is often more important than being able to predict the exact magnitude of a performance attribute. It is concluded that the current MULTALL version can be used for analysis of transonic axial compressors with the help of the necessary external programs. The most time-consuming aspect for compressor analysis is importing the geometry. However, once the baseline geometry is ready to be solved by MULTALL, the same external program used to assist with importing the geometry can be used to modify the baseline geometry to obtain input files for different designs within minutes. Once these input files have been created, multiple instances of MULTALL can be run on a single processor with multiple threads. Therefore, different designs may be solved simultaneously on a single processor. Alternatively, a range of solutions on an operating curve may be solved simultaneously for a specific design after having obtained an initial solution, except when solving the model near stall. In rough estimates, experience with solving typical MULTALL models (approximately 280000 elements per stage) on a 3.7 GHz processor with 12 threads, shows that a performance curve can typically be solved within approximately 1 hour per stage. This estimate assumes that the user is actively involved in making the necessary adjustments to obtain convergence.

Another convenience of the MULTALL-open suite of programs is that a plotting program is included. This program can be used to generate plots of the mesh and a selection of solution variables along grid points. Since the plots are generated along grid points, the program can not be used to view the geometry to scale. As mentioned before, the geometry should be viewed to scale on an external program, such as the MATLAB® program written for this work.

Stellenbosch University https://scholar.sun.ac.za

Chapter 6

Conclusion

6.1 Validation test cases in ANSYS®

During CFD validation of ANSYS®, it was concluded that the $k-\omega$ turbulence model and the $SST-\gamma Re_\theta$ with a modified shear stress parameter of $a_1 = 0.345$ perform well for both test cases in terms of overall compressor performance, with the $SST-\gamma Re_\theta$, $a_1 = 0.345$ result being superior to the $k-\omega$ result with regards to predicting the experimental separation behaviour on the Darmstadt stator. The $SST-\gamma Re_\theta$ with standard structure parameter under-predicts the pressure ratio for both test cases. Furthermore, the modified structure parameter of the $SST-\gamma Re_\theta, a_1 = 0.345$ model suppresses seemingly premature chaotic corner stall when the Darmstadt compressor is operated closer to stall. During CFD validation it was also concluded that the choking mass flow rate of a compressor is better predicted when a transition model is used. Results suggest that turbulence models without transition modelling over-predict blockage because of the omitted laminar boundary layer flow present in the experiment.

6.2 Comparison of transient and steady-state results

It is concluded that the erroneous treatment of flow features at the mixing plane of a steady state model most likely gains significance in modelling of multi-stage compressors. During a comparison of transient and steady state results for a single stage, the results did not differ significantly. However, for the multi-stage compressor, slightly lower performance is predicted in terms of pressure ratio, efficiency, and choking mass flow rate. Entropy production at the tip clearance flow increases. Losses are also increased by increased corner stall at some blade rows.

Stellenbosch University https://scholar.sun.ac.za

6.3 Effects of fillets and wall roughness

With regards to the effect of fillets, hub corner stall is restrained for shaft speeds at which corner stall is significant, reducing blockage and resulting in a slightly higher choking mass flow rate. At lower shaft speeds where corner stall is less significant, the addition of fillets only serve to add material blockage, reducing the choking mass flow rate. In terms of pressure ratio and efficiency, slightly lower performance is observed at low shaft speeds. Around the design point, the isentropic efficiency is increased rather than reduced. However, the required shaft power at the same pressure ratio is more for the filleted model. This is because the effect of flow stagnation, which is a loss in terms of fluid flow, is replaced by material blockage.

With regards to surface roughness, the addition of blade surface roughness has a greater effect than endwall roughness due to for example, the outward migration of a thickened suction side boundary layer which mixes with the tip leakage flow to and the geometric nature of the particular compressor passage. Due to a reduced tip clearance vortex size in the case of a roughened shroud, some of the boundary layer blockage caused is compensated for in this case, which is why the choking mass flow rate is much less affected in comparison to a roughened blade.

6.4 The use of MULTALL for transonic axial compressor performance prediction

With regards to the magnitude of performance attributes predicted by typical MULTALL simulations, good estimates were obtained for the test cases. The ability to predict the difference in the performance of various designs is often more important than being able to predict the exact magnitude of a performance attribute. The level of accuracy with which MULTALL resolves typical flow features of transonic axial compressors such as the tip clearance flow features, is promising. It is concluded that the current MULTALL version can be used for analysis of transonic axial compressors with the help of the necessary external programs. Furthermore, the speed at which typical MULTALL models can be solved is promising for use in commercial CFD applications.

Stellenbosch University https://scholar.sun.ac.za

References

ANSYS®. 2019. *ANSYS® CFX® theory guide.* [Online]. Available: www.ansyshelp.ansys.com.

Aungier, R.H. & Farokhi, S. 2004. Axial-Flow Compressors: A Strategy for Aerodynamic Design and Analysis. *Applied Mechanics Reviews. 57. 22-10.1115/1.1786589.*

Aupoix, B. & Spalart, P. 2003. *Extensions of the Spalart-Allmaras turbulence model to account for wall roughness. International Journal of Heat and Fluid Flow. 24. 454-462. 10.1016/S0142-727X(03)00043-2.*

Bakhtiari, F. & Wartzek, F. & Leichtfuß, S. & Schiffer, H. & Goinis, G., & Nicke, E. 2015. *Design and Optimization of a New Stator for the Transonic Compressor Rig at TU Darmstadt.*

Bammert, K. and Woelk, G. U. 1980. The Influence of the Balding Surface Roughness on the Aerodynamic Behavior and Characteristic of an Axial Compressor, *Journal of Engineering for Power, Transactions from ASME, vol. 102, no.2, April 1980.*

Bergner, J. 2006. *Experimentelle Untersuching der Störmung im Blattspitzenbereich eines transsonischen Axialverdichters nahe der Stabilitätsgrenze.* Technische Universität Darmstadt, PhD Dissertation.

Bergner, J., Hennecke, D. K., Kablitz, H. 2003. Darmstadt Rotor No. 2, III: Experimental Analysis of an Aft-Swept Axial Transonic Compressor Stage *International Journal of Rotating Machinery, 9: 393?402, 2003*

Biollo, R. & Benini, E. 2011. *State-of-Art of Transonic Axial Compressors, Advances in Gas Turbine Technology. ISBN: 978-953-307-611-9.*

Boretti, A. 2010. Experimental and Computational Analysis of a Transonic Compressor Rotor. *17th Australasian Fluid Mechanics Conference.*

Stellenbosch University https://scholar.sun.ac.za

Brockett, W. & Kozak, A. 1982. *Small axial turbine stator technology program.* NASA CR- 165602.

Broichhausen, K. D. & Ziegler, K. U., 2005. Supersonic and Transonic Compressors: Past, Status and Technology Trends, *Proceedings of ASME Turbo Expo 2005*, GT2005-69067.

Calvert, W.J. & Ginder, R.B. 1999. Transonic fan and compressor design. *Proceedings of the Institution of Mechanical Engineers, Part C: Journal of Mechanical Engineering Science 213.*

Chen, Shao-wen., Xu, Hau., Wang, Song-tao,. Wang, Zhong-qi. 2014. Experimental research of surface roughness effects on highly-loaded compressor cascade aerodynamics. *Journal of Thermal Science. 1993-033X.*

Chima, R. V. 1998. Calculation of Tip Clearance Effects in a Transonic Compressor Rotor. *ASME Journal of Turbomachinery, Vol. 120, No. 1, (January 1998), pp. 131-140, ISSN 0889-504X.*

Chima, R.V. and Liou, M.-S. 2003. Comparison of the AUSM+ and H-CUSP Schemes for Turbomachinery Applications, *AIAA Paper AIAA-2003-4120. Also NASA/TM-2003-212457.*

Chinnaswamy, S. 2015. *The Impact of Surface Roughness on Transonic Compressor Performance.* Masters thesis, Chalmers University.

Denton, J.D. 2017. *Multistage Turbomachinery Flow Calculation Program MULTALL_OPEN.* [Online]. Available: www.whittle.eng.cam.ac.uk.

Denton, J.D. 2017. *Instructions for Program STAGEN.* [Online]. Available: www.whittle.eng.cam.ac.uk.

Denton, J.D. 2018. *Data input for the program MULTALL_OPEN using "NEW_READIN".* [Online]. Available: www.whittle.eng.cam.ac.uk.

Dixon, S.L. 2014. *Fluid Mechanics and Thermodynamics of Turbomachinery.* ISBN: 978-0-12-415954-9, 2014.

Eggenspieler, G. 2011. Modelling Laminar-Turbulent Transition Processes *ANSYS® Presentation.* [Online]. Available: https://support.ansys.com/staticassets /ANSYS/Conference/Confidence/San%20Jose/Downloads /turbulence-transition-modeling-5.pdf.

Estevadeordal, J. & Gorrell, S. E. & Copenhaver, W. W. 2007. PIV Study of Wake-

Stellenbosch University https://scholar.sun.ac.za

Rotor Interactions in a Transonic Compressor at Various Operating Conditions, *Journal of Propulsion and Power, Vol. 23, No. 1, (Jan-Feb 2007), ISSN 0748-4658*

Hah, C. 2009. *Large Eddy Simulation of Transonic Flow Field in NASA Rotor 37* NASA/TM-2009-215627.

Hah, C., Copenhaver, W.W., and Puterbaugh, S.L. 1993. Three-Dimensional Flow Phenomena in a Transonic High-Throughflow, Axial-Flow Compressor Stag. *ASME Journal of Turbomachinery, vol. 115, no. 2, pp. 240-248.*

Hah, C. & Loellbach, J. 1999. Development of Hub Corner Stall and Its Influence on the Performance of Axial Compressor Blade Rows. *ASME Journal of Turbomachinery, Vol. 121, No. 1, (January 1999), pp. 67-77, ISSN 0889-504X.*

Hah, C., Rabe, D.C., Sullivan, T.J., and Wadia, A.R. 1996. Effects of Inlet Distortion on the Flow Field in a Transonic Compressor Rotor, *ASME Journal of Turbomachinery, vol. 120, no. 2, pp.233-246*

Haideng, Zhang & Yun, wu & Yinghong, Li & Huawei, Lu. 2015. Experimental investigation on a high subsonic compressor cascade flow. *Chinese Journal of Aeronautics. 107. 10.1016/j.cja.2015.06.019.*

Farokhi, S. 2008. *Aircraft Propulsion.* Wiley, John Sons, Incorporated.

Hawthorne, W. R. 2017 *Aerodynamics of Turbines and Compressors.* (HSA-1), Volume 1 (High Speed Aerodynamics and Jet Propulsion). Princeton University Press.

Flack, R. D., *Fundamentals and Applications of Jet Propulsion.* Cambridge University Press, 2005.

Hofmann, W. Ballmann, J. 2002. Tip Clearance Vortex Development and Shock-Vortex-Interaction in a Transonic Axial Compressor Rotor. *Proceedings of 40th AIAA Aerospace Sciences Meeting and Exhibit, AIAA 2002-0083*

Haug, J. P. & Niehaus, R. 2018. Full Annulus Simulations of a Transonic Axial Compressor Stage with Distorted Inflow at Transonic and Subsonic Blade Tip Speed. *Proceedings of the European Turbomachinery Conference ETC12 2017, Paper No. 211.*

Funk & Wagnall. (2008) Retrieved from Funk & Wagnall's New World Encyclopedia database, Encyclopædia Britannica.

Stellenbosch University https://scholar.sun.ac.za

Jongsik (Justin), Oh. 2016. The Effects of Blade Fillets on Aerodynamic Performance of a High Pressure Ratio Centrifugal Compressor. *International Compressor Engineering Conference.*

Kantrowitz, A., 1950. The Supersonic Axial-Flow Compressor *NACA report 974.*

Khalid S. 1994. *The Effects of Tip Clearance on Axial Compressor Pressure Rise* PhD. dissertation, Massachusetts Institute of Technology

Klapproth, J. F. 1952. Performance of an Impulse-type Supersonic Compressor with Stators. *NACA report E52B22.*

Kügeler E. & Nürnberger, D. & Weber A. & Engel K. 2008. Influence of Blade Fillets on the Performance of a 15 Stage Gas Turbine Compressor. *Proceedings of the ASME Turbo Expo: Power for Land, Sea, and Air, Volume 6: Turbomachinery, Parts A, B, and C:415-424. doi:10.1115/GT2008-50748.*

Malan, P., Suluksna, K., Juntasaro, E. 2009. Application of Stereoscopic and Tomographic PIV in a Transonic Cascade. *47th AIAA Aerospace Sciences Meeting. 6.2009-1142*

Menter, F. & Langtry, R.B. & R. Likki, S. & Suzen, Y. & Huang, P. & Völker, S. 2006. A Correlation-Based Transition Model Using Local Variables Part I: Model Formulation. *ASME Journal of Turbomachinery .128. 10.1115/1.2184352*

Millsaps, K. T.& Baker, L. J. & Patterson, J. S. 2004. Detection and Localization of Fouling in a Gas Turbine Compressor From Aerodynamic Measurements, *Proceedings of the ASME Turbo Expo 2004, Vienna, Austria, Paper No. GT2004-54173, Vol. 5B, pp. 1867-1876*

Müller, M., Schiffer, H.-P., Hah, C. 2007. Effect of circumferential grooves on the aerodynamic performance of an axial single-stage transonic compressor. *Proceedings of the ASME Turbo Expo GT2007-27365*

Müller, M., & Schiffer, H.-P.& Voges, M. & Zscherp, C. 2009. Experimental Investigation of the Rotor / Casing Treatment Interaction in an Axial Single-Stage Transonic Compressor. *8th European Turbomachinery Conference*

Nikuradse, J. 1933 Strömungsgesetze in rauhen Rohren. *Forschung Im Ingenieurwesen, Ausg. Beill. 4, 361.*

Prasad, A. 2003. Evolution of Upstream Propagating Shock Waves From a Transonic Compressor Rotor. *ASME Journal of Turbomachinery, Vol. 125, No. 1, (January 2003), pp. 133-140, ISSN 0889-504X.*

Stellenbosch University https://scholar.sun.ac.za

Rajeevalochanam, P. & Sunkara, A. & Kalita, N. & Vailshery, M. 2017. Numerical Study on the Effect of Blade Fillet in an Axial Turbine Stage *17th (2017) CFD Symposium.*

Reid, L. & Moore R.D. 1980. Design and Overall Performance of Four Highly Loaded, High-Speed Inlet Stages for an Advanced High-Pressure-Ratio Core Compressor. *Lewis Research Center, NASA Technical Paper 1337.*

Reid, L. & Moore R.D., 1978. Performance of Single-Stage Axial-Flow Transonic Compressor With Rotor and Stator Aspect Ratios of 1.19 and 1.26, Respectively, and With Design Pressure Ratio of 2.05. *Lewis Research Center, NASA Technical Paper 1659.*

Reising, S. & Schiffer, H.-P. 2009. Non-Axisymmetric End Wall Profiling in Transonic Compressors. Part I: Improving the Static Pressure Recovery at Off-Design Conditions by Sequential Hub and Shroud End Wall Profiling. *ASME Paper GT2009-59133.*

Schlichting, H. 1987. *Boundary Layer Theory.* McGraw-Hill Inc.

Shi, Yan & Li, Jun & Feng, Zhenping. 2010. Influence of Rotor Blade Fillets on Aerodynamic Performance of Turbine Stage. *Proceedings of the ASME Turbo Expo. 7. 10.1115/GT2010-23721.*

Stratford, B. 1973. The prevention of flow separation and reversal in the corners of compressor blade cascades. *Aeronautical Journal, vol. 77, pp 249-256.*

Suder, K. L. 1998. Blockage Development in a Transonic, Axial Compressor Rotor *ASME Journal of Turbomachinery, Vol. 120, No. 3, (July 1998), pp. 465-476, ISSN 0889-504X*

Tan, J. & Jin, J. 2011. Stress Limiter Consideration for k-w Turbulence Models in Shock Wave/Turbulent Boundary Layer Interactions in Supersonic and Hypersonic Flows. *AIAA Paper 2011-3980.*

Tharwat,R., El-Samanoudy, M., El-Baz, A. M. R. 2016. Considerations of Stress Limiter for the SST Turbulence Model in Dual Throat Nozzle Predictions. *International Conference on Computational Fluid Dynamics ICCFD9-2016-123*

Tweedt, D. & Okiishi, T. 1983. Stator blade row geometry modification influence on twostage compressor aerodynamic performance. *Air Force Office of Scientific Research AFOSR-TR-84-0418.*

Stellenbosch University https://scholar.sun.ac.za

Pullan, G. 2004. Secondary Flows and Loss Caused by Blade Row Interaction in a Turbine Stage. *ASME Journal of Turbomachinery, 2004;128(3):484-491. doi:10.1115/1.2182001.*

Shabbir, A., Celestina, M.L., Adamczyk, J.J., and Strazisar, A.J. 1997. The Effect of Hub Leakage Flow on Two High Speed Axial Compressor Rotors *ASME Paper 97-GT-346, June 1997.*

Suder, K.L., and Celestina, M.L.M 1995. Experimental and computational investigation of the tip clearance flow in a transonic axial compressor rotor. *NASA-TM-106711*

Suder, K.L., Chima, R.V., Strazisar, A.J., and Roberts, W.B. 1995. The Effect of Adding Roughness and Thickness to a Transonic Axial Compressor Rotor. *ASME Jounral of Turbomachinery, vol. 117, Oct. 1995, pp. 491-505.*

Weber, A. & Schreiber, H.A. & Fuchs, R. & Steinert, W. 2002. 3-D Transonic Flow in a Compressor Cascade With Shock-Induced Corner Stall. *ASME Journal of Turbomachinery, Vol. 124, No. 3, (July 2002), pp. 358-366, ISSN 0889-504X.*

Willert, C & Klinner, J. 2014. Application of Stereoscopic and Tomographic PIV in a Transonic Cascade. *AFDAR International Workshop on Advanced Flow Diagnostics for Aeronautical Research.*

Stellenbosch University https://scholar.sun.ac.za

Appendices

Stellenbosch University https://scholar.sun.ac.za

Appendix A
Validation test cases

A.1 NASA Stage-37 mesh information

The mesh for NASA Stage-37 can be seen in Figure 1. The coarse inlet domain for an estimate of the rotor inlet-profile can be seen upstream of the rotating-mesh rotor domain. It can be seen that the mesh is relatively fine for some distance upstream of the rotor and downstream of the stator in order to resolve the rotor-bow shock and stator separation-wake.

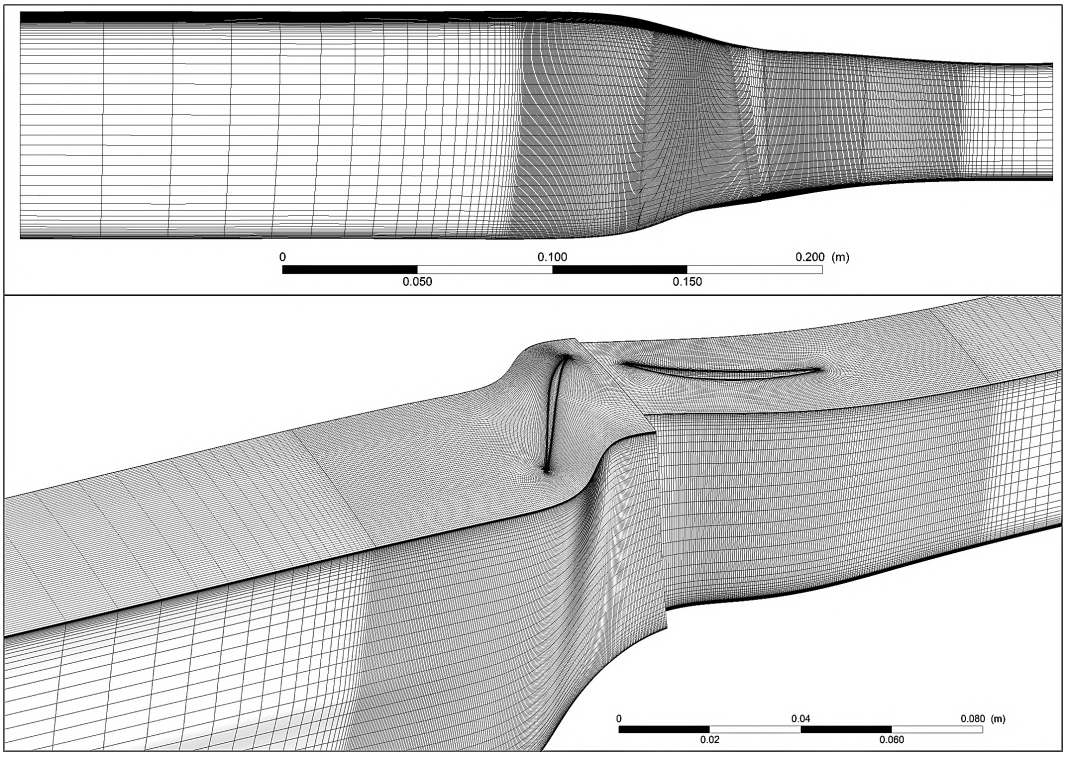

Figure 1: NASA Stage-37 mesh in ANSYS® CFX®.

The grid information for NASA Stage-37 is given in Tables 1 to 3. It was con-

Stellenbosch University https://scholar.sun.ac.za

cluded that the model becomes adequately mesh independent at a mesh with 3.66 million rotor nodes and 1.37 million stator nodes. In Table 3, the number nodes, first cell height, and solution file size for the different grids can be seen. The mesh solution convergence data at choke can be seen in Table 4. Residual convergence can be seen in Table 5. It is concluded that the solutions become adequately mesh independent for this work around 3.66 million nodes for the rotor domain and 1.37 million nodes for the stator domain.

Table 1: General grid information (Stage-37)

	Rotor nodes	Stator nodes	Rotor first cell height [um]	Stator first cell height [um]	file size [GB]
1	1.2M	850k	20	20	1.76
2	2M	850k	20	20	2.39
3	3M	1.1M	20	20	3.43
4	3.33M	1.27M	10	10	3.83
5	3.66M	1.37M	5	5	4.24

Table 2: Grid y^+ and convergence at choke (Stage-37)

#	Mass flow [kg/s]	Isentropic efficiency	Pressure ratio	Rotor max y^+	Stator max y^+
1	20.90	0.7684	1.7963	29.3	25.0
2	20.921	0.7713	1.7995	29.5	24.9
3	20.927	0.7716	1.8021	29.8	25.4
4	20.913	0.7691	1.8022	18.7	15.5
5	20.907	0.7685	1.8022	11.9	9.8

Table 3: Residual convergence (Stage-37)

#	W-mom	V-mom	U-mom	P-Mass
1	1.50E-04	1.50E-04	6.20E-05	1.75E-05
2	1.30E-04	1.19E-04	5.40E-05	1.55E-05
3	1.45E-04	1.28E-04	6.10E-05	1.98E-05
4	1.14E-04	1.30E-04	5.25E-05	1.76E-05
5	1.15E-04	1.40E-04	5.30E-05	1.65E-05

Stellenbosch University https://scholar.sun.ac.za

A.2 Modelling parameters

The boundary conditions and modelling parameters used for the Darmstadt R-1/S-1 test case in ANSYS® CFX® are shown in Tables 4 and 5, respectively.

Table 4: Darmstadt R-1/S-1 boundary conditions in ANSYS® CFX®

Location	**Boundary condition**	**Value**
Inlet	Total pressure (subsonic regime)	101.325 kPa
	Total temperature	288.15 K
	Fractional turbulent intensity	0.04
	Flow direction	Normal to boundary condition
Outlet	Static pressure (subsonic regime) with circumferential pressure-averaging and profile blend factor of 0.05 (recommended in ANSYS® manual (2019))	Varied from 1 atm to 1.4 atm depending on turbulence model
Rotating-mesh rotor domain shroud	Wall velocity	Counter rotating at 20000.0 rpm
Inlet domain hub	Wall velocity	Rotating at 20000.0 rpm
Stator domain hub	Stationary hub	N/A

Table 5: Modelling control parameters in ANSYS® CFX® for Darmstadt R-1/S-1

Modelling control parameter	**Value**
Floating point accuracy	16 digits
Advection scheme	Bounded second-order upwind biased
Turbulence numerics	Bounded second-order upwind biased
Timescale factor	0.5 (0.1 for starting solution)
Specific heat at constant pressure	1004 J/kg.K (assumed)
Ideal gas transport properties	Sutherland's formula

Stellenbosch University https://scholar.sun.ac.za

A.3 Darmstadt test case

A comparison of the Darmstadt stator flow field for the $SST - \gamma Re_\theta, a_1 = 0.31$ and $SST - \gamma Re_\theta, a_1 = 0.345$ turbulence models at different mass flow rates are given in Figures 2 and 3. In Figure 3 it can be seen that seemingly premature chaotic and unstable stator flow separation occurs downward of 15.2 kg/s for the $SST - \gamma Re_\theta, a_1 = 0.31$ model.

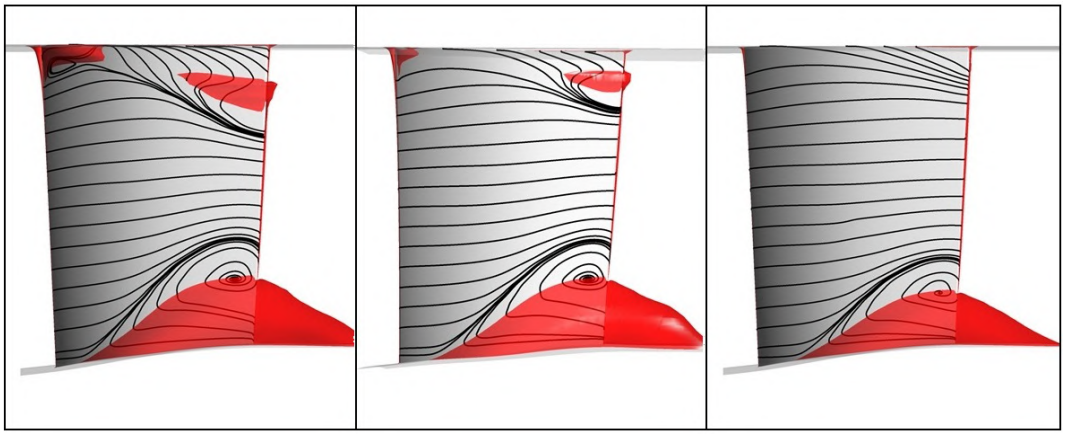

Figure 2: From left to right (14.8, 15.2, 16 kg/s) for $SST - \gamma Re_\theta$ model, $a_1 = 0.345$. Red indicates regions of negative axial velocity.

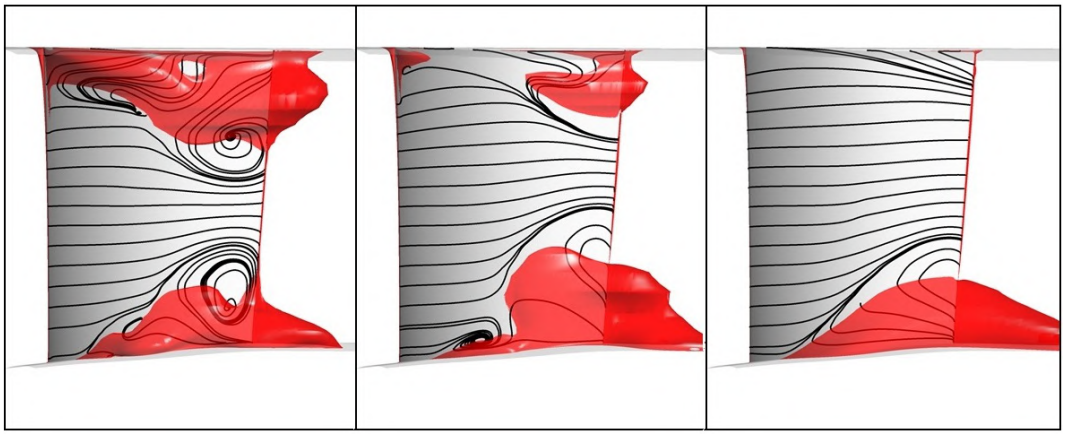

Figure 3: Chaotic unsteady stator flow at 14.8 and 15.2 kg/s. From left to right (14.8, 15.2, 16 kg/s) for $SST - \gamma Re_\theta$ model, $a_1 = 0.31(standard)$. Red indicates regions of negative axial velocity.

Stellenbosch University https://scholar.sun.ac.za

A.4 NASA Stage-37 performance curves

The numerical and experimental pressure ratio across the rotor (not the total pressure ratio) are compared for the NASA Stage-37 test case in Figure 4. The rotor isentropic efficiency (Figure 5), rotor temperature ratio (Figure 6), and stage temperature ratio (Figure 7) are also shown. Over-predicted shock induced boundary layer separation in the rotor had been identified as the cause of under-predicted pressure ratio. Similar to what was seen for the stage pressure ratio, the SST turbulence model performs the worst. If the γRe_θ transition model is enabled, there is a slight reduction in suction side shock-induced boundary layer separation. The $k-\omega$ and $k-\epsilon$ models perform well. The standard shear stress limiter of the SST turbulence model does not perform well in regions with large normal strain. With the adapted shear stress limiter, the $SST-\gamma Re_\theta, a_1 = 0.345$ model performs well.

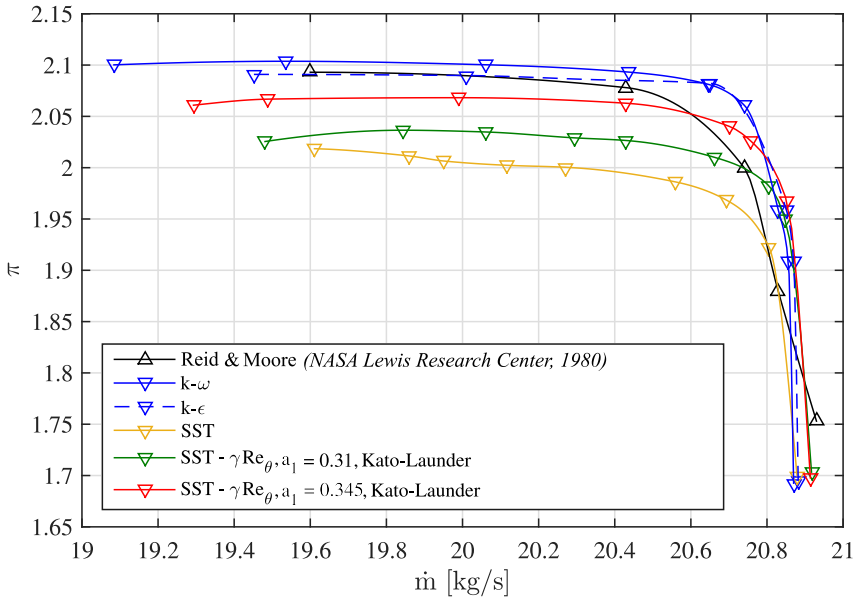

Figure 4: NASA Stage-37: rotor pressure ratio

Stellenbosch University https://scholar.sun.ac.za

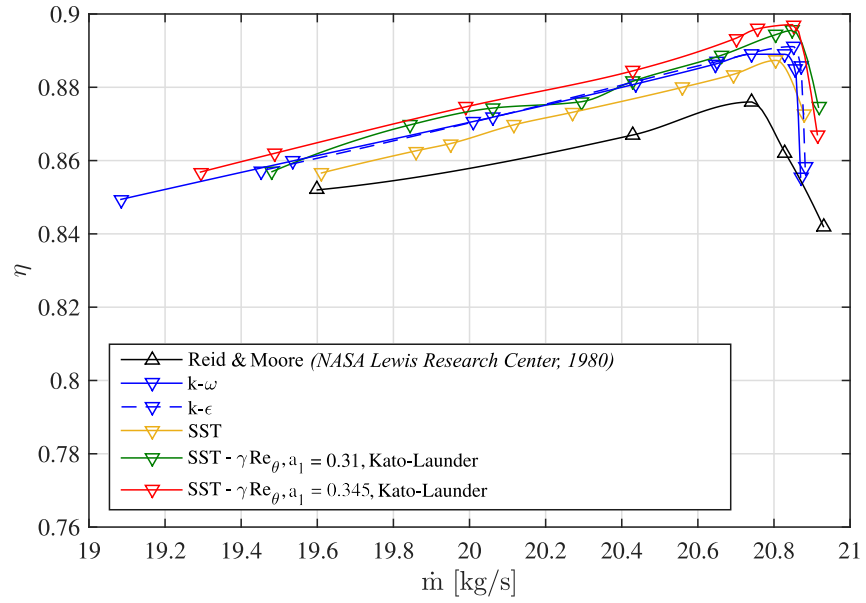

Figure 5: NASA Stage-37: rotor isentropic efficiency

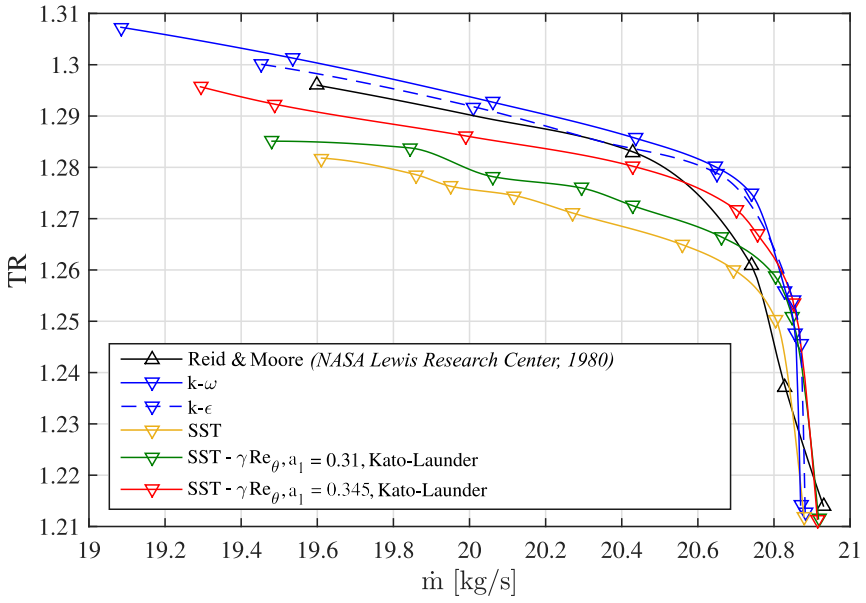

Figure 6: NASA Stage-37: rotor temperature ratio

Stellenbosch University https://scholar.sun.ac.za

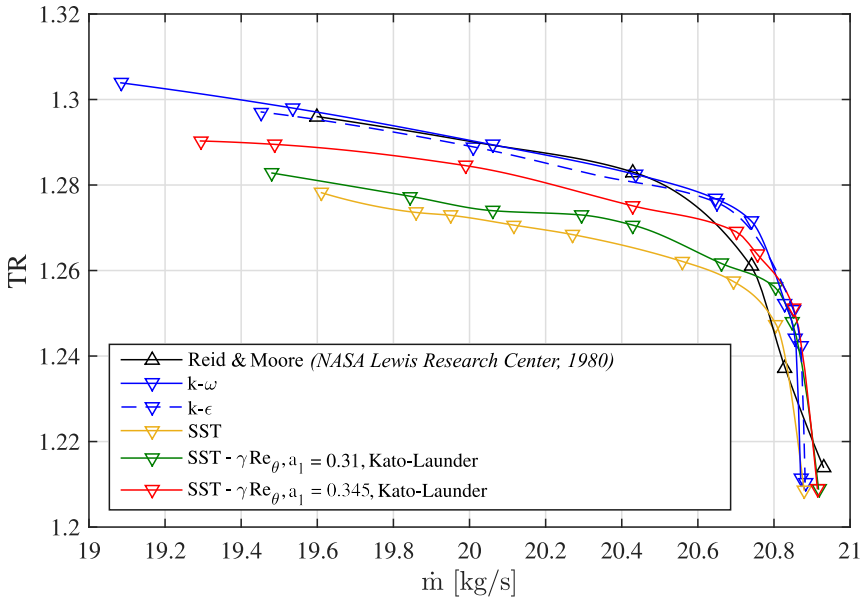

Figure 7: NASA Stage-37: stage temperature ratio

Stellenbosch University https://scholar.sun.ac.za

Appendix B
Main numerical investigation

B.1 Transient vs. steady-state comparison

In Figure 8, the location of the plane used for Figure 3.4 is shown for visual context.

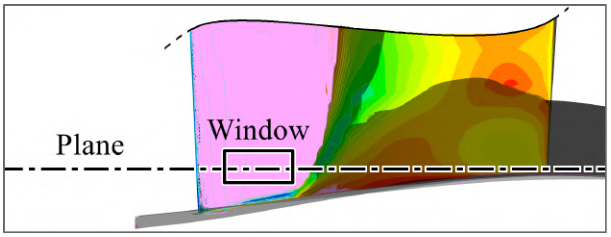

Figure 8: The location of the plane used for Figure 3.4.

B.2 ANSYS® multi-stage compressor mesh

The residual convergence for the multi-stage compressor for different grids can be seen in Table 6. It is concluded that convergence is adequate for a steady-state model. The first cell height at different stages can be seen in Table 7. Note that the first cell height is reduced in later stages to compensate for an increase in grid y^+.

Stellenbosch University https://scholar.sun.ac.za

Table 6: Multi-stage mesh dependency convergence

#	W-mom	V-mom	U-mom	P-mass
1	4.96E-06	2.34E-06	1.05E-06	1.14E-06
2	5.27E-06	2.40E-07	8.00E-07	6.00E-07
3	4.86E-06	4.00E-07	4.00E-07	9.70E-07
4	1.69E-05	6.98E-07	1.76E-06	4.11E-07
5	2.41E-05	8.60E-07	2.23E-06	1.27E-06
6	2.09E-05	1.26E-06	4.06E-06	1.81E-07
7	1.98E-05	7.80E-07	1.68E-06	3.20E-07
8	1.72E-05	7.12E-07	2.36E-06	5.40E-07
9	1.53E-05	1.17E-05	2.26E-06	7.90E-06
10	2.40E-05	3.20E-05	5.45E-05	5.32E-05

Table 7: First cell height per stage [μm]

Grid no.	Stage-1	Stage-2	Stage-3	Stage-4
1	80	70	60	55
2	80	70	60	55
3	40	35	30	27.5
4	20	17.5	15	13.75
5	10	8.75	7.5	6.875
6	10	8.75	7.5	6.875
7	10	8.75	7.5	6.875
8	5	4.375	3.75	3.4375
9	1	0.875	0.75	0.6875
10	0.4	0.35	0.3	0.275

Stellenbosch University https://scholar.sun.ac.za

B.3 Transient and steady-state comparison

An example of the difference in complexity between a transient and steady-state results is given in Figure 9.

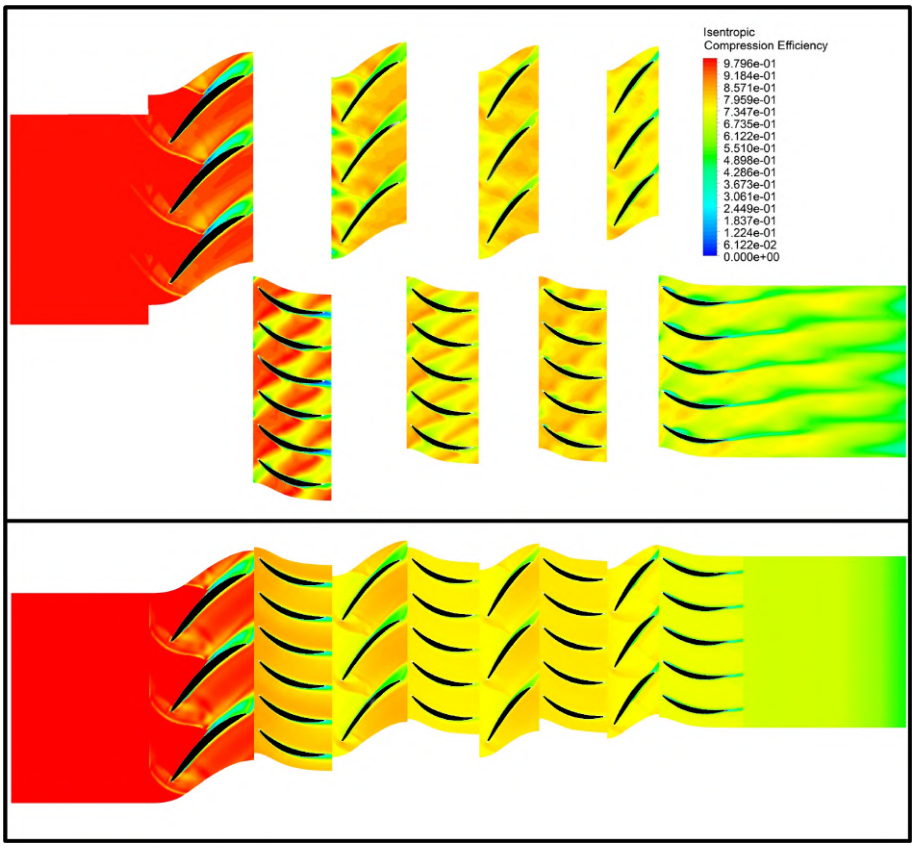

Figure 9: Isentropic compression efficiency contour plot at 50% span showing the difference in complexity between the transient (top) and steady-state solutions

B.4 Effect of blade and endwall roughness

The results for the roughness study at 100% speed can be seen in Figures 10 and 11. As expected, the choking mass flow rate decreases as the total roughened surface area through the compressor increases due to increased blockage. Since the compressor lacks mass flow rate stall margin at 100% speed, these results are not analysed with regards to efficiency and pressure ratio reduction. It can be seen that, for the extreme case (B8W8), the reduction in choking mass flow rate is only 0.5%.

Stellenbosch University https://scholar.sun.ac.za

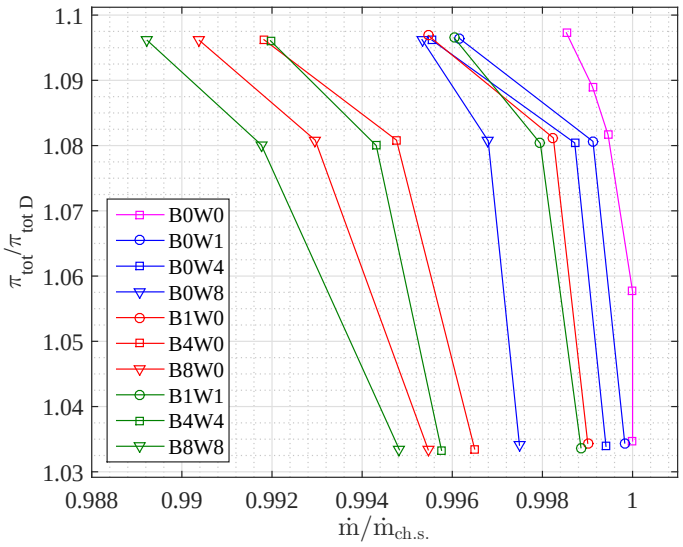

Figure 10: Roughness study pressure ratio at 100% design speed.

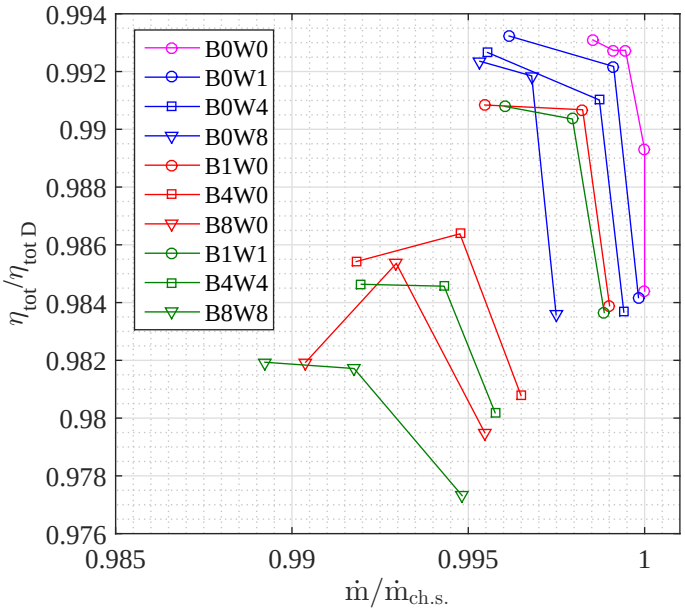

Figure 11: Roughness study isentropic efficiency at 100% design speed.

Stellenbosch University https://scholar.sun.ac.za

B.5 Effect of fillets

Another example of reduced flow separation due to fillets can be seen in Figure 12. It can be seen that stall in the lower half of the blade is reduced.

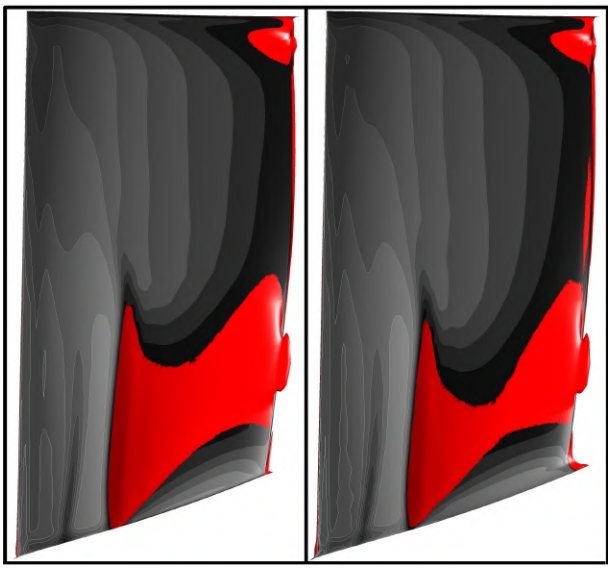

Figure 12: Reduced flow separation due to the addition of fillets (the filleted model is on the right). The red ISO surface shows negative axial velocity.

Stellenbosch University https://scholar.sun.ac.za

Appendix C
MULTALL

C.1 Geometry definition

In Figure 14, a comparison between the original and mathematical thickness distribution at different blade profile sections is shown. It can be seen that, although the difference is small, some discrepancies exist.

Stellenbosch University https://scholar.sun.ac.za

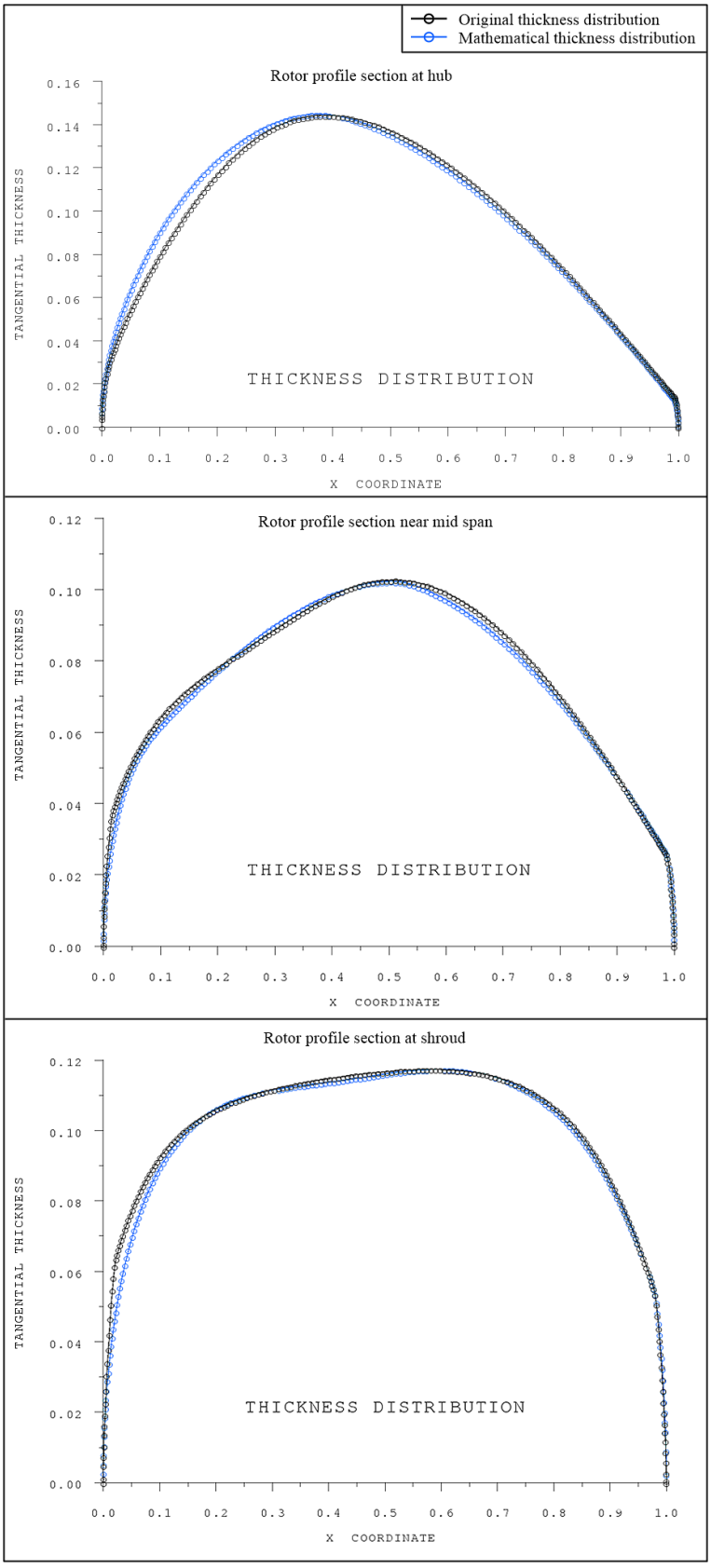

Figure 13: NASA Stage-37 rotor thickness distribution. A comparison between the original and mathematical thickness distribution.

Stellenbosch University https://scholar.sun.ac.za

C.2 Modelling setup

Solver parameters

Solver parameters which were found to be notably important in order to achieve convergence are shown in Table 8.

Table 8: Solver parameter values which have been used accordingly in order to obtain convergence of MULTALL models. ***Default value**.

Parameter	Value	Comments
ITIMST	3*	This option selects the "scree" scheme, introduced to MULTALL in 2000. It is robust and second order accurate. This scheme is preferred in most cases (Denton, 2018).
CFL	0.2-0.5 0.4*	The time step length factor is typically 0.4. If other methods fail, reduce to 0.2 if instability is encountered.
DAMP	8-10*	If instability was encountered, the damping factor was reduced. This factor limits the ratio of maximum change in the solution to the average change per time step.
NCHANGE	1000*-2000	Increase from the default of 1000 if instability is encountered.
FBLK1 FBLK2 FBLK3	0.2-0.4* 0.1-0.2* 0.05-0.1*	These safety factors on the multigrid block levels may be reduced if instability is encountered.
NMIXUP	1000*-2000	If the solution diverges when starting from initial solution guesses, consider increasing.
FACMIXUP	2.0*-3.0	Same as above.
FEXTRAP FANGLE	0.8*-0.95 0.8*-0.95	Increase if instability at the mixing plane is encountered.
RFIN	0.1 or 0.5	Reduce this relaxation factor on changes in inlet pressure if instability at the inlet is encountered.
SFEXIT	0* or 0.1	Set to 0.1 if flow tries to reverse at outlet.
NSFEXIT	0* or 5-10	Increase if flow tries to reverse at outlet.

As per Table 8, if the solution diverges after $NCHANGE$ iterations, consider increasing $NCHANGE$ or reducing the $DAMPIN$ value, which has a standard value of 10. The $DAMPIN$ value limits the ratio of maximum change to the average change per time step. However, note that if the $DAMPIN$ value is reduced by too much, such that

$$DAMP = DAMPIN(1 - 0.75 \times FCHANGE) < 2 \tag{1}$$

Stellenbosch University https://scholar.sun.ac.za

where

$$FCHANGE = 1 - (NSTEP - 1)/NCHANGE \tag{2}$$

and $NSTEP$ is the current time step, then the damping process is skipped altogether (the above can be seen in the MULTALL Fortran code). The solution then often diverges within the first 50 iterations. Often the default value of 10 for $DAMPIN$ can only be reduced to 8, depending on the starting solution. The role of $DAMP$ can be seen in equation 4.3, as found in Denton (2017).

$$\triangle_{used} = \frac{\triangle_{calc}}{1 + \dfrac{Abs(\triangle_{calc})}{DAMP}} \tag{3}$$

It may also help to increase the default of 1000 iterations over which damping and smoothing is applied, or to reduce CFL (time step length factor). Note that $NCHANGE$ is not to be confused with $NMIXUP$, which is the number of iterations (default of 1000) over which turbulent viscosity is increased by a specified factor $FACMIXUP$ to help with convergence if starting from the assumed initial conditions (no solved flow field). Therefore, if the solution diverges when starting from initial solution guesses, consider increasing $NMIXUP$ or $FACMIXUP$.

Stellenbosch University https://scholar.sun.ac.za

C.3 Multi-stage compressor

Selected regions of the MULTALL multi-stage compressor mesh can be seen in Figure 14. Note the forward lean of the rotor blades (not to scale in these grid-wise plots).

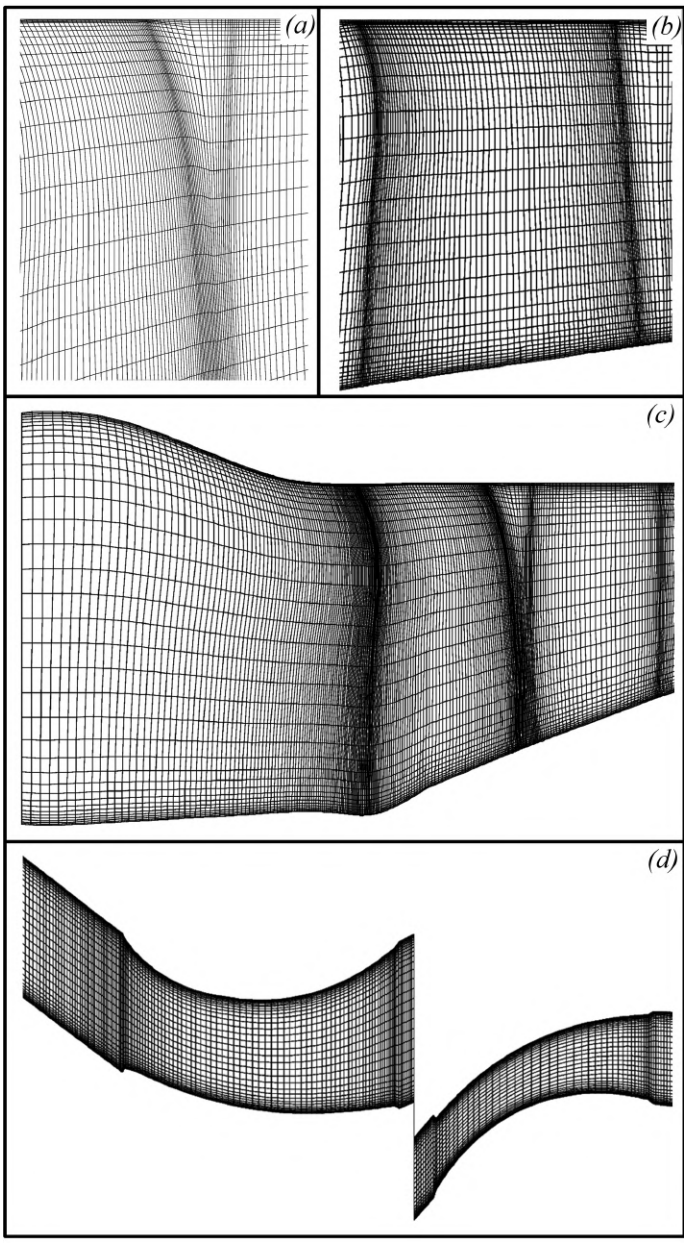

Figure 14: Multi-stage compressor mesh. (a): Meridional detail at the tip gap of the first stage. (b): Meridional overview of rotor 3. (c): Meridional overview of the inlet and first stage. (d): Stream surface at first stage.